

Diagnostic of Laser Produced Plasmas and Investigation of Laser-Solid Interactions Using X-Ray Diffraction from Bent Crystals

Dissertation

zur Erlangung des akademischen Grades
doctor rerum naturalium (Dr. rer. nat.)



vorgelegt dem Rat der Physikalisch-Astronomischen Fakultät
der Friedrich-Schiller-Universität Jena

von Diplom-Physiker **Faton S. Krasniqi**

geboren am 28.04.1978 in Skopje, Mazedonien

Gutachter:

1. **Prof. Dr. E. Förster**
Institut für Optik und Quantenelektronik
Friedrich Schiller Universität Jena
2. **Prof. Dr. P. Mulser**
Institut für Angewandte Physik
Technische Universität Darmstadt
3. **Prof. Dr. G. Pretzler**
Institut für Laser- und Plasmaphysik
Heinrich Heine Universität Düsseldorf

Tag der letzten Rigorosumsprüfung: 26.10.2005

Tag der öffentlichen Verteidigung: 22.11.2005

Dedicated to
my Parents

Contents

Contents	i
1 Introduction	1
2 The Spectrometer and Experimental Setup	5
2.1 Introduction	5
2.2 Vertical-Geometry Johann Spectrometer (VJS)	7
2.2.1 Principle of VJS	7
2.2.2 Reconstruction of the Spectra	9
2.3 Experimental Setup	11
3 Spectral Line Broadening and Profile Modifications	13
3.1 Introduction	13
3.2 Diagnosis of Hot and Dense Plasmas Based on the Spectral Line Profile Analysis	14
3.3 Experimental Results and Discussion	17
3.4 Summary and Conclusions	22
4 Line Shift and Merging in Hot and Dense Al Plasmas	24
4.1 Introduction	24
4.2 Theoretical Background	26
4.3 Experimental Results and Discussion	30
4.4 Summary and Conclusions	35
5 Fine Structure Effects in Al Ly γ	37
5.1 The Effect of Dynamic Electric Fields in Al Ly γ Line Profile	37
5.2 Exhibition of the Charge Exchange Phenomena in Al Ly γ Line Profile	43
5.3 Experimental Results and Discussion	48
5.4 Summary and Conclusion	54
6 Semiconductor-Metal Phase Transition in SmS	56
6.1 General Considerations	56
6.2 Intermediate Valence	60
6.3 Pressure and Temperature Induced Phase Transitions in the Surface of SmS Crystal	62
6.4 Summary and Conclusions	63

7 Ultrafast Structural Dynamics in SmS Probed by Time-Resolved X-Ray Diffraction	64
7.1 Introduction	64
7.2 Femtosecond Laser Plasma X-Ray Sources	65
7.3 Generation of Strain Pulses in SmS by Femtosecond Laser Pulses	67
7.4 Time Resolved Experiments with SmS	70
7.4.1 Experimental Setup	70
7.4.2 Experimental Results	72
7.5 Summary and Conclusions	81
8 Summary and Conclusions	82
Zusammenfassung	85
Bibliography	89
A Nuclear Fusion	106
B Plasma Potential	110
C Line Broadening Mechanisms	114
D Doppler Shift	117
E The Stark Effect for H-like Ions and Parabolic Quantum Numbers	120
F Important Physical Constants of SmS	123
G Applications of SmS	126
H Characterization of the SmS Crystal	127
H.1 Introduction	127
H.2 Theoretical Background	127
H.3 Experimental Results and Discussion	129
H.3.1 Measurement of the SmS Crystal Rocking Curves	130
H.3.2 X-ray Diffraction Topography	132
H.4 Summary and Conclusions	133
I Phonon Wave-Vectors in X-Ray Diffraction	134

Chapter 1

Introduction

In recent years, the technology of ultrashort laser pulse generation has progressed to the point that picosecond and sub-picosecond (up to 10 fs) pulses are routinely produced (Wark, 1999). These laser pulses can be focused down to a few micrometers and enormous intensities can be reached (exceeding 10^{18} W/cm², see e.g. Audebert *et al.*, 2002). When such a high-power laser pulses strike a solid target, a characteristic sequence of processes such as surface vaporization, thermionic emission, electron-neutral and electron-ion inverse bremsstrahlung, leads to production of a *hot and dense plasma* (Weyl 1989; Root 1989). This plasma consists of particles at very high energies—of the order of 100 eV to several keV, and densities near solid (Atwood 1999). The high temperatures imply high velocities that cause the plasma to expand rapidly and cool; as a consequence these plasmas are short lived (close to the duration of the heating pulse). Because of the high energy concentrations, these plasmas tend to involve rapid plasma expansion and thus a sharp gradients in density and temperature (Atwood, 1999).

Hot and dense plasmas are a dominant aspect of many astronomical objects, whether in our solar system, in other stars, or in other galaxies (Cook, 1981; Bryant and Bingham, 1993; Hood, 1993; Kahn *et al.*, 2002). Merging the data from laboratory experiments with astronomical observation has a paramount importance to improve our knowledge of the universe (Dendy, 1993). Another aspect which motivates the study of these plasmas is connected with the goal of creating fusion as an energy source (see Appendix A). Furthermore, the states of fusion plasmas are similar to those in stellar interior (Ichimaru, 1993). Beside astrophysical and fusion applications, studies of hot and dense plasmas are of fundamental interest for X-ray laser research (see e.g. Bell,

1993) and X-ray lithography (Yaakobi *et al.*, 1983; Kühne and Petzold, 1988).

At the laser intensities above 10^{13} Wcm^{-2} , X-rays ranging in energies 50 eV to near MeV, will be emitted from a plasma (Hauer and Baldis, 1989). They have a special importance as a major diagnostic tool of the plasma. X-ray emission is a primary process occurring during both the evolution and expansion phases of the plasma. In fact, it is the main detectable process carrying information from the plasma during the stage of production and heating (Salzmann, 1978). Because of the characteristic atomic structure of the emitting ions, hot and dense plasma emits a spectrum which contain a wealth of information regarding such parameters as e.g. plasma temperature, density, ionization stage and size. In particular, it was found that the screening of the nuclear potential by the free electrons shifts the energy levels, modifies the bound electron wave functions, and changes the cross section of the atomic processes as a function of plasma density (see e.g. Salzmann, 1998). Thus, an accurate understanding of the atomic structure of the ions embedded in such plasmas is an essential ingredient in theoretical models relevant to astrophysics, as well as progress of fusion studies.

To study the effect of plasma environment on the emitter, one must create a plasma in a condition that is well defined, and at the same time, sophisticated X-ray spectrometers* (especially those with high spectral resolution) are required because spectral lines are generally shifted and broadened (see Chapters 3, 4, and references therein). Determining the conditions of plasma requires systems that, ideally, have no gradients. The spatial constraint (i.e., no gradient) comes from the fact that critical determination of the effects of interest requires that the contribution from widely varying plasma conditions (density and temperature) be minimized. This can be reached with the use of sandwich- and dot-target geometry (Leboucher-Dalimier *et al.*, 1993; Lee *et al.*, 1995). This help to suppress lateral gradients and isolate the plasma to a finite column that will move outward along the laser axis.

The first objective of this thesis (Chapters 2 to 5) is to investigate the influence of the intermediately coupled plasma environment (with plasma coupling constant near to one) on the radiating ions by using high-resolution, high-dispersion vertical geometry Johann spectrometer. Benefiting from the high spectral and spatial resolution of

*Plasma diagnostics techniques can be separated into two main categories (Hauer and Baldis, 1989): (i) those involving the analysis of the emission spectrum from the plasma, and (ii) those analyzing the changes undergone by radiation introduced into the plasma in the form of a probe beam (which is very useful to diagnose plasmas where self emission is weak or cannot escape due to large opacities).

the spectrometer used and optimized sandwich-target geometry, the influence of the ionization potential lowering and Langmuir oscillations in the emission spectra is observed. These results have both practical and theoretical importance. Practical, because some signatures observed in the emission spectrum lead to a new density diagnostics, and, theoretical, because they can be used to test different theoretical formulations of radiator-plasma interactions.

X-rays emitted from laser produced plasmas has been used also for many years to study the structural properties of crystalline and, to some extent, amorphous materials on the atomic scale (see e.g. [Helliwell and Rentzepis, 1997](#) and [Rousse *et al.*, 2001a](#)). Recent development in time-resolved X-ray diffraction, using both synchrotron and laser-plasma based sources, have lead to capability of directly observing structural changes in solid materials, phase transitions, the motion of complex molecules and chemical reactions, on picosecond or subpicosecond time scales ([Srajer *et al.*, 1996](#); [Perman *et al.*, 1998](#); [Rose-Petruck *et al.*, 1999](#); [Rousse *et al.*, 2001a](#); [Sokolowski-Tinten *et al.*, 2003](#); [Plech *et al.*, 2004](#)).

Improving the time resolution of X-ray diffraction measurements by moving into the picosecond and sub-picosecond time scales is important from both the fundamental physics and the applied technology points of view. From the scientific point of view, interaction of a material with ultrashort pulses produces non-equilibrium conditions where various processes may take place such as in particular, carrier excitation, carrier-phonon and carrier-carrier scattering, and carrier recombination (see e.g. review by [Sundaram and Mazur, 2002](#) and references therein). Time resolved X-ray diffraction can provide information about the evolution of the structural configuration which indeed help in the understanding the process development in the transient state. From the applied point of view, interaction of materials with ultrashort laser pulses is the basis for several rapidly developing new technologies, such as thin film processing and the chemical reaction control (see e.g. [Pronko *et al.*, 1995](#), [Helliwell and Rentzepis, 1997](#); [Willmott and Huber, 2000](#) and [Plech *et al.*, 2004](#)). Thus, the knowledge of the structural dynamics, radiation-matter coupling and mechanisms of energy transfer, will make possible the evaluation of the transient properties of materials and propose the design of new materials suitable for new technological applications.

The second objective of this thesis (Chapters 6 and 7) is to investigate the time re-

solved structural changes in semiconducting samarium mono-sulphide (SmS) crystal, induced by *fs*-laser heating. These structural changes are probed by focusing laser driven plasma *fs*-X-ray pulses using a toroidally bent crystal. SmS at atmospheric pressure is an ionic semiconductor of NaCl-type structure; at pressure of about 0.65-0.67 GPa, it undergoes semiconductor-to-metal phase transition (see Chapter 6). The phase transition involves the delocalization of a 4*f*-electron in Sm ion from 4*f* to 5*d* (i.e., it involves a $4f^6 \rightarrow 4f^5 5d^1$ Sm-ion configurational change) which implies the conversion of Sm^{2+} toward Sm^{3+} (Jayaraman *et al.*, 1970; Kirk *et al.*, 1972). Fluctuation of the valence in SmS ion directly causes a fluctuation in the ionic diameter and, because of the strong Coulomb attraction among the Sm ion and its surrounding chalcogen ions, it induces lattice distortion around the Sm ion. Therefore, these investigations contribute to understanding of time resolved response of SmS and provide insights into phase transition.

This thesis is organized as follows: In Chapter 2, the basic concepts of the vertical-geometry Johann spectrometer and the experimental set up used to investigate radiator-perturber interactions in hot and dense Al plasmas are outlined. Chapter 3 concentrates to demonstration of diagnostic potential contained in spectral line profiles. In Chapter 4, the shift of Al Ly γ line and merging of Al Ly ζ - θ into continuum is reported. In Chapter 5, the effects of the plasma waves and charge exchange in line profiles of Al Ly γ is presented. In Chapter 6, Sections 6.1 and 6.2, the special features and parameters that characterize the mixed-valent state, and the framework in which the experimental results can be understood are outlined. Section 6.3 is concerned with the X-ray analysis of the metallic phase, induced by polishing the SmS crystal, and semiconductor phase, induced by heating the metallic-phase SmS crystal. Finally, Chapter 7 presents the evidence of the controlled structure dynamics, i.e., generation and observation of strain pulses in the semiconductor phase of the SmS crystal. Additional topics which are intended to help understanding of material presented in this thesis are outlined in Appendices A to I.

Chapter 2

The Spectrometer and Experimental Setup

2.1 Introduction

X-ray spectroscopy is a widely used diagnostic tool in the study of laser produced plasmas (Hauer *et al.*, 1991). X-rays of moderate energy (from several hundred eV to tens of keV) emitted from such plasmas are one of few sources of detailed information on processes occurring in laser produced plasmas (LPPs). In this energy range, crystal spectroscopic methods are in general use. A variety of available crystals with different diffractive and mechanical properties offer the possibility to make an optimum choice of the dispersive element and spectroscopic scheme in accordance with the aims of diagnostics. Among the parameters relevant to optimization such as spectral range, luminosity, dispersion, spatial and spectral resolution, the last mentioned is probably the most important (Hauer *et al.*, 1991). Over the years, a number of spectroscopic schemes have been advocated for use in the diagnosis of LPPs; these include flat single crystal spectrometers (Renner *et al.*, 2004), von Hamos and toroidal focusing schemes (Hauer *et al.*, 1984; Misalla *et al.*, 1999), instruments working in the Johann mode (Förster *et al.*, 1992), elliptically bent crystals (Henke *et al.*, 1983), vertical dispersion mode double crystal spectrometer (He *et al.*, 1993; Renner *et al.*, 1995), vertical-dispersion Johann spectrometer and schemes involving the Renninger effect (Fraenkel, 1982). Among these instruments, unconventional spectrometers based on the vertical dispersion principle (Renner *et al.*, 1995, 1997a) attracted considerable interest due to their extraordinary characteristics. They combine extremely large linear dispersion, spectral and one-dimensional (1D) spatial resolution with a simultaneous production

of two-mirror symmetric spectra disposed about a central wavelength.

In hot and dense plasmas the emitters are influenced by the free electrons and surrounding ions. This leads to the broadening of the spectral lines (see Chapter 3), reduction of the binding energy and line shifts (see Chapter 4), appearance of dips (see Chapter 5) and satellites (Duston *et al.*, 1983; Leboucher-Dalimier *et al.*, 1993) in the line profiles. Since the emission spectrum emitted by ions embedded in such plasmas reflects the perturbed level structure, the precise measurement of the spectral line profiles is of great importance. The acquisition of high quality data necessary to prove the existence of the theoretically predicted spectroscopic features, or to validate sophisticated theories, is generally governed by two factors. First, the resolving power and the luminosity of the instrument must be high enough to permit collection of the data required. Second, the data must be collected from well-defined plasmas. The optimized sandwich-target geometry combined with data collection using the vertical dispersion Johann spectrometer can provide the required data. This Chapter presents the basic concepts of the vertical geometry Johann spectrometer and the experimental setup used to investigate the Lyman lines emitted from hot and dense Al plasmas.

Vertical-geometry Johann spectrometer (VJS) is a high resolution, high dispersion spectrometer, which is based on the principle of vertical dispersion, and which enables precise measurements of spectral lines having wavelength in the X-ray region. It has been successfully used in advanced plasma spectroscopy such as investigation of colliding plasmas and plasma induced line shifts in Lyman series of aluminum (Renner *et al.*, 1997a,b, 1998, 1999, 2003). A complete theoretical analysis of the spectrometer has been given by Renner *et al.* (1997a). The properties of this instrument such as luminosity and spectral resolution have been compared with those of the double-crystal vertical dispersion spectrometer (DCV), flat single crystal spectrometer (FC) and Johann classical scheme (JC) by Renner *et al.* (1994). The results show that the luminosity and spectral resolution of the DCV, FC, JC and VJS are in the ratio of approximately 1 : 4 : 40 : 600 and 1.00 : 0.31 : 0.98 : 0.80, respectively (these numbers may differ slightly due to the wavelength, type of the crystal and source size, but their common character remains unchanged).

In the next section, the basic properties of the apparatus and reconstruction of the spectra are surveyed.

2.2 Vertical-Geometry Johann Spectrometer (VJS)

2.2.1 Principle of VJS

Vertical-geometry Johann spectrometer (VJS) is fitted with a cylindrically bent crystal of a radius R , Figure 2.1(a). The active vertical dimension of the crystal is larger than the horizontal one and determines the range of diffracted wavelengths. Each ray emitted by the plasma source (defined by a horizontal divergence α and a vertical divergence φ , see Figure 2.1(a)), strikes the crystal at a Bragg angle given by (Schnopper and Kalata, 1969)

$$\sin \theta = \sin \theta_{0\alpha} \cos \varphi \quad (2.1a)$$

$$\cos \theta_{0\alpha} = \cos \theta_0 \cos \alpha \quad (2.1b)$$

where θ_0 is the central Bragg angle (defined by $\alpha = 0$ and $\varphi = 0$), φ is the vertical divergence angle and α is the horizontal divergence angle.

According to Bragg's law ($2d \sin \theta = \lambda$) and Eq.(2.1), and neglecting the horizontal divergence of the crystal* ($\alpha \rightarrow 0$), only that wavelength λ which satisfies the equation

$$\lambda = \lambda_0 \cos \varphi \quad (2.2)$$

is diffracted from the crystal (spectrometer) at a given φ . For each λ , reflection occurs at angles $\pm\varphi$; the rays with the wavelengths shorter than λ_0 are dispersed in the vertical direction symmetrically about the horizontal plane containing the central ray with a wavelength λ_0 . Figure 2.1(b) shows the scheme of the VJS where a polychromatic point source is used to illuminate the crystal. The wavelength range covered by the spectrometer is

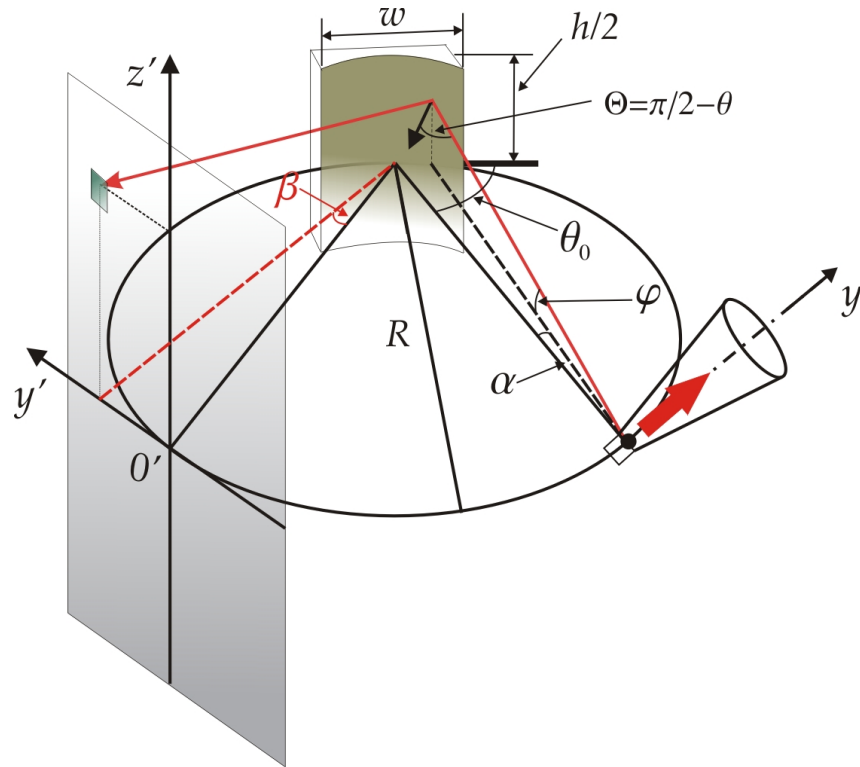
$$\begin{aligned} \Delta\lambda &= \lambda_0(1 - \cos \varphi_{\max}) \\ &= 2d \sin \theta_0(1 - \cos \varphi_{\max}) \end{aligned} \quad (2.3)$$

where

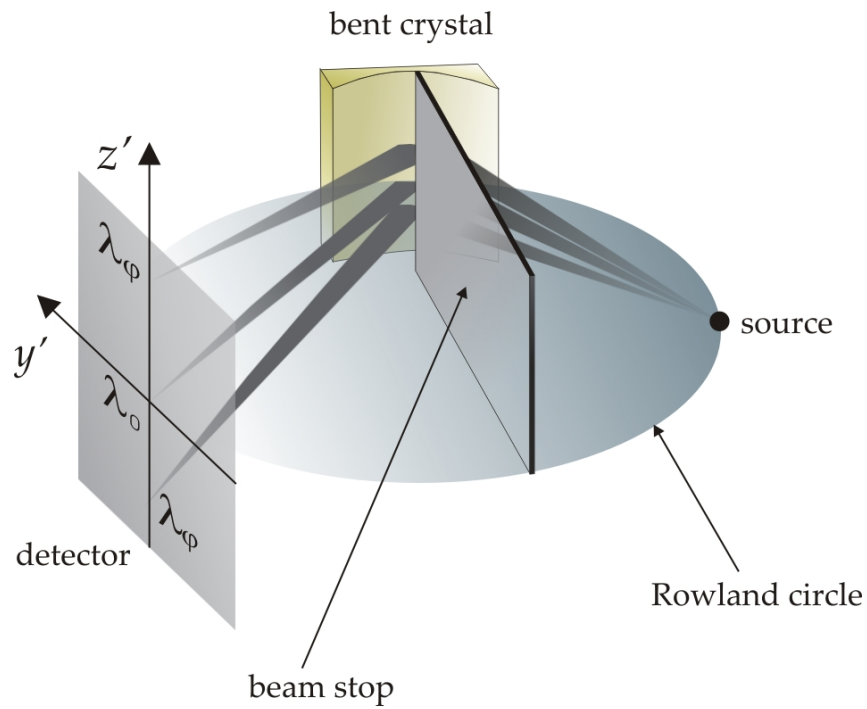
$$\varphi_{\max} = \tan^{-1} \left(\frac{h}{2R \sin \theta_0} \right) \quad (2.4)$$

Thus, for fixed θ_0 , the wavelength range covered by the spectrometer depends on the vertical size of the crystal h .

*The horizontal divergence can be decreased toward the negligible values by placing a beam stop in front of the crystal, as shown in Figure 2.1(b). Additionally, the horizontal size of the crystal (w), which determines the maximal horizontal divergence ($\alpha_{\max} \propto w/R$) is very small in comparison to the crystal-source distance.



(a)



(b)

Figure 2.1: Scheme of the vertical-geometry Johann spectrometer (VJS): (a) The spectrometer is fitted with a cylindrically bent crystal of a radius R , θ_0 is the central Bragg angle, θ is the Bragg angle at a given point in the crystal surface, α is the horizontal divergence angle, φ is the vertical divergence angle, λ_0 is the central wavelength, λ is the wavelength of the radiation diffracted at the angle φ , w is the horizontal size of the crystal and h is the vertical size of the crystal, (b) Radiation of wavelength λ is dispersed in the vertical direction symmetrically about the horizontal plane containing the central beam with a wavelength λ_0 .

The vertical dispersion of the spectrometer is found by differentiating Eq.(2.2)

$$\frac{d\varphi}{d\lambda} = -\frac{1}{\lambda \tan \varphi} \quad (2.5)$$

while the conventional dispersion (i.e., in the plane of incidence) follows from the Bragg condition, i.e.,

$$\frac{d\theta}{d\lambda} = \frac{\tan \theta}{\lambda} \quad (2.6)$$

Thus, the dispersion in the vertical direction for small φ is identical to that in the horizontal direction when the Bragg angle is close to $\pi/2$. High dispersion is an important parameter because it reduces the geometric apparatus smearing due to the finite size of the source, so that the spectral resolution close to the diffraction limit can be achieved at a reasonable source-to-detector distances (for VJS, typically about 100 mm) (Renner *et al.*, 1997a). Using extremely high dispersion at low angles φ (typically $|\varphi| < 12^\circ$), spectral line shifts and shapes can be accurately investigated; this is particularly true when the high dispersion is combined with another characteristic feature—the production of two sets of symmetric spectra.

The spectral resolution of the spectrometer ($\lambda/\Delta\lambda$) depends on the characteristics of the crystal used, on the source size (decreases with increasing source size) and on the angle φ (decreases with increasing φ) (Renner *et al.*, 1997a), and can reach the value of about 10000 (Renner *et al.*, 1994).

2.2.2 Reconstruction of the Spectra

The information contained in the two-dimensional (2D) detected intensity distribution must be reconstructed by computational procedure. The recorded spectral lines emitted from a quasi-linear source (e.g., constrained flow plasma) have an arched shape. Their arched character follows from variation of the angle of incidence θ_0 at sources extended along the y -axis. Figure 2.2 shows the scheme of the spectral profile formation at the detector. The source and the detector are positioned at the Rowland circle. The detector is normal to the central ray and the spectrum consist of two spectral lines with wavelengths λ_1 and λ_2 ($\lambda_1 > \lambda_2$). The emission from the points P_n and P_{-n} , which are located outside the Rowland circle, is diffracted in the detector plane at y'_n and y'_{-n} , respectively. Thus, if the point P_0 is located at the target surface (target surface is perpendicular to y , see Figure 2.2), then, intensity distribution at $y' > 0$ corresponds

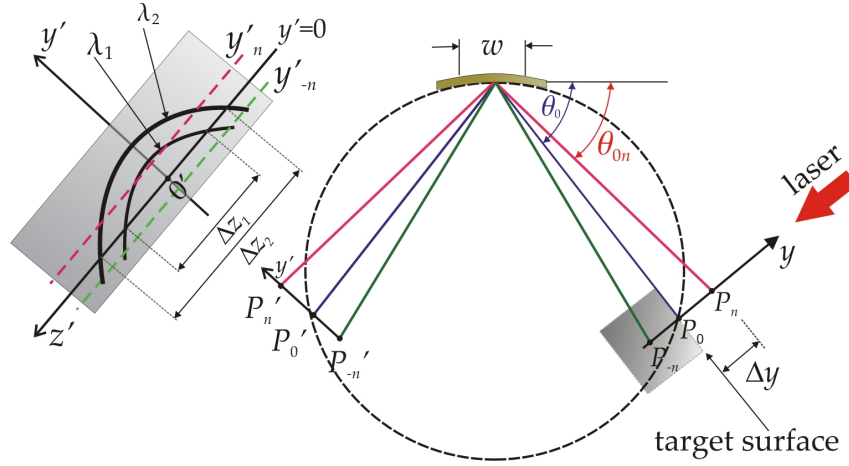


Figure 2.2: Radiation with wavelength λ_1 and λ_2 ($\lambda_1 > \lambda_2$) emitted from central point P_0 are diffracted at angles $\varphi_{1,2} = \cos^{-1}(\lambda_{1,2}/\lambda_0)$, symmetrically disposed about y' -axis i.e. through z' -axis. The emission from the points P_n , P_0 and P_{-n} , is dispersed in the detector plane containing P'_n , P'_0 and P'_{-n} , respectively.

to the emission above the irradiated target surface, and, at $y' < 0$ the intensity distribution corresponds to the emission below the irradiated target surface (i.e., in the blow-off crater). Rays with wavelength λ_1 and λ_2 emitted from the central point P_0 are diffracted at angles $\varphi_{1,2} = \cos^{-1}(\lambda_{1,2}/\lambda_0)$, symmetrically disposed about y' -axis. By moving from P_0 to P_n , the horizontal glancing angle

$$\Delta\theta_{0n} = \theta_0 - \theta_{0n} = \tan^{-1} \left[\frac{\Delta y}{R \sin \theta_0} \right] \quad (2.7)$$

decreases, thus the maximum wavelength that can be dispersed also decreases to $\lambda_{0n} = 2d \sin(\theta_0 - \Delta\theta_{0n})$. Consequently, the spacing

$$\Delta z_n = \frac{4R \sin \theta_0 \tan \varphi_n}{\cos(\Delta\theta_{0n})} \quad (2.8)$$

between symmetric-spectral features decreases in comparison to the case of $y = 0$.

The intensity distribution recorded in the X-ray film is digitized by densitometering the film.[†] Figure 2.3 shows a typical densitogram of the spectrum emitted from a laser irradiated Al-sandwich target. The recorded spectral lines are nearly symmetric with respect central wavelength λ_0 ; small deviations from the full symmetry can be explained by a statistical character of the detected x-ray fluxes and small angular misalignment during densitometering procedure. The intensity value in each pixel of the digitized image in Figure 2.3 is related to wavelength using

$$\lambda(y', z') = 2d \frac{\frac{y'}{R} \cos \theta_0 + \sin^2 \theta_0}{\sqrt{\sin^2 \theta_0 + \frac{y'^2}{R^2} + \frac{z'^2}{4R^2}}} \quad (2.9)$$

[†]The typical values of the pixel size are $8 \mu\text{m}$ in y' direction and $100 \mu\text{m}$ in z' direction.

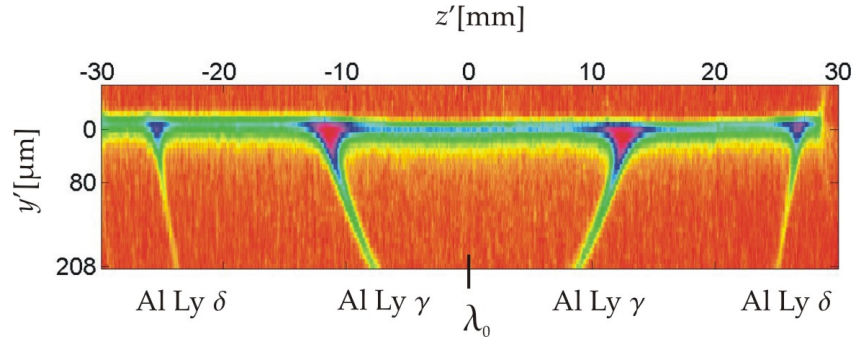


Figure 2.3: A typical densitogram of the spectrum emitted from an Al foil ($20 \mu\text{m}$ thick) sandwiched between two CH substrates (each $20 \mu\text{m}$ thick) irradiated at laser energy of 4.4 J .

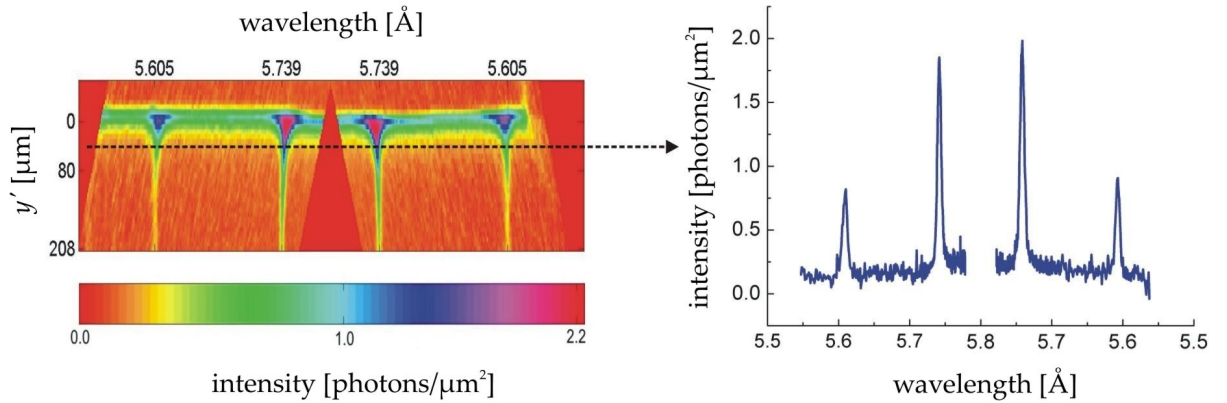


Figure 2.4: The reconstructed spectrum of that shown in Figure 2.3. It shows the Al Ly γ (vacuum wavelength $\lambda_{0,\gamma} = 5.739 \text{ \AA}$) and δ ($\lambda_{0,\delta} = 5.605 \text{ \AA}$), up to $208 \mu\text{m}$ from the target surface.

which is obtained using Eqs.(2.2), (2.7) and (2.8). The reconstructed spectrum produced from the densitogram presented in Figure 2.3 (showing the Al Ly γ and δ emission up to the distance of $208 \mu\text{m}$ from the target surface) is shown in Figure 2.4. To minimize errors introduced by the line shift and opacity effects, λ_0 was determined by measuring the spacing between centers of Al Ly γ lines at $y' = 168 \mu\text{m}$ and by using Eqs.(2.2) and (2.7).

2.3 Experimental Setup

The experiments dedicated to investigate the influence of the intermediately coupled plasma environment on the radiating ions were carried out on the nanosecond laser facility at the LULI, Ecole Polytechnique, Palaiseau (France). The scheme of the experimental geometry is shown in Figure 2.5. A single laser beam delivering up to 20 J of the frequency-quadrupled radiation ($0.263 \mu\text{m}$) in a pulse length of 0.5 ns was focused to a spot with a diameter of $80\text{-}100 \mu\text{m}$, yielding intensity of the order of 10^{14}

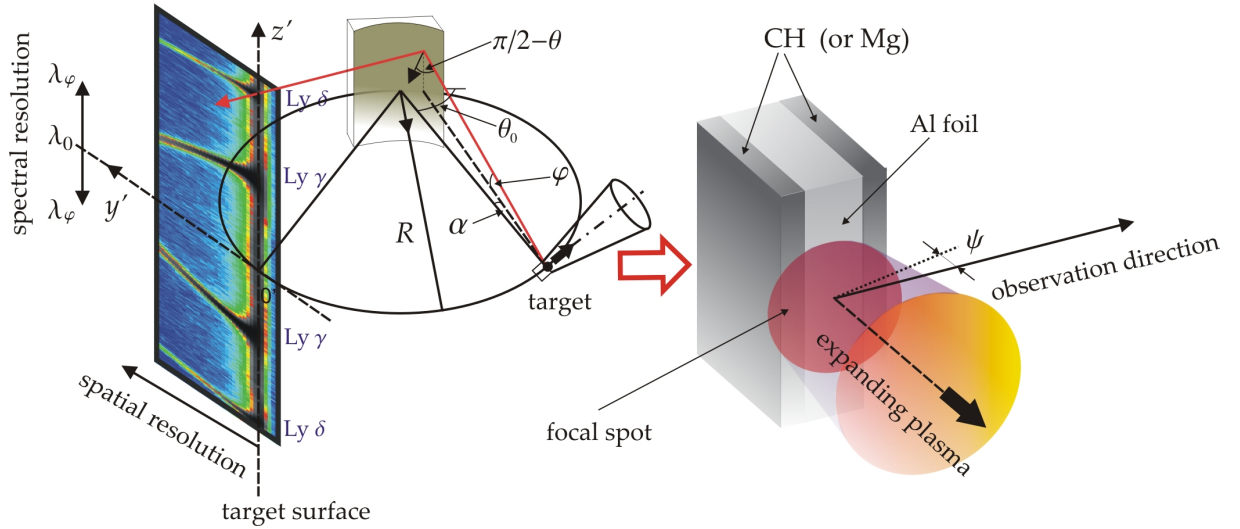


Figure 2.5: The spectrometer and the geometry of the target. θ_0 is the central Bragg angle, θ is the Bragg angle at a given point in the crystal surface, α is the horizontal divergence angle, φ is the vertical divergence angle, λ_0 is the central wavelength, λ is the wavelength of the radiation diffracted at the angle φ , and ψ is the angle of observation with respect to the target surface. The instrument is equipped with a crystal of quartz (100) cylindrically bent to a radius of 77.2 mm and produces two identical symmetric spectra.

Wcm^{-2} . The radiation was incident onto a structured target consisting of aluminum foil (with thickness ranging from 5-50 μm), sandwiched between two CH or Mg foils (each with thickness ranging from 5-25 μm). By placing the sandwiched target through the center of the focal spot, the Al plasma was confined in a constrained flow by the substrate plasma, the lateral gradients were suppressed and the effective plasma parameters were optimized to the values favorable for collection of the data which are needed for investigations presented in Chapters 3-5. Close to the irradiated target surface, hydrodynamic simulations (Christiansen *et al.*, 1974) estimate the electron density and temperature to about $3 \times 10^{22} \text{ cm}^{-3}$ and 300 eV, whereas at 100 μm from the target surface to about $2 \times 10^{21} \text{ cm}^{-3}$ and 840 eV, respectively; this result suggests that the plasma is expected to be intermediately coupled, with plasma coupling constant Γ between about 0.1 and 0.7, see Appendix B.

The spectra were observed at an angle of $\psi = 2.0^\circ \pm 0.7^\circ$ to the irradiated target surface by using the vertical-geometry Johann spectrometer. The instrument is equipped with a crystal of quartz (100), $2d = 8.5084 \text{ \AA}$, cylindrically bent to a radius of 77.2 mm, and with effective area of $2 \times 30 \text{ mm}^2$ (horizontal \times vertical). The ray tracing calculations (Renner, 2004b) suggest that for the Al Ly β , γ and δ , the VJS provides spectral resolution of 4240, 4150 and 4070, respectively. The spectra were recorded on the x-ray film Kodak Industrex CX.

Chapter 3

Spectral Line Broadening and Profile Modifications in Hot and Dense Aluminum Plasmas

3.1 Introduction

Spectral lines emitted from ions in plasmas, due to high density, high temperature, expansion and absorption, are broadened, shifted and asymmetric compared to line profiles emitted from isolated ions. The broadening mechanisms* which may be important in a plasma are (Cooper, 1966): (i) *natural line broadening*, due to the finite life time of the excited state, (ii) *Doppler broadening*, due to thermal motion of the radiating ions, (iii) *electron impact broadening*, due to collisions of electrons with the radiating ions, (iv) *quasi-static Stark broadening*, due to microfields generated by perturbing ions, and (v) *opacity broadening*, due to transport of emission from the region of radiation to the observing instrument (Hauer and Baldis, 1989; Salzmänn, 1998). In a low density plasmas, Doppler broadening is generally the dominant mechanism, while for higher plasma densities (higher than 10^{18} cm^{-3} for Al plasma at $T = 700 \text{ eV}$; Griem, 1974), the plasma microfields generally broaden the line through the Stark effect, and the Stark broadening may then govern the line shape (Calisti *et al.*, 1990).

The analysis of Stark-broadened spectral line profiles is one of the most common methods for plasma diagnosis from the beginning of the 1960s (see e.g. Griem, 1974). Since the shape of these profiles depends on the electron density, Stark broadening has been widely used as a density diagnostics of wide range of plasma conditions such as stellar atmospheres (Pagel, 1971; Griem, 1974) and plasmas relevant to inertial

*See Appendix C for a brief review.

confinement fusion (ICF) (Hauer *et al.*, 1980; Kilkenny *et al.*, 1980; Hooper Jr. *et al.*, 1989; Haynes Jr *et al.*, 1996). In particular, in the case of ICF, the glass-encapsulated targets containing fusion fuel (deuterium and tritium) can be doped with a small amount of high-Z impurity (such as argon or neon) and then, for expected density-temperature conditions produced by implosion, it will be possible to observe spectral lines of the impurity ions which are broadened (Haynes Jr *et al.*, 1996). The basic theory and an overview of the Stark broadening has been presented by Griem (1974). More recent advances are reported by Junkel *et al.* (2000).

To give a proper diagnosis of the plasma, the information contained in the emission spectrum is related to both the atomic physics of the ionic emitters and to the plasma physics of the environment. The standard method of analysis involves comparison of an experimental spectrum with calculation carried out at fixed temperature and electron density. The electron density and temperature used in the best fit of the synthetic spectra with the experimental data are then considered to characterize the emitting region. This chapter concentrates to demonstration of diagnostic potential contained in spectral line profiles. Additionally, a strong asymmetry of the Al Ly β and γ lines measured at Al irradiated foils is observed. Some brief excerpt of the line profile formalism and its diagnostic application are outlined in Section 3.2. The consistency of line profile formalism to provide diagnostic information, and the observed asymmetries in Al Ly β and γ , are shown in Section 3.3.

3.2 Diagnosis of Hot and Dense Plasmas Based on the Spectral Line Profile Analysis

For an ion undergoing spontaneous electric dipole transition in the presence of a plasma, the intensity distribution of the emitted radiation is given by (Tighe and Hooper, Jr, 1976)

$$I(\omega) = \int_0^{\infty} P(\epsilon) J(\omega, \epsilon) d\epsilon \quad (3.1)$$

where $P(\epsilon)$ is the quasistatic microfield distribution (i.e., the probability distribution function for finding a given electric field ϵ at the radiator immersed in a plasma) and $J(\omega, \epsilon)$ represents collisional broadened line profile (due to impact with electrons) in the presence of the static ion microfield ϵ . Therefore $J(\omega, \epsilon)$ is essentially the dynamic line profile and the total line shape is a convolution of the collisional and quasistatic

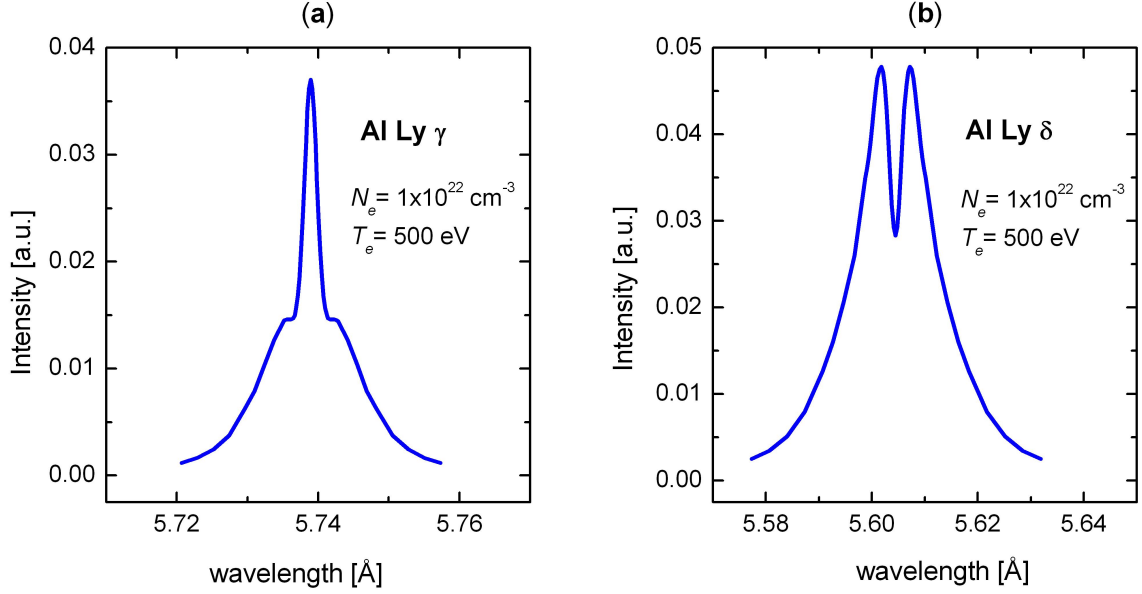


Figure 3.1: (a) Line profile of aluminum Lyman γ (vacuum wavelength $\lambda_{\gamma,0} = 5.739 \text{ \AA}$), calculated using the code FLY, corresponding to electron density $N_e = 1 \times 10^{22} \text{ cm}^{-3}$ and electron temperature $T_e = 500 \text{ eV}$, (b) line profile of aluminum Lyman δ (vacuum wavelength $\lambda_{\delta,0} = 5.605 \text{ \AA}$), calculated using the code FLY, corresponding to electron density $N_e = 1 \times 10^{22} \text{ cm}^{-3}$ and electron temperature $T_e = 500 \text{ eV}$.

contributions. The formalisms concerning calculation of $P(\epsilon)$, $J(\omega, \epsilon)$ and $I(\omega)$ can be found in e.g. Griem (1974), Tighe and Hooper, Jr (1976) and Lee (1979a).

The spectral line profiles given by Eq.(3.1), for hydrogen-like aluminium Lyman lines, can be calculated using the non-local-thermodynamic-equilibrium atomic physics code FLY (Lee and Larsen, 1996). The form of the impact profile, $J(\omega, \epsilon)$, is a Lorentzian with a frequency dependent width operator

$$J(\omega, \epsilon) \propto \frac{\text{Im}}{\pi} [\Delta\omega(\epsilon) - iG(\Delta\omega, \epsilon)]^{-1} \quad (3.2)$$

where $\Delta\omega$ is the separation from the line center of a transition from an upper state, u , to a lower state, l . This separation is dependent on the plasma field ϵ , so that $\Delta\omega = \omega - \omega_{ul}(\epsilon)$. The G function is the electron broadening operator which is essentially the cross section for interactions between the radiating ion and the electron subsystem (Lee, 1995), and $i = \sqrt{-1}$. Calculation of $P(\epsilon)$ follows the formalism given by Iglesias *et al.* (1985).

Figures 3.1(a,b) show the line profiles of Al Ly γ and δ calculated using the code FLY at the electron density $N_e = 1 \times 10^{22} \text{ cm}^{-3}$ and electron temperature $T_e = 500 \text{ eV}$. The spectral line profiles which arise from the even principal quantum numbers $n = 2, 4, 6, \dots$ (i.e., Lyman α , γ , ϵ , etc.) have a sharp spike which sits on the shoulders provided largely by ion contributions; the sharp spike is result of the electron contribu-

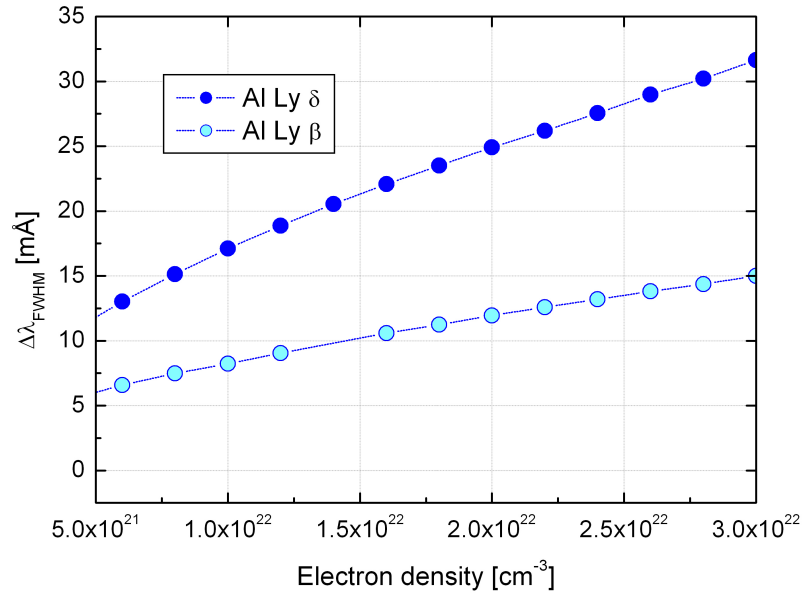


Figure 3.2: The full width at half maximum (FWHM) of aluminum Lyman β and δ derived by means of the code FLY.

tions. These line profiles contain an unshifted central component that is unperturbed by the ion fields and is broadened only by electron impact. The width (FWHM) of these spectral line profiles show a *non-monotonic* behavior with the electron density, i.e., there is a region where there is a decrease of FWHM with increasing electron density followed by monotonic-increase again. Because of this behavior, the line-widths of these spectral lines (Lyman α , γ , ϵ , etc.) *do not* provide reliable diagnostic information (Lee, 1985). In distinction, the width of spectral lines which arise from odd principal quantum number states $n = 3, 5, 7, \dots$ (i.e., Lyman β , δ , ζ , etc.) show a monotonic behavior at high densities and *can* be used for diagnostic purposes. The line profiles of these transitions have a central dip whose depth depends on the ion dynamics and opacity. Haynes Jr et al. (1996) showed that inclusion of the ion dynamics and opacity in calculations contribute to the reduction of the central dip. Figure 3.2 displays the dependence of the FWHM of aluminum Ly β and δ as a function of electron density derived by means of the code FLY. It is obvious that for the same value of electron density Al Ly δ line is broader than Al Ly β , which is due to the fact that the width of a spectral line increases with n .

Using theoretical calculations to generate Ly β and δ Stark-broadened line profiles, Lee (1985) found a simple parametrization of the FWHM over a broad range of the

Table 3.1: Values of the parametrization shown in Eq.(3.3)

Line	T_e [eV]	A	B	C	D
β	250	2.669	-1.252	0.546	-0.008
δ	250	6.959	-1.270	0.563	-0.007
β	500	3.353	-1.055	0.559	-0.009
δ	500	8.370	-1.132	0.586	-0.009
β	1000	3.970	-0.893	0.582	-0.009
δ	1000	9.721	-0.975	0.604	-0.009

atomic species [$Z \in (6, 18)$], electron density [$N_e \in (10^{19}, 10^{25}) \text{ cm}^{-3}$], and electron temperature ($T_e = 250, 500, 1000 \text{ eV}$). The result is

$$\Delta\lambda_{\text{FWHM}}[\text{m}\text{\AA}] = A \times 8.066 \times 10^{-2} (\lambda_0[\text{\AA}])^2 \left(\frac{12}{Z}\right)^B \left(\frac{N_e[\text{cm}^{-3}]}{10^{22}}\right)^{C+(Z-12)D} \quad (3.3)$$

where λ_0 is the unperturbed wavelength. The values of parametrization shown in Eq. (3.3) are given in Table 3.2. The result yields an electron density diagnostics accurate to about 20 %.

3.3 Experimental Results and Discussion

Figure 3.3 shows the measured line profiles of Ly γ and δ emitted from the laser irradiated Al foil, 50 μm thick, sandwiched between two CH substrates, each 25 μm thick. The spectral lines are emitted from regions located at 16, 24, 32, 48 and 64 μm from the target surface. The increased broadening of spectral lines, as the distance from the target surface is decreased, is evident. Also, Ly δ is broadened more than Ly γ . As shown in the previous section, this happens because the line width (FWHM) of a spectral line increases with electron density and principal quantum number of the upper transition level. The measured spectra are symmetric and well fitted by a Lorentz function of the form

$$I(\lambda) = I_0(\lambda) + \frac{2A}{\pi} \frac{w}{4(\lambda - \lambda_c)^2 + w^2} \quad (3.4)$$

where A is the area under the curve, w is full width at half maximum, and λ_c is the center of the line. The measured FWHM of Al Ly δ increases from about 7 m \AA observed at 64 μm from the target surface to about 23 m \AA at 16 μm close to the target surface. The observed line widths (FWHM) are attributed to electron densities by using the code

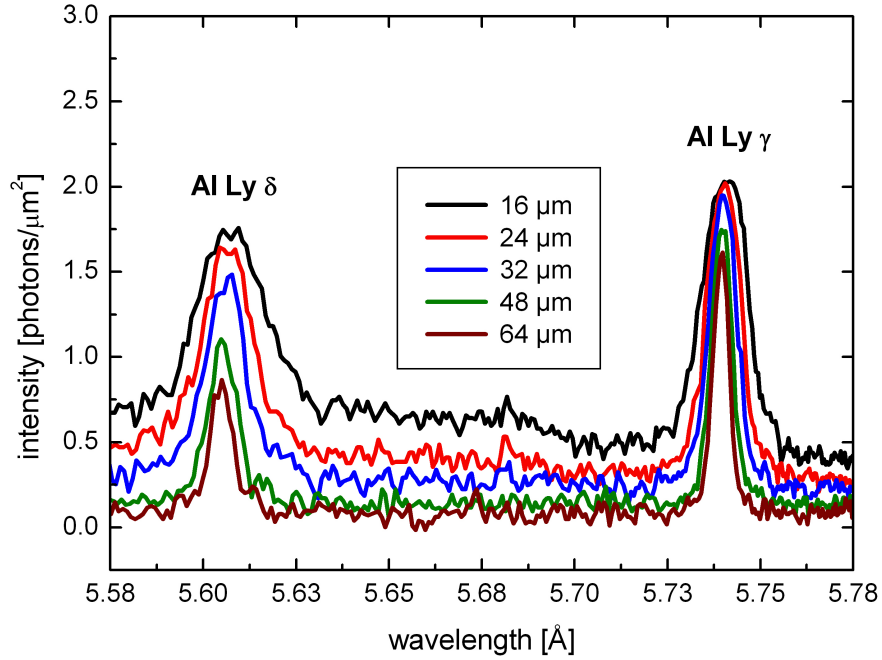


Figure 3.3: The measured line profiles of Al Ly γ (vacuum wavelength $\lambda_{\gamma,0} = 5.739 \text{ \AA}$) and δ ($\lambda_{\delta,0} = 5.605 \text{ \AA}$) emitted from Al irradiated target ($50 \mu\text{m}$ thick). Laser energy: 3.3 J.

FLY. The variable used to obtain fits of theoretical line profiles with the measured ones was N_e (electron density). Electron temperatures of the emitting regions are provided from simulations with hydrocode MEDUSA in a planar geometry (see next chapter).[†] The line widths of Ly γ are not used to derive electron densities, because, as mentioned in the previous section, they do not show monotonic behavior with electron density and thus cannot guarantee unambiguous determination of the density. The quality of fits is displayed in Figures 3.4(a,b) where Ly δ line profiles emitted at 32 and 64 μm from the target surface, respectively, are compared with synthetic spectra generated by the code FLY. The electron densities were optimized to best fit each of the experimental line outs. At these regions, an excellent agreement is found for electron densities of $6 \times 10^{21} \text{ cm}^{-3}$ and $2 \times 10^{21} \text{ cm}^{-3}$, respectively. Near the target surface the synthetic spectra do not fit well the line wings of Ly δ . This discrepancy can be attributed to a possible satellite creation.

The consistency of this method, in providing diagnostic information, is demon-

[†]Stark-broadened shapes and positions of spectral lines depend relatively weakly on temperature (for a temperature change in the range 500 – 2000 eV the density derived from the width changes up to $\pm 12\%$ (Renner *et al.* 2003)).

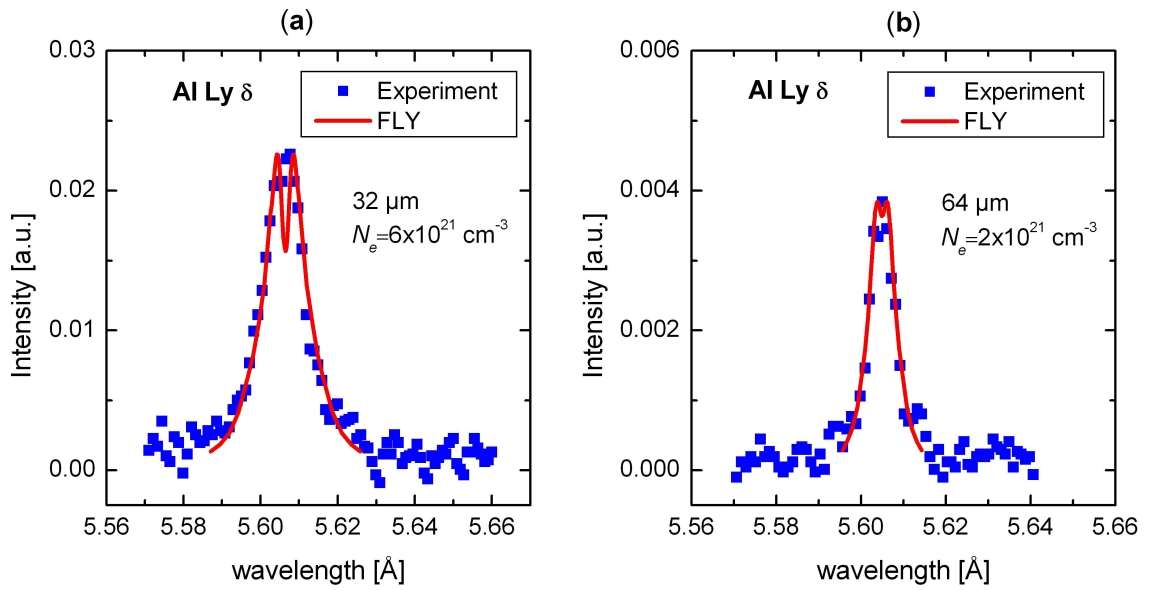


Figure 3.4: The fit of aluminum Ly δ experimental profiles, emitted at (a) 32 μm and (b) 64 μm from the target surface, with theoretical line profiles generated by means of the code FLY. The spectra are emitted from laser irradiated Al foil, 50 μm thick, sandwiched between two CH substrates, each 25 μm thick.

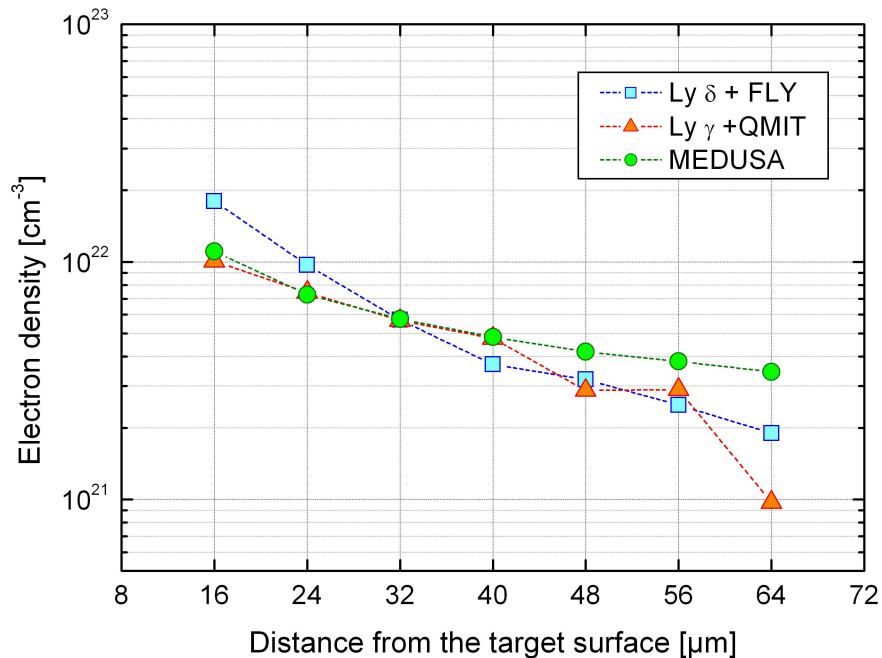


Figure 3.5: Comparison of electron densities deduced by FLY and measured FWHM of Al Ly δ with those derived from measured Al Ly γ shifts and QMIT, and hydrodynamic simulations with MEDUSA (target: Al, 50 μm thick, sandwiched between two CH substrates (each 25 μm thick)).

strated in Figure 3.5, where the electron densities deduced by means of FLY and measured widths of Al Ly δ are compared with electron densities inferred from measured Al Ly γ shifts[‡] and hydrodynamic simulations with MEDUSA in planar geometry. The electron densities deduced by FLY and experimentally measured widths compare favorably with those deduced from line shifts. The discrepancy in densities, except near the surface and at 64 μm , is less than 26%; this corresponds well to the accuracy of the standard density diagnostics based on Stark-broadened line profile analysis, which is estimated to about 20% (Lee, 1985).

At laser irradiated Al foils, where the expanding plasma is not laterally constrained, a strong asymmetry of Ly β and γ is observed. Figures 3.6(a) and 3.7(a) display Ly β and γ profiles emitted from Al foil targets at different distances from the target surface, measured at laser energies 3.5 J and 6.4 J, respectively. From the spectra displayed in the Figure 3.6(a) it is evident that Ly β profiles show an asymmetry in the red side (i.e., in the side of longer wavelengths). The asymmetry is increased with increasing distance from the target surface, i.e., with decreasing of plasma density. In contrast to the Ly β profiles which show the asymmetry in the red side, at Ly γ profiles the asymmetry is very strong in the blue side (i.e., in the side of shorter wavelengths), Figure 3.7(a). Similarly to the Ly β case, the asymmetry in line profiles increases with increase of the distance from the target surface, i.e. with decrease of the density.

At Al sandwich targets the asymmetry of the spectral lines is much less evident. In Figures 3.6(b) and 3.7(b), the Ly β and γ profiles from Al sandwich targets at different distances from the target surface are shown. They are measured at laser energies 3.8 J, and 5.2 J, respectively. It is obvious that they are almost symmetric.

The experimental spectra shown in Figures 3.6 and 3.7 indicate that the observed asymmetry is related with the *spatial constraint* of the plasma. Indeed, in laterally unconstrained plasmas, the radiating ions experience electric- and velocity-field inhomogeneities which lead to asymmetries in spectral line profiles. This tentative interpretation is based on the discussions of Joyce *et al.* (1987), Wark *et al.* (1994), Murillo *et al.* (1997) and Patel *et al.* (2000). Wark *et al.* (1994) and Patel *et al.* (2000) observed and discussed the asymmetry in Al Ly α line profile. Their interpretation of asymmetry is mainly based on the plasma velocity fields along the line of sight which change the

[‡]The line shifts are converted to electron densities by using the quantum-mechanical-impact theory (see next chapter).

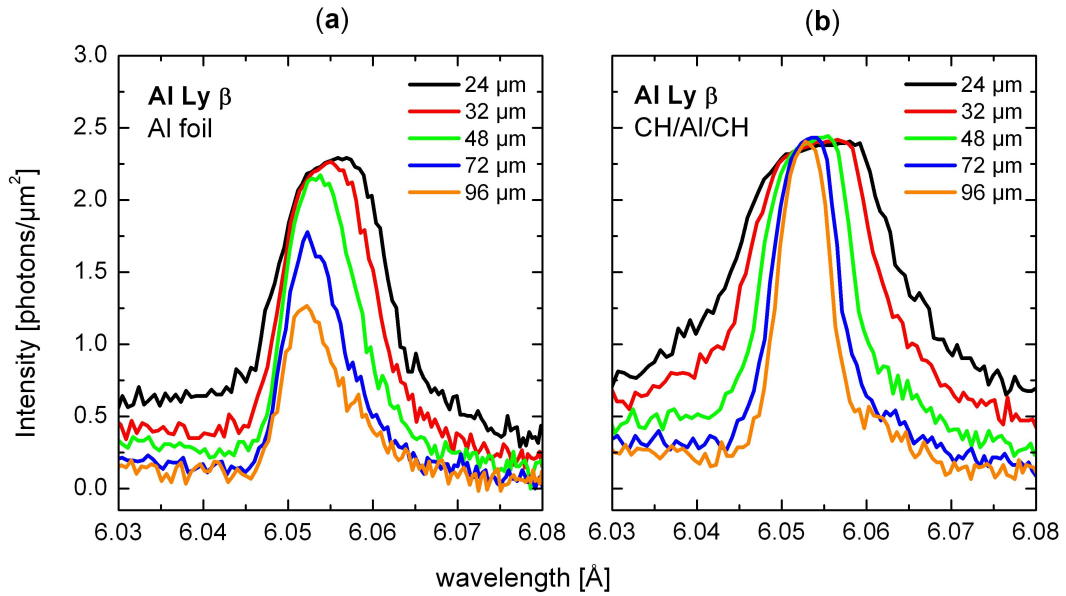


Figure 3.6: Al Ly β profiles emitted from: (a) Al foil (20 μm thick), and (b) CH/Al/CH target (Al foil, 20 μm thick, sandwiched between 40 μm CH).

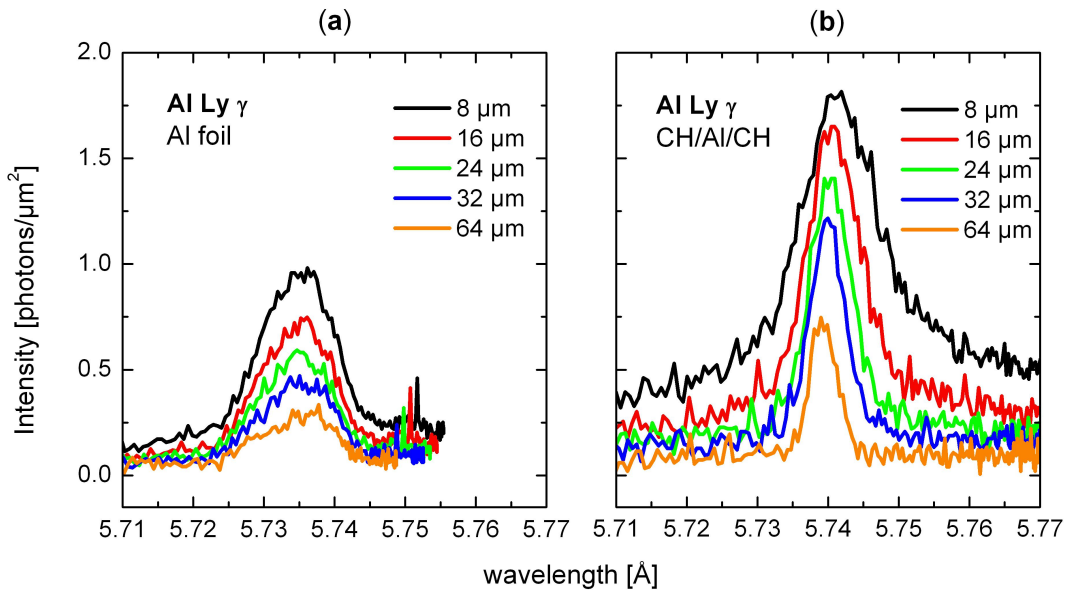


Figure 3.7: Al Ly γ profiles emitted from: (a) Al foil (20 μm thick), and (b) CH/Al/CH target (Al foil, 20 μm thick, sandwiched between 40 μm CH).

local values of emissivity and opacity. On the other hand, *Joyce et al. (1987)*, who discussed the asymmetry in Ly $\alpha - \gamma$, supposed that the asymmetry is mainly introduced by quadrupole interaction, quadratic Stark effect and fine structure splitting which modify the energy levels of a radiator. Further, *Koshelev (1988)* proposed an alternative explanation on the basis of the physics of dielectronic satellites. He claims that in a hot and dense plasmas, dielectronic satellites can make a significant contribution to asymmetry in a line profile, particularly in the red wing. These spectra seem to suggest also, that the observed asymmetry should be related to the inner structure modifications of radiating ions. In previous section it is shown that the spectral line profiles which arise from the odd principal quantum numbers (to which belongs Ly β) have a central dip and those profiles which arise from the even principal quantum numbers (to which belongs Ly γ) have a spike which sits between two shoulders. This fact may indicate that these lines 'feel' the perturbation by gradient fields differently due to their specific dependence on the principal quantum number of the upper transition level. However, the question whether the observed asymmetry should be related to electric field gradients, Doppler shifted reabsorption, dielectronic satellites or combination of all of them, is still open. An reliable answer to it should stimulate further experiments with appropriately defined conditions, aimed to observe asymmetry in higher Lyman transitions (Ly δ , ϵ and ζ), in order to confirm the dependence of the red-, blue-asymmetry on the principal quantum number and on the electron density. This effort should be accompanied with the development of advanced theories for calculation of spectral lines, which take into account the effects induced by field gradients, radiation transport and dielectronic satellites, as well.

3.4 Summary and Conclusions

The high dispersion, spatially resolved spectra emitted from constrained and unconstrained Al plasmas are measured and analyzed. The widths of Al Ly δ were interpreted in terms of variable density distribution in the expanding plasma by using the atomic physics approach. The densities derived from the measured Ly δ line widths are consistent (to within 26%) with those derived from line shifts and plasma simulations.

At Al irradiated foils, where the plasma is not laterally constrained, the Ly β profiles show asymmetry in the red side, whereas Ly γ profiles show asymmetry in the

blue side. The asymmetry increases with increasing distance from the target surface, i.e., with decreasing of plasma density. At Al sandwich targets, where the plasma is laterally constrained (and the plasma gradients are suppressed) the asymmetry is very weak. This behavior of spectral lines can be qualitatively explained by an interplay of (i) Doppler shifted reabsorption of the lines in expanding plasmas with high lateral gradients (in comparison to sandwiched plasmas), (ii) ion quadrupole interaction, (iii) quadratic Stark effect, (iv) fine structure splitting, and (v) possible dielectronic satellite creation. Because of the absence of a reliable theoretical models which relate the red-, blue-asymmetry to the principal quantum number and plasma density, the question whether the observed asymmetry should be related to electric field gradients, Doppler shifted reabsorption, dielectronic satellites or combination of all of them, remains still open.

Chapter 4

Line Shift and Merging in Hot and Dense Al Plasmas

4.1 Introduction

The wavelength shift of spectral lines emitted from hot and dense plasmas, also called *plasma polarization shift*, is a plasma effect generated by the modification of the ionic potential by the plasma environment (free electrons and ions). An excess of the negative charge, which partly lies within the bound electron orbits, partially shields the nuclear charge, thus altering the energy level structure of the emitter. As a result, the energy of the photon emitted during a transition between two levels will be different in comparison to the case when the ion is isolated (i.e., it is not immersed in a plasma) (Salzmann, 1998). Theoretical predictions indicate that the ion induced shift is substantially smaller than electron effects, because the ion gas has not enough time to be effectively polarized (because the ions are more massive than the electrons), therefore most of line shift models relate the spectral line shift to the polarization of the negative charge around the ionic nucleus (Nguyen *et al.*, 1986).

The interest in plasma polarization shift follows from both theoretical and experimental aspects. Reliable identification of this effect provides a very sensitive mapping of free electron distribution within the ionic volume (Salzmann, 1998), can be used to diagnose hot and dense plasmas (Skupsky, 1980), and provides insight into the atomic properties of ions immersed in hot and dense plasmas.

The theory of line shift was developed in a series of papers during the 1970's and 1980's (see e.g. Salzmann, 1998). Skupsky (1980) suggested application of line shift of neon Lyman α to measure the density in the region anticipated for high-compression

laser fusion experiments. Calculation of the shifts involved solution of the Schrödinger equation in a self-consistent potential determined by the nucleus and the distribution of the free electrons and neighboring ions. [Nguyen *et al.* \(1986\)](#) developed a self-consistent-field model to describe the high density effects on atomic bound states, and quantum-mechanical-impact calculations to obtain line shifts. The quantum-mechanical-impact calculations consider a dynamical treatment between bound and free electrons. Recently, [Junkel *et al.* \(2000\)](#) presented a full Coulomb multi-electron formalism from which line shifts and asymmetry arise. The calculated line shifts are consistent with those predicted by [Griem \(1988a\)](#). A self-consistent-field and quantum-mechanical-impact calculations for line shifts of He-like ions were presented by [Koenig *et al.* \(1988\)](#).

The experimental results of the earlier line shift investigations described in [Volonté \(1978\)](#) were partly contradictory in reporting either red, blue or no shift of the spectral lines. Experiments with low- Z radiators ($Z = 1$ to 3) ([Grützmacher and Wende, 1978](#); [Pittman and Fleurier, 1986](#); [Böddeker *et al.*, 1993](#); [Jamelot *et al.*, 1990](#)) have confirmed that spectral lines are red shifted. In particular, [Böddeker *et al.* \(1993\)](#) measured the position of the Lyman α line of hydrogen atoms and results of these experiments were in good agreement with computations of [Griem \(1988a\)](#). Although line shifts in low- Z plasmas have been observed for many years (since 1970's), their observation at higher- Z plasmas was achieved during 1990's. Observation of line shifts in higher- Z plasmas is a difficult problem. Generally, shifts smaller than a line widths are expected to be observable at high-density plasma, where other effects, such as continuum lowering (see next Section), spectral line broadening ([Salzmann, 1998](#)), and line profile modifications due to radiative transport effects ([Wark *et al.*, 1994](#)) may obscure the shift of interest. This difficulty is overcome with the progress made in the design of sophisticated X-ray spectrometers with high resolution and luminosity. [Renner *et al.* \(1997, 1998\)](#) used aluminum microdot targets (which produce quasi-one-dimensional plasma) and high-dispersion X-ray spectrometer to record line profiles of aluminum Lyman $\alpha - \eta$. The red shifts observed for transitions $\gamma - \eta$ were consistent with predictions of the quantum-mechanical-impact theory ([Nguyen *et al.*, 1986](#)). More recently, [Woolsey *et al.* \(2000\)](#) and [Seamann *et al.* \(1999\)](#) reported red shifts in the He β lines of K-shell argon and aluminum, respectively, both roughly consistent with the results of [Nguyen *et al.* \(1986\)](#).

The experimental identification of line shifts in high- Z plasmas is greatly simplified if the plasma is not subjected to temperature and density gradients, and by using advanced spectrometers. These demands can be reached by using sandwich-target geometry (see Chapter 2, Section 2.3) and high-resolution vertical-geometry Johann spectrometer (see Chapter 2, Section 2.2). In this chapter, the shift of Al Ly γ line and merging of Al Ly $\zeta - \theta$ into continuum are reported. The Al plasmas were produced by irradiating Al foils, sandwiched between CH (and Mg) substrates. The substrates constrained the plasma into a columnar flow with small transverse velocities. The shifts were measured as a function of a distance from the target surface, and are compared with line shift estimates based on the theoretical results outlined in the next Section.

4.2 Theoretical Background

Interaction of the radiating ion with a plasma environment introduces plasma potential, $V_{pl}(\mathbf{r})$, as a new term in the Hamiltonian of the radiating ion. Plasma potential (see Appendix B) influences various ionic states of the radiator slightly differently, thereby modifying the energy levels (Figure 4.1) and corresponding wave functions. The energy levels of the radiator immersed in the plasma are shifted toward the continuum i.e., binding energy of electrons in the various states is reduced in comparison to the isolated ion case. The reduction of the binding energy is increased when the electron density increases; this phenomenon is known as *continuum lowering* or *ionization potential lowering*. The upward shift, χ_{nl} , of the energy level E_{nl} is

$$\chi_{nl} = E_{nl} - E_{nl}^0 = \langle nl | -eV_{pl} | nl \rangle \quad (4.1)$$

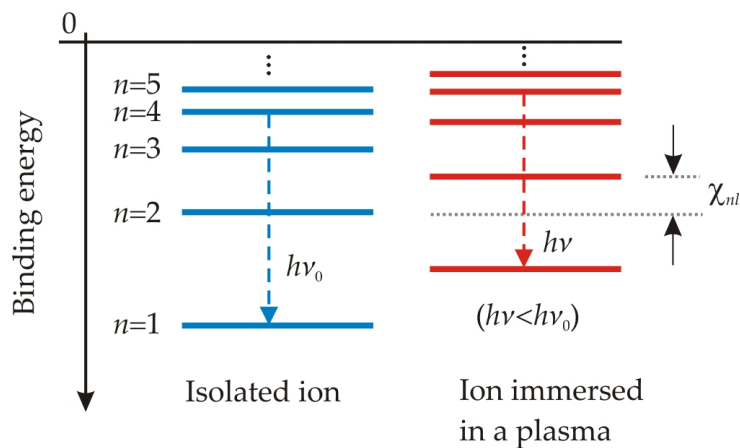


Figure 4.1: Scheme of the energy level shift of an ion immersed in a plasma.

where E_{nl} is the ionic level energy of the radiator immersed in the plasma, and E_{nl}^0 is the energy of the same level when the radiating ion is isolated.

Continuum lowering may be regarded as the main atomic phenomenon unique to hot plasmas (Salzmann, 1998), and it is the phenomenon which causes the line shift. For intermediately coupled plasmas, to estimate the level shift, it is a plausible approximation to use the ion sphere model (see Appendix B) which takes into account only contribution from free electrons to V_{pl} . By considering the situation of a homogenous free electron distribution within the ion sphere volume (which is achieved when the temperature is high enough so that the kinetic energy overcomes the potential energy, see Appendix B), plasma potential can be written as

$$V_{pl}(r) = -\frac{1}{4\pi\epsilon_0} \frac{\zeta e}{R_i} \left[\frac{3}{2} - \frac{1}{2} \left(\frac{r}{R_i} \right)^2 \right] \quad (4.2)$$

with

$$R_i = \left(\frac{3\zeta}{4\pi N_e} \right)^{1/3} \quad (4.3)$$

where R_i is the ion sphere radius, N_e is the electron density, e is the electron charge magnitude, ϵ_0 is the permittivity of the free space, ζ is the number of electrons missing from the ion, and Z is the atomic number of the radiating ion (nuclear charge of the radiator).

Using (4.1) and (4.2), The upward shift, χ_{nl} , of the energy level E_{nl} is

$$\chi_{nl} [eV] = 3.482 \left(\zeta^2 \frac{N_e [\text{cm}^{-3}]}{10^{21}} \right)^{1/3} A_{nl} \quad (4.4)$$

where

$$A_{nl} = 1 - 1.213 \times 10^{-17} \left(N_e [\text{cm}^{-3}] \right)^{2/3} \frac{\zeta^{-2/3}}{Z^2} n^2 [5n^2 + 1 - 3l(l+1)] \quad (4.5)$$

Ionic states for which $\chi_{nl} \geq |E_{nl}^0|$ are no longer bound.* These states are shifted into continuum, and, as a result the corresponding spectral lines merge into continuum (see Section 4.3). An example of the dependence of the $6p$, $7p$, $8p$ and $9p$ state-energies of hydrogen-like aluminum on electron density is shown in Figure 4.2. The calculations are performed by using Eqs.(4.1), (4.4) and condition $\chi_{nl} \geq |E_{nl}^0|$. It is evident that all states move approximately in parallel to each other due to the weak dependence of χ_{nl} on principal quantum number n . The electron density at which a state with principal quantum number n merges into continuum is approximately proportional to $1/n^6$.

* $E_{nl}^0 [eV] = -13.606 Z^2/n^2$ (Mandl, 1992).

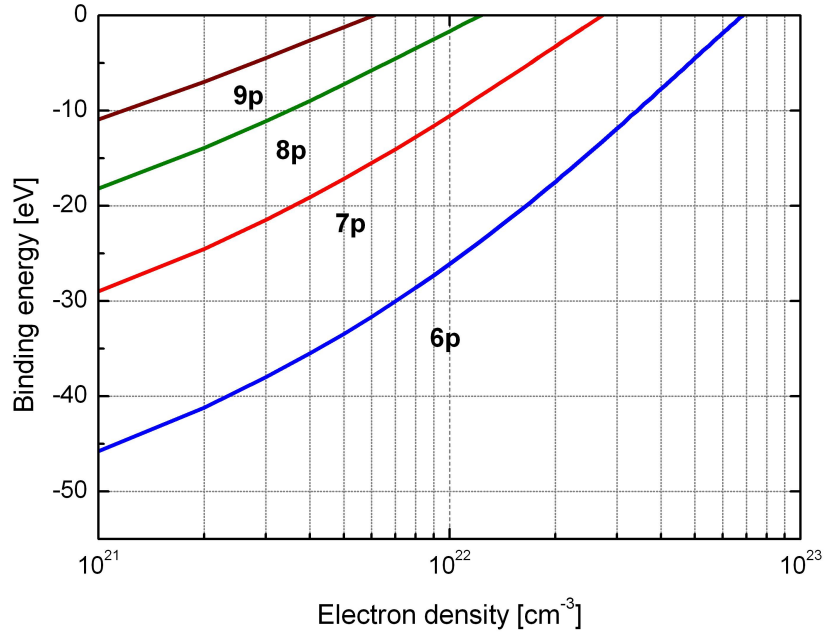


Figure 4.2: The reduction of the binding energy of $6p$, $7p$, $8p$ and $9p$ states as a function of electron density and their merging into continuum.

The shift of a spectral line, $\Delta h\nu$, is the difference between the energy of the photon, $h\nu$, emitted in a transition from an initial state[†], $|i\rangle$, to a final state, $|f\rangle$, when the ion is immersed in a dense plasma, and the transition energy, $h\nu_0$, between the same two states when the ion is isolated,

$$\begin{aligned} \Delta h\nu &= h\nu - h\nu_0 \\ &= [\langle i | H_0 - eV_{pl}(r) | i \rangle - \langle f | H_0 - eV_{pl}(r) | f \rangle] \\ &\quad - [\langle i | H_0 | i \rangle - \langle f | H_0 | f \rangle] \\ &= [\langle i | -eV_{pl}(r) | i \rangle - \langle f | -eV_{pl}(r) | f \rangle] \end{aligned} \quad (4.6)$$

where H_0 is the Hamiltonian of the isolated ion, and $V_{pl}(r)$ is the potential generated by the free electrons. Inserting Eq.(4.2) into (4.6), one obtains for line shift:

$$\begin{aligned} \Delta h\nu &= h\nu - h\nu_0 \\ &= -\frac{1}{12\varepsilon_0} \frac{e^2 a_0^2}{Z^2} N_e \left\{ n^2 [5n^2 + 1 - 3l(l+1)] - n_f^2 [5n_f^2 + 1 - 3l_f(l_f+1)] \right\} \end{aligned} \quad (4.7)$$

where the subscript ' f ' stands for the final state. For Lyman lines ($np \rightarrow 1s$) from

[†]The different quantum states of the radiator are specified in terms of Dirac notation: $|s\rangle \equiv \psi_s$, and $\langle A \rangle = \int \psi_s^* A \psi_s d\tau$, where s stands for the state (n, l, m) and A for an arbitrary operator.

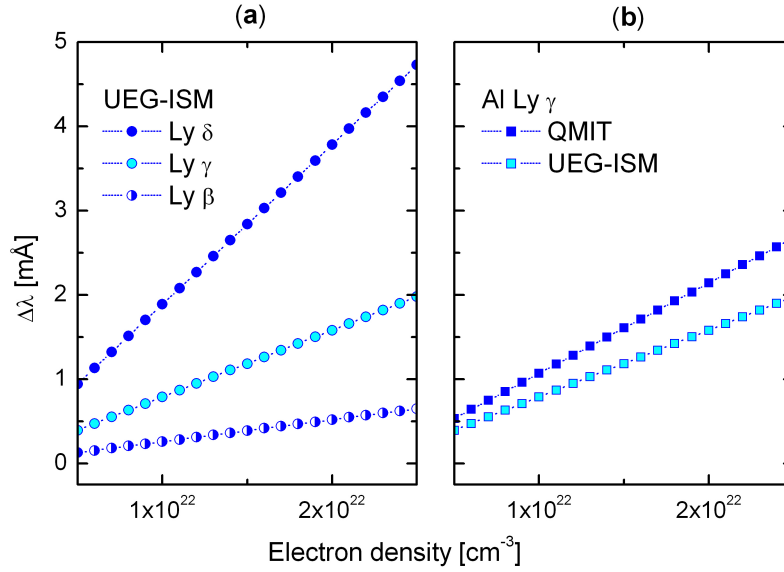


Figure 4.3: (a) Shift of Al Ly β , γ , and δ calculated using UEG-ISM, (b) Shift of Al Ly γ calculated using QMIT and UEG-ISM.

Eq.(4.7) one gets

$$\Delta h\nu (np \rightarrow 1s) [eV] = -\frac{4.223}{Z^2} \left(\frac{N_e [\text{cm}^{-3}]}{10^{24}} \right) [5n^2(n^2 - 1) - 6] \quad (4.8)$$

In the wavelength scale Eq. (4.8) has the form

$$\Delta\lambda (np \rightarrow 1s) [\text{Å}] = \frac{3.406}{Z^2} (\lambda_0 [\text{Å}])^2 \left(\frac{N_e [\text{cm}^{-3}]}{10^{28}} \right) [5n^2(n^2 - 1) - 6] \quad (4.9)$$

where λ_0 is the unperturbed wavelength corresponding to the radiative transition $np \rightarrow 1s$. In Figure 4.3(a), the wavelength shifts of Lyman β , γ and δ of H-like aluminum predicted by Eq. (4.9) are computed.

Numerical estimates of line shifts can be obtained also by using a quantum-mechanical impact theory (QMIT) and a model of a confined atom in a self-consistent field developed by [Nguyen *et al.* \(1986\)](#). Within the framework of the quantum-mechanical impact theory, which includes the monopole, dipole, quadrupole and octopole interactions, the expected shifts, $\Delta\lambda$, of the Lyman lines can be expressed as

$$\Delta\lambda (np \rightarrow 1s) [\text{Å}] = \frac{8.066}{Z^2} (\lambda_0 [\text{Å}])^2 \left(\frac{N_e [\text{cm}^{-3}]}{10^{27}} \right) D(n, l, T_e) \quad (4.10)$$

where n, l are the quantum numbers of the upper transition level, and T_e is the electron temperature. The line shift factors $D(n, l, T_e)$ for Lyman γ are tabulated as a function of temperature in Table 4.1 (overtaken from [Nguyen *et al.*, 1986](#)).

Table 4.1: Line shift factors $D(n = 4, l = 1, T_e)$ for Lyman γ . The data are taken from [Nguyen *et al.* \(1986\)](#).

$T_e[eV]/Z^2$	$D(n = 4, l = 1, T_e)$
1.0	98.83
1.2	92.64
1.4	88.28
1.6	85.00
1.8	82.29
2.0	80.01
2.5	75.52
3.0	72.29
3.5	69.97
4.0	68.15
4.5	66.65
5.0	65.39
5.5	64.30
6.0	63.36
6.5	62.52
7.0	61.76

The density dependence of the Lyman γ line shift of aluminum resulting from quantum mechanical impact theory (QMIT) and uniform-electron-gas-ion-sphere-model (UEG-ISM) is shown in Figure 4.3(b). The Lyman γ line shifts computed by means of UEG-ISM are about 26% smaller than QMIT values, which indicates that the electron density is not uniform in the vicinity of 4p orbits.

4.3 Experimental Results and Discussion

Figure 4.4 shows Al Ly γ line profiles emitted from laser irradiated Al target, sandwiched between CH substrates, at regions which are located at 16, 24, 32 and 40 μm from the irradiated target surface. The spectra are recorded at laser energy of about 3.3 J. The shift from the unperturbed position, $\lambda_0 (= 5.739 \text{ \AA})$, is obvious. As the distance from the target surface decreases, i.e., as the electron density increases, the spectral lines are getting broader and the shift from the unperturbed position increases. The Ly γ shift increases from approximately 0.5 m \AA observed at the distance of about 40 μm from the target surface to more than 2.2 m \AA close to the target surface. This is consistent with predictions of the theoretical models introduced in the previous section, that the line shift is proportional to the electron density. The full widths at half maximum

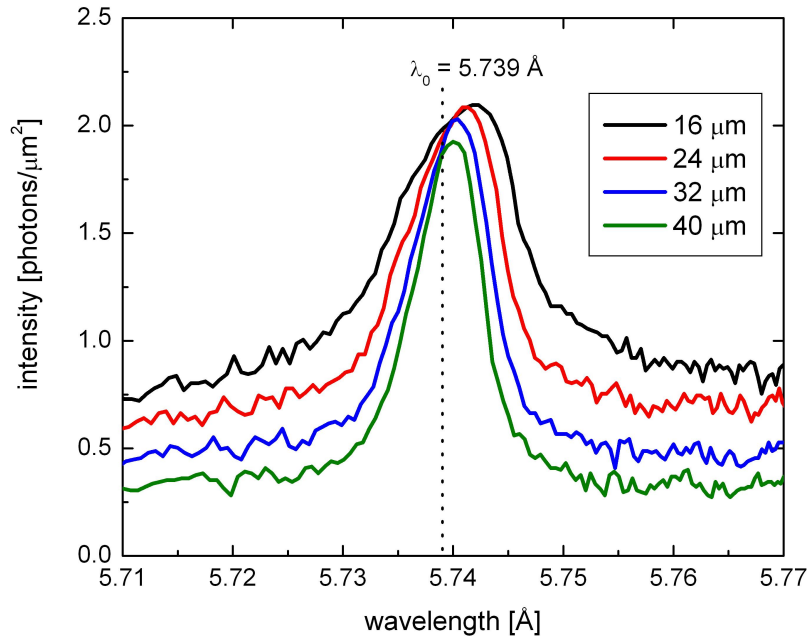


Figure 4.4: Aluminum Ly γ line profiles emitted from the Al irradiated target (20 μm thick), sandwiched between two Mg substrates (each 20 μm thick), measured at the laser energy 3.3 J. The spectral lines are emitted from regions which are located at distances 16, 24, 32 and 40 μm in front of the irradiated target surface.

at 40 and 8 μm from the target surface are 7.2 and 19.4 mÅ, respectively. The observed Ly γ line profiles are well fitted by a Lorentz function of the form (3.4). The error, introduced by the fitting, in determining the line center is about 0.1 mÅ which is comparable with errors introduced by the crystal perfection and readout of the coordinates at the detector. The maximum contribution of the Doppler shift resulting from the ion motion amounts about 0.1 mÅ (at the distance 40 μm from the target surface[‡], see Appendix D). The experimental line shifts are compared with the theoretical values derived from UEG-ISM and QMIT in Figure 4.5. The electron densities which correspond to the emitting regions are derived by means of 1D hydrodynamic code MEDUSA in planar geometry (Christiansen *et al.*, 1974). In the version of the code used here, the hydrodynamic equations are supplemented by a time-dependent, non-local thermodynamic equilibrium average-atom model. This allows the population densities of both the ground and excited states of the ions to be calculated; the latter are proportional to the emission rate of the given transitions. The effective plasma parameters (electron

[‡]This value is obtained assuming that the radiating ions experience thermal motion with velocity $v = \sqrt{3k_B T/M}$, where M is the ion mass (at the distance of 40 μm from the target surface, hydrodynamic simulations (Christiansen *et al.*, 1974) predicts that the electron temperature is about 700 eV). The distance target-crystal was typically about 52 mm.

density and temperature) were averaged over all time-steps by using the emission rate as weighing factor (Renner *et al.*, 1999). It is obvious that the Ly γ shifts predicted by QMIT and UEG-ISM at 16-48 μm from the target surface compare well with the experimentally measured shifts. Near the irradiated target surface ($\leq 24\mu\text{m}$) the predictions of both models are satisfactory (to within about 30%), whereas far from the target surface ($\geq 32\mu\text{m}$) the results begin to converge. The discrepancy at 8 μm is attributed to the underestimation of electron temperature by the hydrodynamic code MEDUSA[§] which results in larger shifts factor $D(n, l, T_e)$ (see Table 4.1) and consequently in larger line shift. At the distances 16-40 μm from the target surface the Ly γ shifts predicted by QMIT show better agreement with the measured shifts than those predicted by UEG-ISM. The discrepancies can be explained in terms of physical assumptions on which the theory of line shift is established (see previous section).

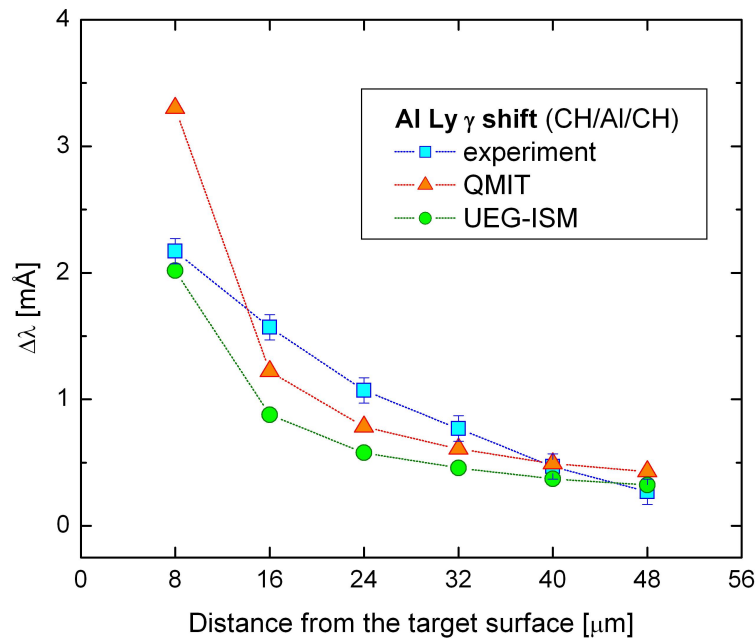


Figure 4.5: Comparison of Al Ly γ shifts with the theoretical values derived by means of QMIT and UEG-ISM. The electron densities which correspond to the emitting regions are derived by means of hydrodynamical code MEDUSA.

In Figure 4.6, the Al Ly γ shifts at 50 μm thick laser irradiated Al targets are shown. In Figure 4.6(a) Ly γ lines are emitted from laser irradiated Al foil (50 μm) sandwiched between two CH substrates (each 25 μm thick), whereas in Figure 4.6(b) Ly γ lines are

[§]At 8 μm from the target surface MEDUSA predicts an electron temperature of about 300 eV.

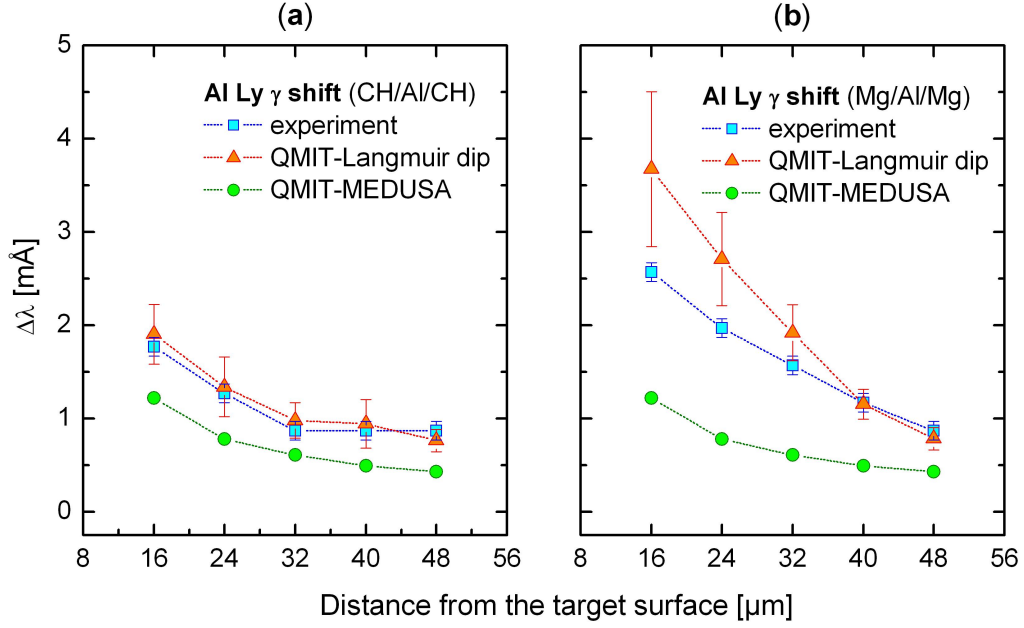


Figure 4.6: Comparison of the experimental Al Ly γ shifts with the theoretical values derived by means of QMIT. (a) Al foil 50 μm thick, sandwiched between two CH substrates (each 25 μm thick), (b) Al foil 50 μm thick, sandwiched between two Mg substrates (each 10 μm thick). The electron densities which correspond to the emitting regions are derived by means of Langmuir dips (see next Chapter) and hydrodynamical code MEDUSA.

emitted from laser irradiated Al foil (50 μm) sandwiched between two Mg substrates (each 10 μm thick). The spectra correspond to the laser energy of about 3.5 and 3.4 J, respectively. The measured line shifts are about 14% of the spectral line widths and are well above the experimental errors. Theoretically predicted shifts are computed by using QMIT (see Eq.(4.10)). The electron densities of the emitting regions are inferred by means of Langmuir dips (see Chapter 5) and by means of the hydrodynamics code MEDUSA. In the case of CH/Al/CH[¶] target, Al Ly γ shifts are up to about 47% smaller than shifts at the Mg/Al/Mg^{||} target. This fact suggests that Mg substrates provide better confinement for Al plasma than CH substrates. The physical explanation of this fact can be related to the diverse lateral plasma confinement. Furthermore, since the plasma expansion velocity is inversely proportional to the square root of the ion mass, one expect that Mg plasmas (which expand slower than CH plasmas) keep the Al plasma at higher densities. The Ly γ shifts at electron densities predicted by the Langmuir dips compare well with experimental values, whereas shifts at electron densities derived by means of the hydrocode MEDUSA are smaller by a factor of 1.8 to 3. The discrepancies are more pronounced for Mg/Al/Mg target because the 1D

[¶]Al foil sandwiched between CH substrates.

^{||}Al foil sandwiched between Mg substrates.

code MEDUSA in a planar geometry does not incorporate the possibility to simulate in detail the hydrodynamics of structured targets (sandwiching of Al targets between Mg or CH substrates) so it does not distinguish between Mg and CH confinements. Other sources of discrepancy can be tentatively attributed to approximations made in the code, those done within the simulation and possible systematic or random errors of the experiment, as well.

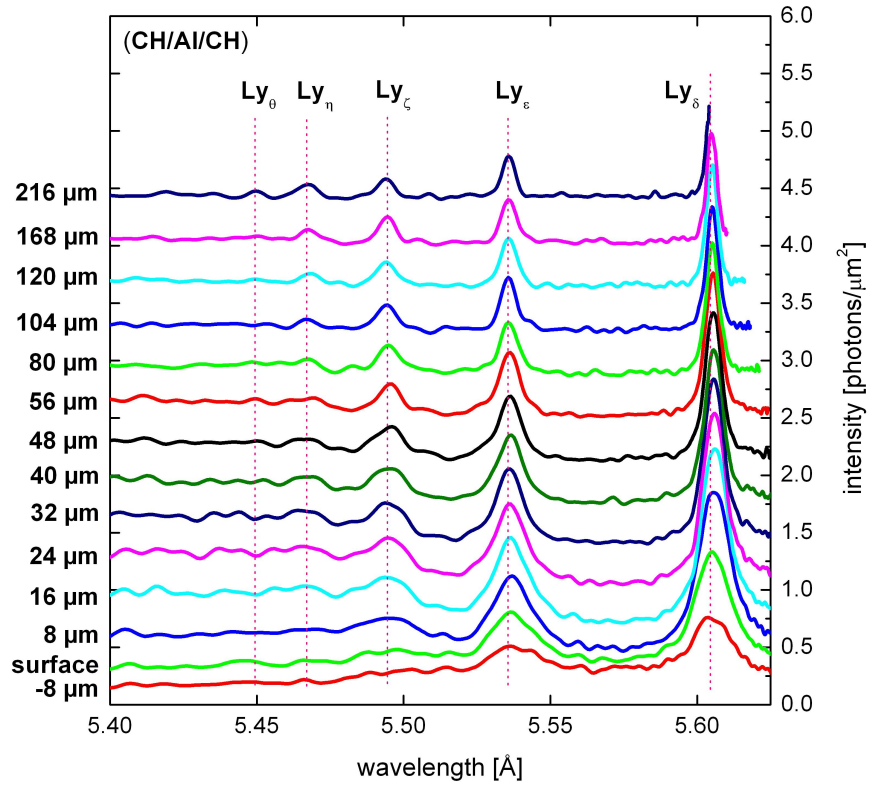


Figure 4.7: Profiles of Al Ly $\delta - \theta$ recorded at distances -8 to 216 μm from the target surface. As the distance to the target surface is decreased, that is electron density increases, some of the higher transitions ($\zeta - \theta$) merge into the continuum because the upper states belonging to those transitions are no longer bound.

Figure 4.7 shows the experimental profiles of Al Ly δ , ϵ , ζ , η and θ emitted at different regions from the target surface. For isolated ions, the wavelengths of Al Ly δ , ϵ , ζ , η and θ are 5.605, 5.534, 5.493, 5.466, and 5.448 Å, respectively (Kelly, 2003). The spectra are emitted from laser irradiated Al foil (20 μm thick) sandwiched between two CH substrates (each 20 μm thick) recorded at laser energy 4.8 J. It is evident that as the distance from the irradiated target surface is decreased, that is electron density increases, some of the higher transitions ($\zeta - \theta$) merge into the continuum. This behavior is due

Table 4.2: Electron densities where Al Ly ζ and η merge into continuum predicted by continuum lowering approach (4.4) and measured Ly δ +FLY (see text).

Spectral line	Ly δ +FLY	Continuum lowering approach
Ly ζ	$1.5 \times 10^{22} \text{ cm}^{-3}$	$2.6 \times 10^{22} \text{ cm}^{-3}$
Ly η	$0.8 \times 10^{22} \text{ cm}^{-3}$	$1.2 \times 10^{22} \text{ cm}^{-3}$

to the fact that upper states of these transitions are no longer bound (see Section 4.1). From Figure 4.7 is obvious that Ly ζ merges into continuum at the target surface, Ly η at about $8 \mu\text{m}$, whereas Ly θ is present only at $216 \mu\text{m}$ from the target surface. The measured widths of Al Ly δ at the target surface and $8 \mu\text{m}$ from the target surface are about 20.8 and $15 \text{ m}\text{\AA}$, respectively. By using the atomic physics code FLY (see Chapter 3), the electron densities at the target surface (where Al Ly ζ merges into continuum) and at $8 \mu\text{m}$ from the target surface (where Al Ly η merges into continuum) are found to be about $1.5 \times 10^{22} \text{ cm}^{-3}$ and $8 \times 10^{21} \text{ cm}^{-3}$, respectively.

Using Eq.(4.4) and condition $\chi_{nl} \geq |E_{nl}^0|$ (see Figure 4.2), the electron densities where Al Ly ζ and Al Ly η merge into continuum are found to be about $2.6 \times 10^{22} \text{ cm}^{-3}$ and $1.2 \times 10^{22} \text{ cm}^{-3}$, see Table 4.2. The discrepancies in electron densities are more pronounced at the target surface. The reason for these disagreements are the high-temperature assumption used to obtain Eq.(4.4) and the negligence of line broadening which is approximately proportional to n^2 , where n is the principal quantum number of the upper transition level. Thus, the observed merging of Al Ly ζ and η into continuum is an interplay of continuum lowering and line broadening.

4.4 Summary and Conclusions

This chapter described the measurement of Ly γ shift and merging of higher Lyman transitions into continuum at laser irradiated Al-sandwich targets. The measured Al Ly γ shifts were compared with shifts predicted by two independent models: UEG-ISM and QMIT. Near the irradiated target surface ($\leq 24 \mu\text{m}$) the predictions of both models are satisfactory (to within about 30%), whereas far from the irradiated target surface ($\geq 32 \mu\text{m}$) the results begin to converge.

Ly ζ - θ show gradual merging into continuum. The electron densities where Ly ζ and η merge into continuum are found to be $1.5 \times 10^{22} \text{ cm}^{-3}$ and $8 \times 10^{21} \text{ cm}^{-3}$,

respectively. Interpretation of line merging within the framework of UEG-ISM and by neglecting line broadening, yields to large errors (33 to 46 %). These disagreements are due to the high-temperature assumption used in UEG-ISM and negligence of line broadening.

Chapter 5

Fine Structure Effects in Al Ly γ

5.1 The Effect of Dynamic Electric Fields in Al Ly γ Line Profile (L-Dips)

In turbulent plasmas the radiating ions are subjected simultaneously to an oscillating high frequency electric field* $E(t) = E_0 \cos(\omega t + \phi)$ originating from electron plasma waves (Langmuir oscillations) and quasistatic electric field, ϵ , generated by ions. The quasistatic electric field, ϵ , represents low-frequency plasma turbulence (ion microfield) and is characterized by some field strength distribution $W(\epsilon)$ (see e.g. Griem, 1974). In the absence of a high-frequency quasi-monochromatic electric field E , one observes a smooth profile of the line corresponding to a smooth change in ϵ from one radiator to another. On the other hand, the high-frequency quasi-monochromatic field E represents Langmuir oscillation at the frequency $\omega \approx \omega_p = [e^2 N_e / (\epsilon_0 m_e)]^{1/2}$. The presence of high-frequency quasi-monochromatic electric fields in a plasma changes substantially the time evolution of a radiator so that the averaged motion of an optical electron may be described in terms of precession and nutation. This leads to the appearance of new components in the emission spectrum: *dips* at definite separation from the line center (Oks *et al.*, 1991; Oks, 1995), see Figure 5.1. These dips, called *L-dips*, result from the resonant coupling of Langmuir oscillations with ion microfields (see below). Langmuir oscillations may cause satellites in the line profiles as well; however, the condition for their appearance in hot and dense plasmas is incompatible with that under which dips appear (Oks, 1995). When only quasimonochromatic electric

*In laboratory plasmas, generally, two classes of electric fields which are distinguished by the width of the frequency band ($\delta\omega/\omega$) are developed: quasi-monochromatic electric field ($\delta\omega/\omega \ll 1$) and broadband electric fields ($\delta\omega/\omega \gtrsim 1$). The quasi-monochromatic electric fields may represent, for example, Langmuir oscillation at a plasma frequency ω_p , laser or microwave radiation at $\omega > \omega_p$, while the ion sound waves can be considered as a broadband electric field (Oks *et al.*, 1991; Oks, 1995).

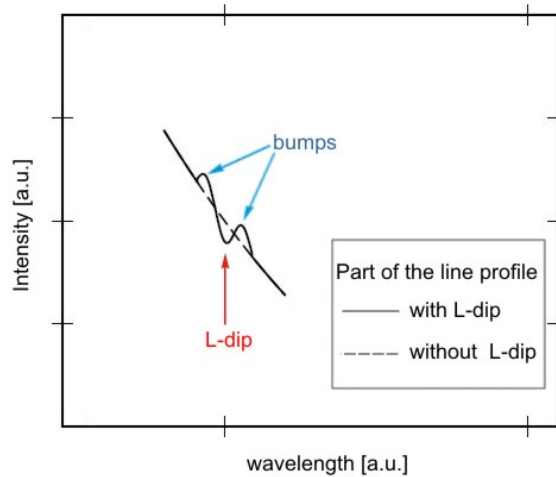


Figure 5.1: A schematic plot of a magnified part of the line profile containing the L-dip, based on the theory of [Oks \(1995\)](#). The dashed line corresponds to a profile without inclusion of quasi-monochromatic electric field. The solid line shows the part of a line profile with inclusion of the quasi-monochromatic field due to Langmuir oscillations; the resulting structure is a dip (whose position is predicted by Eq.(5.2) or (5.5), see below) surrounded by two bumps. Being superimposed with an inclined spectral line profile, each bump-dip-bump structure can be responsible for two local minima of the intensity (rather than just for one local minimum of the intensity at the location given by Eq.(5.2) or (5.5)); in this Figure, the secondary minimum is located at a slightly smaller wavelength compared to the primary minimum (L-dip).

field is present, in the emission spectrum emerge series of satellites at the harmonics of the frequency of the quasimonochromatic electric field, i.e., at $\pm\omega, \pm2\omega, \dots$. In this case the spectral line profile is described in terms of the modified Bessel functions (the so-called Lifshitz profile) ([Oks, 1995](#)).

Since the structure of the emitted spectrum reflects the perturbed level structure caused by simultaneous action of the quasistatic and quasi-monochromatic electric fields, it can be used to diagnose the plasma i.e., it can be used to measure the electron density and, in principle, also the amplitude of the quasi-monochromatic electric field. These information are contained in the position of the L-dip relative to the line center, and in L-dip width. Namely, the positions of L-dips from the line center depend on a plasma density, and their widths depend on the amplitude of the electric field. Determination of electron density by means of L-dips is particularly important for spectral lines which arise from even principal quantum number states $n = 2, 4, 6, \dots$ (i.e. Lyman α, γ, ϵ , etc.), whose line-widths cannot guarantee unambiguous determination of densities ([Lee, 1985](#)). Thus, development of reliable procedure for identification of L-dips in the profiles of these spectral lines would provide another independent method for determining the plasma density and/or for proving the consistency of the

data obtained by other means such as e.g. line shifts. Another important diagnostic aspect is related with laser-driven inertial confinement fusion (ICF) (see Appendix A). The success of ICF depends partly on mitigating the undesirable effect caused by fast electrons which can preheat the core of an imploding sphere prior to the arrival of the compression shock front (Bell, 1993). Fast electrons are generated from high electric fields developed in the plasma (Rubenchik and Zakharov, 1991; Bell, 1993); thus, an estimate of the electric field amplitude would give information about their energy.

L-dips were first discovered experimentally in profiles of hydrogen spectral lines in 1977 (Zhuzhunashvili and Oks, 1977) and explained theoretically by Oks and Rantsev-Kartinov (1980), and, Gavrilenko and Oks (1981, 1987). The theory of L-dips, including quadruple interactions between radiating ions and perturbers, and extended for H-like ions, is presented by Oks *et al.* (1991).

In various plasma experiments (Finken *et al.*, 1980; Oks *et al.*, 1991; Oks, 1995, and references therein), at different plasma sources (linear-, θ - and z - pinches), L-dips were observed and successfully used as a diagnostic tool. In particular, Oks *et al.* (1991) identified L-dips in L_{α} line profiles of Hydrogen at gas-linear pinch plasma; electron densities derived by means of L-dips were consistent with those obtained by means of coherent Thomson scattering. Moreover, experimental results of Yaakobi *et al.* (1977), reanalyzed by Oks (1995), indicate that the local structures observed in the the Ly γ line of Ne X might be interpreted as L-dips. However, the spectral and spatial resolution of that experiment was relatively low. A more conclusive experimental confirmation of L-dip occurrence in spectral lines of laser-produced plasmas requires instrumentation with improved spectral and spatial resolution, and at the same time it requires a design of new experimental configurations.

New experiments aimed to identify and observe L-dips in Al-sandwich targets by using high-resolution, high-dispersion vertical geometry Johann spectrometer, are presented in Section 5.3, Renner *et al.* (2005) and Krasniqi *et al.* (2005a). Due to specially designed targets and application of VJS (see Chapter 2, Section 2.2), in the profiles of the Al Ly γ line, the structures that can be identified as L-dips are observed. Furthermore, L-dips are used to derive electron densities of the emitting regions. The data are compared with those derived by means of line shifts and hydrodynamic simulations. Below, some brief excerpts of the theory published in (Oks *et al.*, 1991; Oks, 1995),

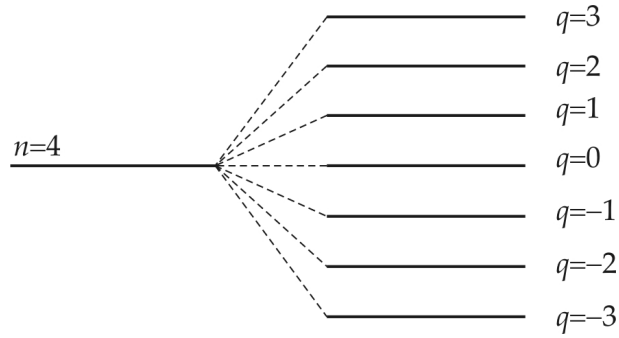


Figure 5.2: Splitting of the energy level with principal quantum number $n = 4$. Aside from the dependence on n , the Stark splitting is a function of the electric quantum number q (see Appendix E).

which are necessary to interpret L-dips in Section 5.3, are outlined.

L-Dips in Spectral Lines Emitted from H-Like Ions

In spectral lines, L-dips arise when the quasistatic Stark splitting of the ionic levels involved in radiative transition satisfies condition of the resonance with the quasi-monochromatic electric field due to Langmuir oscillations. This resonance is reached when the separation of two neighboring Stark sublevels $\Delta\omega$ is equal to a multiple of a plasma frequency[†] ω_p , i.e.,

$$\Delta\omega = k \omega_p \quad (5.1)$$

where $k = 1, 2, 3, \dots$ is the number of quanta involved in the resonance.

In the dipole approximation, under the action of the electric field ϵ , a level of a radiator with principal quantum number n is split into $(2n - 1)$ equidistant Stark sublevels, Figure 5.2. In high density plasmas the spatial non-uniformity becomes essential. This means that a dipole approximation is no longer sufficient for describing the interaction of a radiator with perturbing ions and higher multi-poles (at least the quadrupole term) have to be taken into account. When the quadrupole interaction of the radiator with the perturbing ions is taken into account, a separation $\Delta\omega_q^+$ between Stark sublevels $(q, q + 1)$ differs from a separation $\Delta\omega_q^-$ between Stark sublevels $(q, q - 1)$ (for more information on electric quantum number q , see Appendix E).

The resonance of the oscillating field with Stark sublevels $(q, q + 1)$, i.e. $\Delta\omega_q^+ = k\omega_p$, leads to the appearance of L-dips in the profile of a spectral line corresponding to a

[†]Depending on electron density, the magnitude of plasma quasistatic field can reach such values that the energy separation between Stark sublevels can be of the same order of magnitude as the plasma frequency and the resonance effect will occur.

radiative transition $n \rightarrow n_0$, whose position $\Delta\lambda_{q+}$ from the line center is[†]

$$\Delta\lambda_{q+} \approx -\frac{\lambda_0^2}{2\pi c} \left[\frac{(nq - n_0q_0)}{n} k\omega_p + U_q^+ \sqrt{\frac{2}{27n^3 Z_r Z_p} \frac{(k\omega_p)^3}{\omega_a}} \right] \quad (5.2)$$

where

$$U_q^+ = n^2(n^2 - 6q^2 - 1) + 6n(2q + 1)(nq - n_0q_0) - n_0^2(n_0^2 - 6q_0^2 - 1) \quad (5.3)$$

$$\omega_a = \frac{1}{(4\pi\epsilon_0)^2} \frac{me^4}{\hbar^3} \quad (5.4)$$

where the subscript '0' stands for the final state (lower state).

Some other group of radiators in the plasma experience the action of the field ϵ just corresponding to the condition of the resonance of Stark sublevels $(q, q - 1)$, i.e., $\Delta\omega_{q-} = k\omega_p$; this leads to the appearance of an additional set of L-dips in the line profile corresponding to a radiative transition $n \rightarrow n_0$, whose position $\Delta\lambda_{q-}$ from the line center is

$$\Delta\lambda_{q-} \approx -\frac{\lambda_0^2}{2\pi c} \left[\frac{(nq - n_0q_0)}{n} k\omega_p + U_q^- \sqrt{\frac{2}{27n^3 Z_r Z_p} \frac{(k\omega_p)^3}{\omega_a}} \right] \quad (5.5)$$

$$U_q^- = n^2(n^2 - 6q^2 - 1) + 6n(2q - 1)(nq - n_0q_0) - n_0^2(n_0^2 - 6q_0^2 - 1) \quad (5.6)$$

For $k = 1$ one has *first order dips*. Dips of higher order, $k > 1$, are observed if $E_0/\epsilon > 10^{-1}$ (Oks *et al.*, 1991).

For Lyman lines the final level has the principal quantum number $n_0 = 1$, i.e., $n_{1,0} = 0$, $n_{2,0} = 0$ ($q_0 = 0$), and $m_0 = 0$ (relation between the principal quantum number, n , and parabolic quantum numbers n_1 and n_2 is outlined in Appendix E). In this case, dips which arise due to the first order resonance ($k = 1$) of the oscillating field of a frequency $\omega_p(N_e)$ with Stark sublevels $(q, q + 1)$ and $(q, q - 1)$, respectively, are located from the line center at distances

$$\Delta\lambda_{q\pm} \approx -\frac{\lambda_0^2}{2\pi c} \left\{ q\omega_p + \sqrt{\frac{2}{27n^3 Z_r Z_p} \frac{\omega_p^3}{\omega_a}} [n^2(n^2 - 6q^2 - 1) + 6n^2q(2q \pm 1)] \right\} \quad (5.7)$$

where the sign '+' stands for L-dips (L^+ dips) which result from the resonance of the oscillating field of a frequency $\omega_p(N_e)$ with Stark sublevels $(q, q + 1)$, and '-' stands for L-dips (L^- dips) which result from the resonance of the oscillating field with Stark

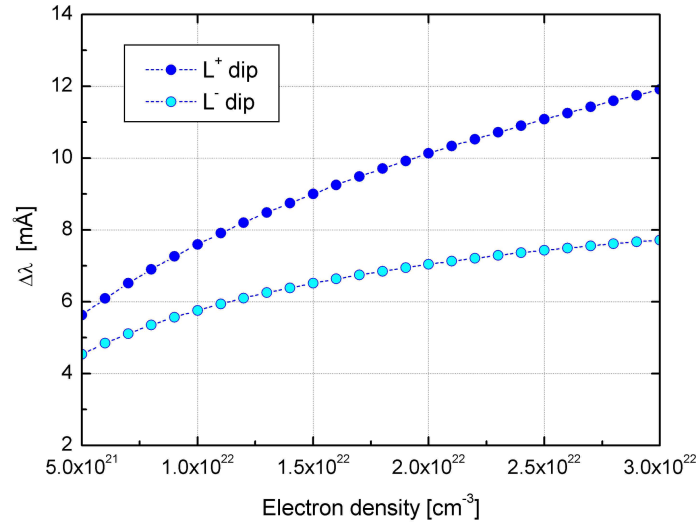


Figure 5.3: Dependence of the Langmuir dips in Al Ly γ on electron density. L^- dip results from the resonance of the oscillating field of a frequency $\omega(N_e)$ with Stark sublevels $(q, q - 1) = (-1, -2)$ whereas the dip L^+ results from the resonance with Stark sublevels $(q, q + 1) = (-1, 0)$.

sublevels $(q, q - 1)$; λ_0 is the unperturbed wavelength. The dependence of the position of L-dips from the line center, computed by means of Eqs.(5.7), is shown in Figure 5.3.

Assuming that the first order L-dips are sufficiently resolved, it might be possible to determine experimentally a half-width, $\Delta\lambda_{1/2}^{dip}$, of a dip (or an equal value of a distance between the dip minimum and the nearest bump). This should enable estimation of the amplitude E_0 of the quasi-monochromatic electric field according to the formula (Oks *et al.*, 1991):

$$E_0 \approx \left(\frac{2}{3}\right)^{1/2} \frac{2 m e c}{\epsilon_0 \lambda_0^2 n^2 \hbar} \Delta\lambda_{1/2}^{dip} \quad (5.8)$$

where n is the principal quantum number of the upper transition level. Knowing E_0 one can calculate the necessary condition, $E_0/\epsilon > 10^{-1}$, for a reliable identification of the high order dips ($k > 1$), e.g., for $\Delta\lambda_{1/2}^{dip} \approx 0.5 \text{ m}\text{\AA}$ (see Section 5.3), Eq.(5.8) yields $E_0 \approx 7 \text{ MV/cm}$. Taking for the field strength ϵ the mean ion microfield $\langle\epsilon\rangle \approx 8.8eN_e^{2/3}/(4\pi\epsilon_0)$, the ratio $E_0/\langle\epsilon\rangle$ which can give an estimate about the possibility of observation of high order L-dips can be calculated; for $N_e = 2 \times 10^{22} \text{ cm}^{-3}$ one obtains $\langle\epsilon\rangle \approx 1 \text{ GV/cm}$, thus $E_0/\langle\epsilon\rangle \approx 0.01$ which means that at this density one can observe only first order dips ($k = 1$).

[‡]The profile of a spectral line corresponding radiative transition $n \rightarrow n_0$ is given by $I_{n \rightarrow n_0}(\lambda) = \sum_j I_{n \rightarrow n_0, j}(\lambda)$, where $I_{n \rightarrow n_0, j}(\lambda)$ is the profile of a Stark component corresponding to a electric quantum number q_j .

The dependence of L-dips on plasma density provides a vehicle for derivation of the electron densities of the emitting regions. This is done by measuring the position of L-dips from the line center and by using Eqs.(5.2) and (5.5), or for Lyman lines, Eqs.(5.7) (see Section 5.3).

5.2 Exhibition of the Charge Exchange Phenomena in Al Ly γ Line Profile (X-Dips)

Hot and dense plasmas with electron density of the order of 10^{22} cm $^{-3}$ and electron temperature in excess of 100 eV, characterized by a moderate coupling (plasma coupling constant Γ to about 1), are favorable environments for the formation of transient radiator systems consisting of two ionic centers (i.e., the electron is shared by two ionic centers), so called *quasi-molecules* (Gauthier *et al.*, 1998). Formation of such dicenter systems can lead to the appearance of fine structures in spectral lines. When the dicenter system is hetero-nuclear (i.e., nuclear charges of the ions involved in a quasi-molecule are different), the fine structures in a spectral line are manifested as dips, called *X-dips*, and are related to charge exchange (Oks and Leboucher-Dalimier, 2000a; Leboucher-Dalimier *et al.*, 2001). Fine structures originating from dicenter systems can be manifested as satellites (called quasimolecular satellites) as well, however, in distinction to X-dips, quasimolecular satellites are unrelated to charge exchange, and are observed in plasmas at higher densities (up to three order of magnitudes greater than those where X-dips can be observed) (Leboucher-Dalimier *et al.*, 2001, 2002).

X-dips result from *avoided crossing* of radiator and perturber terms.[§] An avoided crossing occurs when two wells, corresponding to separated ionic centers of charges Z_r (nuclear charge of radiating ion) and Z_p (nuclear charge of perturbing ion), with $Z_r \neq Z_p$, have states ψ_r and ψ_p characterized by the same energies $E_r = E_p$, by the same magnetic quantum numbers $m_r = m_p$, and by the same radial elliptical quantum $k_r = k_p$ (Oks and Leboucher-Dalimier, 2000a,b; Oks, 2000).

The experimental studies of X-dips would serve for producing fundamental data on charge exchange cross section between multi-charged ions (Leboucher-Dalimier *et*

[§]Here, a term is used to denote a state of an ion (atom) characterized with principal quantum number n , electric quantum number q , magnetic quantum number m , and spin-magnetic quantum number m_s (in spherical coordinates a term is characterized with n , l , m and m_s , where l is the angular momentum quantum number).

al., 2001; Oks and Leboucher-Dalimier, 2000a,b). The study of charge exchange is important, not only to obtain a basic mechanisms of rearrangement collisions, but also because charge exchange is a process which can be used for measuring the concentration of impurity ions in tokamak plasmas and in pumping atomic levels which exhibit laser action (Bransden and McDowell, 1992).

X-dips are relatively new phenomena. They were first observed in the profile of the neutral hydrogen line H_α emitted from a helium plasma of the gas-liner pinch (Böddeker *et al.*, 1995). A successful observation of X-dips in spectral lines of multi-charged ions in laser produced plasmas is reported by Leboucher-Dalimier *et al.* (2001). New experiments aimed to identify and observe X-dips in Al_4C_3 -sandwich target by using high-resolution, high-dispersion vertical geometry Johann spectrometer, are presented in the next Section and by Renner *et al.* (2005). Below, some brief excerpts of the analytic theory given by Oks and Leboucher-Dalimier (2000a) are outlined.

X-dips in Spectral Lines Emitted from Hydrogen-Like Ions

To explain X-dips in spectral lines emitted from H-like ions, electron terms in the field of two stationary Coulomb centers of charges Z_r and Z_p (hetero-nuclear dicenter system) separated by a distance R , are considered. Z_r and Z_p denote the nuclear charges of a radiating ion and perturbing ion, respectively. The upper state of the radiating ion involved in the radiative transition (term a) has the principal quantum number n and electric quantum number q , whereas the lower state of the radiating ion (term a_0) involved in the radiative transition is characterized with quantum numbers n_0 and q_0 .

At some distance R_c , the radiator term a experiences avoided crossing with perturbing ion term a_p (characterized with principal quantum number n_p and electrical quantum number q_p) i.e. $E_a = E_{a_p}$ and $m = m_p$. In the case of large internuclear distances

$$R \gg (4\pi\epsilon_0) \frac{\hbar^2 n^2}{me^2 Z_r} \quad (5.9)$$

one can treat separately the terms a and a_p and use $1/R$ expansion of the energies E_a , E_{a_p} and E_{a_0} . The expansion of energies up to the $1/R^2$ terms has the form

$$E_a \approx -\frac{1}{(4\pi\epsilon_0)^2} \frac{me^4 Z_r^2}{2\hbar^2 n^2} - \frac{1}{4\pi\epsilon_0} \frac{Z_p e^2}{R} + \frac{3\hbar^2 nq Z_p}{2mR^2 Z_r} \quad (5.10)$$

$$E_{a_p} \approx -\frac{1}{(4\pi\epsilon_0)^2} \frac{me^4 Z_p^2}{2\hbar^2 n_p^2} - \frac{1}{4\pi\epsilon_0} \frac{Z_r e^2}{R} + \frac{3\hbar^2 n_p q_p Z_r}{2mR^2 Z_p} \quad (5.11)$$

$$E_{a_0} \approx -\frac{1}{(4\pi\epsilon_0)^2} \frac{me^4 Z_r^2}{2\hbar^2 n_0^2} - \frac{1}{4\pi\epsilon_0} \frac{Z_p e^2}{R} + \frac{3\hbar^2 n_0 q_0 Z_p}{2mR^2 Z_r} \quad (5.12)$$

The position of the crossing of the terms R_c , i.e., the internuclear distance between the radiating and perturbing ions where the crossing of the terms takes place, is found by equating $E_a = E_{a_p}$,

$$R_{c(\pm)} = \left(4\pi\epsilon_0 \frac{\hbar^2}{me^2}\right) \frac{(Z_p - Z_r) \pm \left[(Z_r - Z_p)^2 - 4\left(\frac{Z_p^2}{2n_p^2} - \frac{Z_r^2}{2n^2}\right) \left(\frac{3Z_p n q}{2Z_r} - \frac{3Z_r n_p q_p}{2Z_p}\right) \right]^{1/2}}{\left(\frac{Z_p^2}{n_p^2} - \frac{Z_r^2}{n^2}\right)} \quad (5.13)$$

From Eq.(5.13) it is obvious that there are two solution for R_c , but only one of them has a physical meaning. Using the fact that avoided crossing always results in a dip (in the profile of the corresponding Stark component) at a relatively large distances (Oks and Leboucher-Dalimier, 2000a)

$$R \gg \max \left[(4\pi\epsilon_0) \frac{\hbar^2 n^2}{me^2 Z_r}, (4\pi\epsilon_0) \frac{\hbar^2 n_p^2}{me^2 Z_p} \right] \quad (5.14)$$

one can choose the value R_c from Eq.(5.13) which corresponds to the crossing distance, i.e., the value R_c which has a physical meaning should be consistent with condition (5.14). E.g., crossing of a radiator term ($n = 4, q = -3, Z_r = 13$) with the perturber term ($n_p = 2, q_p = -1, Z_p = 6$) occurs at $R_c \approx 4.6 \text{ \AA}$ (Figure 5.4); this is the solution of Eq.(5.13) which has a physical meaning because this distance is about 7 times greater than the largest value predicted by inequality (5.14); the other value does not fulfill numerically this inequality. This crossing of the terms translates into a X-dip in the line profile of Al Ly γ which is located about 8.6 m\AA from the line center.

For the majority of radiating ions, the perturbing ions with charge Z_p are separated by a distance R that is not in a close proximity to R_c . In this case the spectral line formation and broadening can be described in terms of Stark splitting of the energy levels of a radiator. The situation differs drastically for a minority of radiators for which the distance R from the perturber is in a close proximity to R_c . Because of the crossing of the terms, charge exchange provides *an additional channel for decay* of the

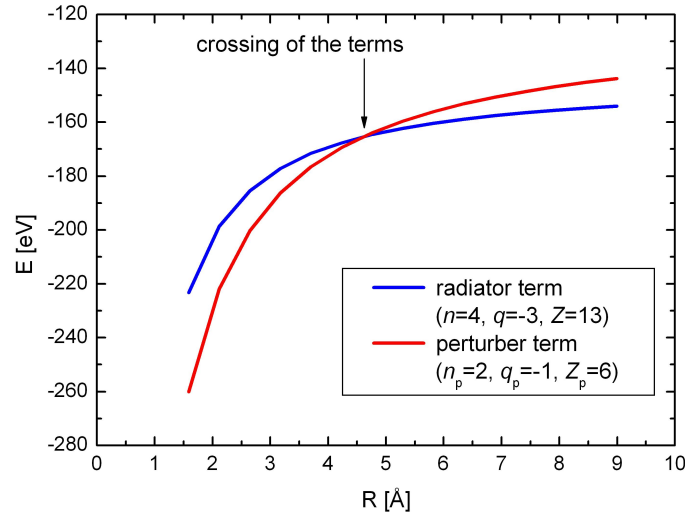


Figure 5.4: Crossing of a radiator term ($n = 4, q = -3, Z_r = 13$) with the perturber term ($n_p = 2, q_p = -1, Z_p = 6$). Energies of the radiator and perturber terms are computed using Eqs. (5.10) and (5.11). Crossing of the terms occurs at $R_c \approx 4.6 \text{ \AA}$. This crossing of the terms translates into a X-dip in the spectral line of Al Ly γ which is located about 8.6 m\AA from the line center.

excited state of the radiating ion. Therefore, the lifetime of the excited state is shorted and the collisional width suddenly increases. Finally, at the wavelength $\Delta\lambda(R_c)$ from the line center the intensity of the resultant line profile becomes smaller than it would be if the avoided crossing was absent. At two close adjacent wavelengths $\Delta\lambda(R_c) \pm \delta$ the intensity is increased. The resulting structure will appear on the line profile as a dip surrounded by two bumps and it has the same structure as that shown in Figure 5.1.

The position of an X-dip relative to the line center λ_0 is given by

$$\Delta\lambda^{dip} = \lambda^{dip} - \lambda_0 \quad (5.15)$$

where λ^{dip} , calculated using Eqs.(5.10) and (5.12), is

$$\lambda^{dip} = 2\pi \hbar c \left[\frac{1}{(4\pi\epsilon_0)^2} \frac{me^4 Z_r^2}{2 \hbar^2} \left(\frac{1}{n_0^2} - \frac{1}{n^2} \right) + \frac{3 \hbar^2}{2mR_c^2} \frac{Z_p}{Z_r} (nq - n_0q_0) \right]^{-1} \quad (5.16)$$

To measure the 'contrast' of the X-dip, a quantity called *visibility of the X-dip* is introduced and defined as (Oks and Leboucher-Dalimier, 2000a)

$$V = \frac{I_0(\Delta\lambda^{dip}) - I_x(\Delta\lambda^{dip})}{I_0(\Delta\lambda^{dip})} \approx \left| \left[1 - (4\pi\epsilon_0) \frac{3\hbar^2 Z_p}{me^2 R_c Z_r} \left| \frac{nq - n_0q_0}{Z_r - Z_p} \right| \right] / [n_0(2n - 1)] \right| \quad (5.17)$$

where $I_0(\Delta\lambda^{dip})$ is the intensity of the spectral line profile without X-dip, and $I_x(\Delta\lambda^{dip})$ is the intensity of the spectral line profile which contain an X-dip.

The avoided crossing of radiator and perturber terms which result in X-dips obeys a *selection rule* which can be stated as follows (Oks and Leboucher-Dalimier, 2000a): For each perturber term (n_p, q_p, Z_p, m_p) , the charge exchange, manifested as an avoided crossing, is possible with no more than one radiator term (n, q, Z_r, m) with the following parabolic quantum numbers:

$$n_1 = n_{1,p} \quad (5.18a)$$

$$m = m_p \quad (5.18b)$$

$$n_2 = n - n_{1,p} - |m_p| - 1 \quad (5.18c)$$

In Al Ly γ ($Z_r = 13$) perturbed by fully striped C ions ($Z_p = 6$), in the range of electron densities $10^{20} - 10^{22} \text{ cm}^{-3}$ and based on the selection rules (5.18), one can observe three X-dips. These X-dips are denoted by X_1 , X_2 and X_3 and are characterized as follows:

- Dip X_1 results from avoided crossing of the radiator term ($n = 4, q = -1, Z_r = 13$) with the perturber term ($n_p = 2, q_p = 1, Z_p = 6$). This avoided crossing occurs in the vicinity of $R_c \approx 3.9 \text{ \AA}$ at the energy $E_4 \approx -167.3 \text{ eV}$ (at $R_c \approx 3.9 \text{ \AA}$ the energy of the ground level of H-like Al is $E_1 \approx -2321.6 \text{ eV}$). The absolute position of the crossing should be at 5.755 \AA . Since for the Al Ly γ the two dicenter-model-code IDEFIX (Leboucher-Dalimier *et al.*, 2002) yields $\lambda_0 = 5.751 \text{ \AA}$, the position of the dip X_1 relative to the line center is $\Delta\lambda_{X_1} \approx 4.3 \text{ m\AA}$. The visibility of the dip X_1 is $V_{X_1} \approx 12.7\%$.
- Dip X_2 results from avoided crossing of the radiator term ($n = 4, q = -2, Z_r = 13$) with the perturber term ($n_p = 2, q_p = 0, Z_p = 6$). This avoided crossing occurs in the vicinity of $R_c \approx 4.3 \text{ \AA}$ at the energy $E_4 \approx -166.2 \text{ eV}$ (at R_c the energy of the ground level of H-like Al is $E_1 \approx -2319.6 \text{ eV}$). Position of the dip X_2 relative to the line center is $\Delta\lambda_{X_2} \approx 6.7 \text{ m\AA}$. The visibility of the dip X_2 is $V_{X_2} \approx 11.5\%$.
- Dip X_3 results from avoided crossing of the radiator term ($n = 4, q = -3, Z_r = 13$) with the perturber term ($n_p = 2, q_p = -1, Z_p = 6$). This avoided crossing

occurs in the vicinity of $R_c \approx 4.6 \text{ \AA}$ at the energy $E_4 \approx -165.5 \text{ eV}$ (at R_c the energy of the ground level of H-like Al is $E_1 \approx -2318.1 \text{ eV}$). Position of the dip X_3 relative to the line center is $\Delta\lambda_{X_3} \approx 8.6 \text{ m\AA}$, and the visibility $V_{X_3} \approx 10.4\%$.

In contrast to carbon perturbers, X-dips caused from crossing of Al-radiator terms with Mg (Magnesium)-perturber terms cannot be observed in Al Ly γ . There are two reasons for this conclusion: (i) for most of possibilities allowed by selection rules (5.18) the condition (5.14), which ensures the presence of the dip, is not fulfilled, and (ii) if the condition (5.14) is fulfilled, X-dips are located outside the Ly γ line profile.

There are upper and lower limits that determine the range of electron densities where the X-dips can be observed (Oks and Leboucher-Dalimier, 2000a,b). Both the lower and the upper limits come from the requirement that the crossing distance R_c should not differ too much from the most probable internuclear distance. If the electron density is too low, the X-dip is located in the far wing of the line where the signal to noise ratio is not reasonable, or is not present in the line at all. If the electron density is too high then Stark broadening will smooth out the dip. The range of electron densities where these X-dips could be observed in Al Ly γ is $10^{20} - 10^{22} \text{ cm}^{-3}$ (Oks and Leboucher-Dalimier, 2000a).

5.3 Experimental Results and Discussions

In this section, the results of the experiments aimed to observe the L- and X-dips in Ly γ line emitted from irradiated Al- and Al₄C₃-sandwich targets, are presented and discussed.

Figures 5.5 and 5.6 show experimental profiles of Al Ly γ line emitted from Al targets sandwiched between CH substrates (CH/Al/CH target) and sandwiched between Mg substrates (Mg/Al/Mg target), irradiated at laser energies 3.5 and 3.4 J, respectively. The spectral lines were observed at different distances from the target surface, that is, they correspond to plasma regions with different electron densities. The profiles display tiny features which move systematically with the decreasing distance from the target surface, i.e., with the increasing electron density. These features are labelled as L⁻ and L⁺. They represent the L⁻ dip, which occurs when the separation between Stark sublevels $q = -1$ and $q = -2$ is equal to the plasma frequency $\omega_p(N_e)$, and the L⁺ dip which occurs when the plasma frequency is equal to the sep-

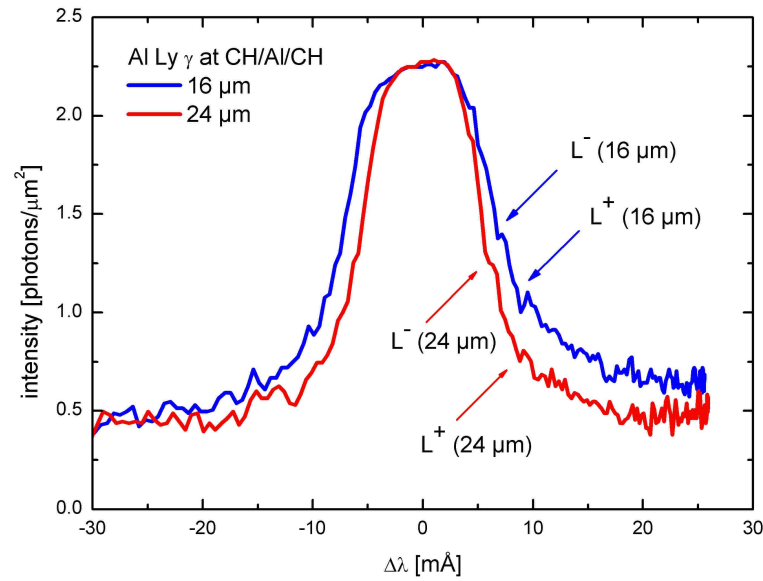


Figure 5.5: Experimental profiles of the Al Ly γ line measured at the laser irradiated Al target, 50 μm thick, sandwiched between two CH substrates, each 25 μm thick (laser energy: 3.5 J). The spectra are emitted at 16 and 24 μm from the target surface. Features labelled as L^- and L^+ represent L-dips.

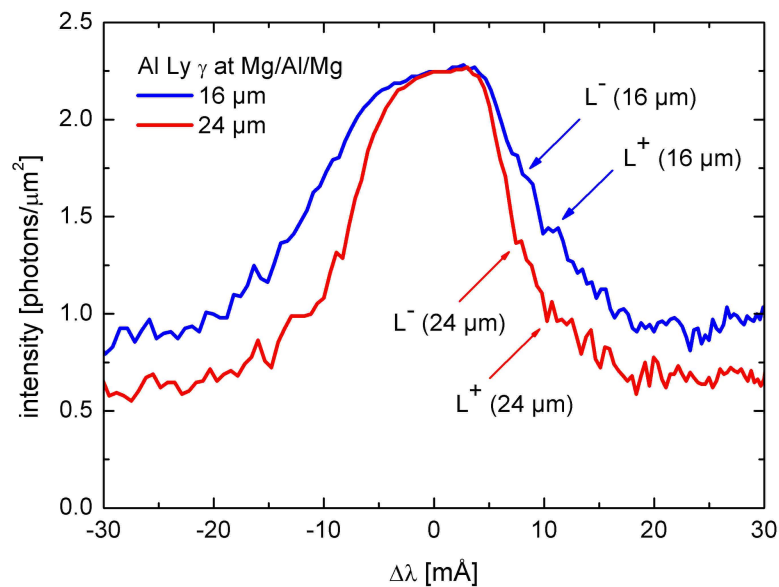


Figure 5.6: Experimental profiles of the Al Ly γ line measured at the laser irradiated Al target, 50 μm thick, sandwiched between two Mg substrates, each 10 μm thick (laser energy: 3.4 J). The spectra are emitted at 16 and 24 μm from the target surface. Features labelled as L^- and L^+ represent L-dips.

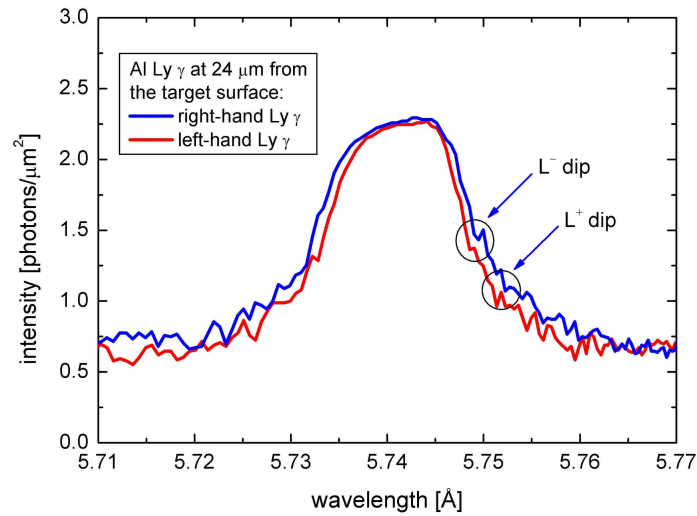


Figure 5.7: The left- and right-hand sides of Al Ly γ -spectrum. L-dips are marked with dashed circles. The observed discrepancies may be ascribed to a slight misalignment of the densitometered film resulting in a spatial misfit of a $\pm 4 \mu\text{m}$ between left- and right-hand records, and to random defects on the detector.

aration between Stark sublevels $q = -1$ and $q = 0$, see Section 5.1. The confidence in a correct identification of the L-dips is mainly based on the outstanding property of the VJS (see Chapter 2, Section 2.2) to produce simultaneously two mirror-symmetric spectra; in other words, any real feature observed in one side of the spectra should also be observed in the symmetric part. The fine structures observed in both mirror-symmetric spectra are nearly identical; the left- and right-hand spectra of Al Ly γ are compared in Figure 5.7. Our analysis of several Al Ly γ line profiles emitted at different regions from the target surface identifies these features as L-dips. This conclusion is based on the facts that for all laser shots providing comparable irradiation of the targets, the spectra demonstrate similar qualitative features, they are reproducible in both mirror-spectra and their evolution with electron density follows theoretical expectations predicted by Eqs.(5.7). In contrast, the analysis of the structure present in the blue side of the spectral lines indicates that the relevant features cannot be attributed to the plasma oscillations. Additionally, the modulation of the intensity by the most pronounced bump-dip-bump structures is about 10%, while the standard deviation of the intensity measurement at the locations of these dips is between 3 and 4%.

The distance of the L^- and L^+ dips from line center decreases with the decreasing electron density but also the intensity of the spectral line and the FWHM decrease as well; consequently the L dips begin to merge into noise. The lower and upper limits

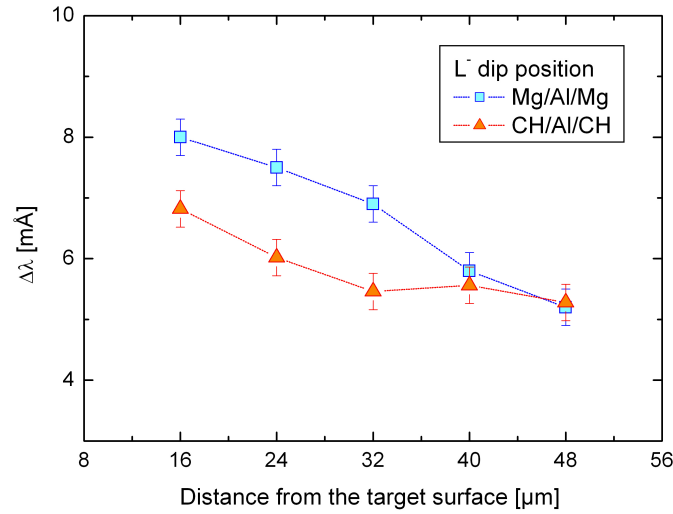


Figure 5.8: The measured space-dependent positions of the L^- dip from the line center.

that determine the range of electron densities where the L-dips could be observed in our measurements are about $5 \times 10^{21} \text{ cm}^{-3}$ and $3.5 \times 10^{22} \text{ cm}^{-3}$, respectively. L^- dips are located closer to the line center and in a parts of a line profile with a favorable signal to noise ratio in contrast to L^+ dips which are located further from the line center and closer to the noise. For this reason, hereafter the attention is focused into L^- dips. At the irradiated CH/Al/CH target, position of the L^- dip from the line center decreases from approximately 7 mÅ observed at the distance of about 16 μm from the target surface to 5 mÅ at 48 μm , whereas at irradiated Mg/Al/Mg target, it decreases from about 8 mÅ to about 5 mÅ, see Figure 5.8. Since the L-dip position from the line center depends on the electron density N_e (via ω_p , see Eq.(5.7)), this fact indicates that the Mg plasmas provide better lateral confinement (compared to the CH plasmas) for the Al plasma. Indeed, since the plasma expansion velocity is inversely proportional to the square root of the ion mass, we can expect that Mg plasma expands by a factor close to 3/2 slower than CH plasma and thus keeps the Al plasma at higher densities. Moreover, this conclusion is supported also by measurements of the widths and shifts of Al Ly γ line. Since the line width and shift increase with increasing electron density (see Chapters 3 and 4), close to the irradiated target surface the Ly γ width and shift at Mg/Al/Mg target are about 27% and 30%, respectively, larger than those at CH/Al/CH target.

The dependence of L-dips on electron density offers an alternative method for de-

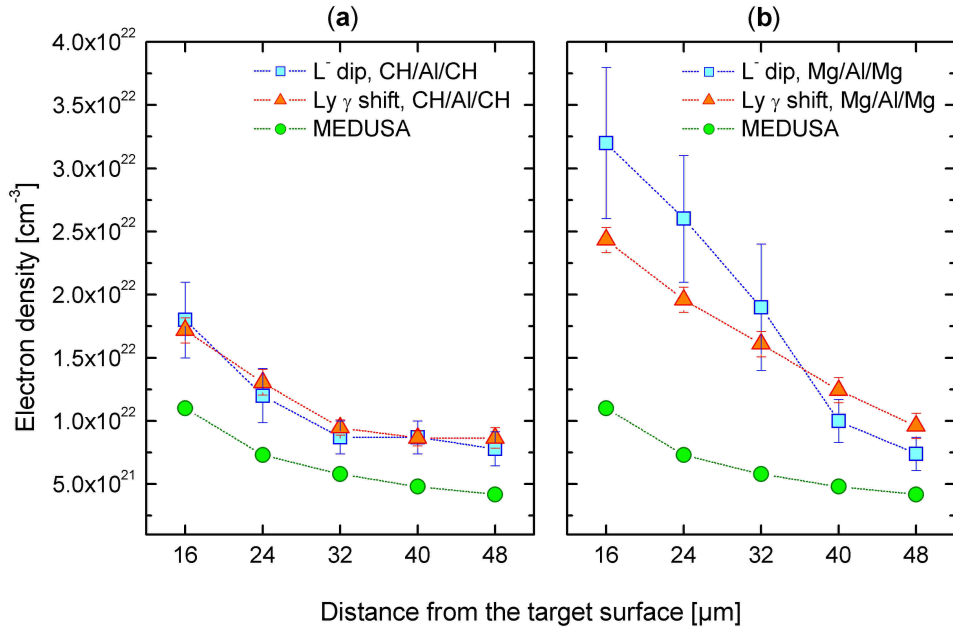


Figure 5.9: Comparison of electron densities deduced from L⁻ dips, line shifts, and the hydrocode MEDUSA: (a) CH/Al/CH target, and (b) Mg/Al/Mg target.

termining the electron density of the emitting plasma. This is done by measuring the position of the L-dip from the line center and by using Eq.(5.7). The consistency of the density diagnostic based in the L⁻ dips for the inference of electron densities in the range $5 \times 10^{21} \lesssim N_e \lesssim 3.5 \times 10^{22} \text{ cm}^{-3}$ is demonstrated in Figure 5.9, where the electron densities inferred from the L⁻ dips are compared with values deduced from the observed Al Ly γ line shifts and from simulations performed by the 1D hydrodynamic code MEDUSA (Christiansen *et al.*, 1974) in a planar geometry. The determination of electron densities from the measured Al Ly γ line shifts was based on the quantum mechanical impact theory (Nguyen *et al.*, 1986); the required electron temperatures were again estimated by means of the MEDUSA. For intermediately coupled plasmas, the density diagnostics based on the line shifts is shown to be a viable density diagnostics (Renner *et al.*, 2003).

The electron densities derived by means of the L-dips compare favorably with electron densities derived by means of the line shifts. In the case of CH/Al/CH target, the results agree to within 8%, whereas at the irradiated Mg/Al/Mg target, the disagreement is less than about 26%. The electron densities derived by means of the hydrocode MEDUSA are smaller by a factor 1.8-3 relative to those inferred by means of L-dips. The discrepancies are more pronounced for Mg/Al/Mg target because the 1D code

MEDUSA in a planar geometry does not incorporate the possibility to simulate in detail the hydrodynamics of structured targets (sandwiching of Al targets between Mg or CH substrates) so it does not distinguish between Mg and CH confinements. Other sources of discrepancy can be tentatively attributed to approximations made in the code, those done within the simulation and possible systematic or random errors of the experiment, as well. The results obtained, however, confirm that it is possible to use L-dips as a density diagnostics in intermediately coupled plasmas.

The spectral resolution of the spectrometer makes possible to determine reliably positions of the L-dips from the line center but it is insufficient to resolve sufficiently in all spectra the dip-minimum and the nearest bumps which surround them. As a consequence one can not determine reliably the amplitude of the oscillating electric field by measuring the distance between the dip minimum and the nearest bump, $\Delta\lambda_{1/2}^{dip}$; for a characteristic experimental value $\Delta\lambda_{1/2}^{dip} \approx 0.5 \text{ m\AA}$ measured at the CH/Al/CH irradiated target (16 μm from the target surface), Eq.(5.8) yields $E_0 \approx 7 \text{ MV/cm}$.

Figure 5.10 presents four experimental profiles of Al Ly γ measured at the laser irradiated Al_4C_3 target sandwiched between CH substrates. The line profiles are more structured than those measured at CH/Al/CH and Mg/Al/Mg irradiated targets. This difference is a consequence of the fact that, except Langmuir oscillations, the spectra are modified also by charge exchange. Charge exchange results in the formation of X-dips which are labelled with X_1 , X_2 and X_3 . They are located at about 5.6, 6.7 and 9.6 m\AA from the line center, respectively. Their positions from the line center do not depend significantly on the electron density. Dips X_3 are located in the low-intensity parts of the line profiles, thus their identification is burdened by the background noise. As shown in Section 5.2, X-dips which are labelled as X_1 , X_2 , and X_3 are the only X-dips which can be observed in Al Ly γ line profile. Theory presented in Section 5.2 predicts that, these dips should be located at 4.3, 6.7 and 8.6 m\AA from the line center. These numbers are a bit different from those published in (Renner *et al.*, 2005), which in fact are closer to the observed positions (3.2, 6.7 and 9.6 m\AA respectively). These differences result from the round-off errors involved in rounding the values of the physical constants such as Planck constant, speed of light in vacuum and electron mass, which can produce errors of the order of m\AA (in the previous section, computations were performed using six digits after the decimal point).

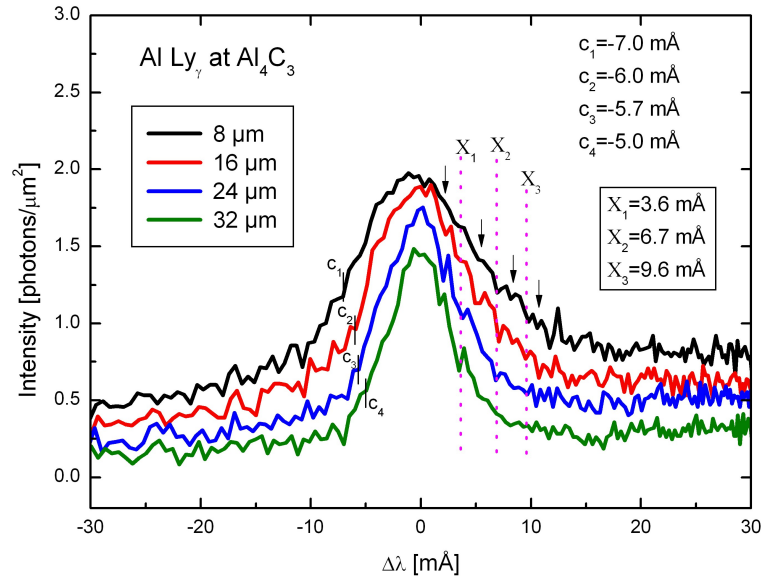


Figure 5.10: Ly γ line profiles emitted from Al_4C_3 irradiated target ($60 \mu\text{m}$ thick) sandwiched between CH substrates ($40 \mu\text{m}$ thick). The spectra are influenced from Langmuir oscillations and charge exchange. X-dips are labelled with X_1 , X_2 and X_3 , whereas Langmuir dips are labelled with c (with corresponding indices). Vertical arrows indicate positions of the bumps which surround the X-dips.

Another convincing argument which leads to the conclusion that the spectral features (labelled with X_1 , X_2 , and X_3) in Figure 5.10 are X-dips and *not* a random noise is, their *nonexistence* in CH/Al/CH and Mg/Al/Mg targets (see Figures 5.5 and 5.6). At CH/Al/CH and Mg/Al/Mg irradiated targets, the Ly γ profiles are smoother due to the fact that, the avoided crossing (which is responsible for formation of X-dips, see previous section) cannot occur because $Z_r = Z_p$ (Neuman-Wigner theorem) (Gershtein and Krivchenkov, 1961; Oks and Leboucher-Dalimier, 2000a).

5.4 Summary and Conclusion

The experimental arguments presented in Section 5.3 and their interpretation based on the theoretical approach presented in Sections 5.1 and 5.2 confirm that, benefiting from the advanced X-ray instrumentation and sophisticated design of the experimental configuration, a reproducible fine structure in profiles of Al Ly γ emitted from the densest part of the hot Al plasma is observed.

The dips corresponding to the simultaneous interaction of the radiating ions with the ion microfields and dynamic electric fields originating from the electron plasma os-

cillations, are identified. Positions of these dips (L-dips) are dependent on the electron density; they are used to deduce electron densities of the emitting regions. Electron densities deduced from L-dip positions compare favorably with those derived from line shifts (to within 26 %). The results obtained confirm that it is possible to use L dips as a density diagnostics in intermediately coupled plasmas, thus suggesting a possibility to develop a new efficient tool for plasma diagnostics. Alternatively, the L-dip-based diagnostics can be used to prove the consistency of other diagnostics used, or to test theories of radiator-plasma interactions.

In the Al Ly γ emitted from irradiated Al₄C₃ targets, X-dips resulting from avoided crossing of radiating Al ion terms with carbon-perturbing terms were observed. X-dips observed at laser irradiated Al₄C₃ targets, where the radiating aluminum ions ($Z_r = 13$) are perturbed by carbon ions ($Z_p = 6$), are not observed at Al foils where the radiating ions and perturbing ions have the same nuclear charge ($Z_r = Z_p$), which confirms the impossibility of the crossing of terms for $Z_r = Z_p$.

Chapter 6

Semiconductor-Metal Phase Transition in SmS

6.1 General Considerations

Samarium mono sulphide (SmS) has attracted a considerable experimental and theoretical attention due to its interesting optical (Jayaraman *et al.*, 1970; Batlogg *et al.*, 1976), electrical (Jayaraman *et al.*, 1970), magnetic (Maple and Wohlleben, 1971; Birgeneau *et al.*, 1972) and mechanical properties (TuHailing *et al.*, 1984), its possible application for data storage (Pohl *et al.*, 1974; Kaminskiĭ, 1978) and conversion of thermal energy to electric energy (Kaminskiĭ and Solov'ev, 2001).

SmS at atmospheric pressure is an ionic semiconductor of NaCl-type structure (see Figure 6.1) with lattice constant of 5.97 Å (Jayaraman *et al.*, 1970), band gap* of about 0.2 eV (Landolt-Börnstein, 2001), and is nominally Sm²⁺S²⁻.[†] This chapter is concerned with semiconductor-to-metal phase transition in SmS. In this section and the next one, some experimental results concerning phase transition, and the theoretical framework in which they can be understood are discussed.[‡] The experimental results concerning the pressure- and temperature-induced phase transitions in SmS are presented in Section 6.3.

A great number of papers (see e.g. review by Smirnov and Oskotskii, 1978 and references therein) after Jayaraman *et al.* (1970), experimentally verified that SmS undergoes a first order *phase transition* to the metallic state at a critical pressure of about 0.65 GPa (0.65×10^9 Pa) and temperature of about 293°K. At this pressure, both the

*The published values for the band gap fluctuate between 0.1-0.4 eV; they are listed in Appendix F.

†The electronic configuration of Sm is [Xe]4f⁶6s², whereas that of S is [Ne]3s²3p⁴.

‡For applications of SmS, see Appendix G.

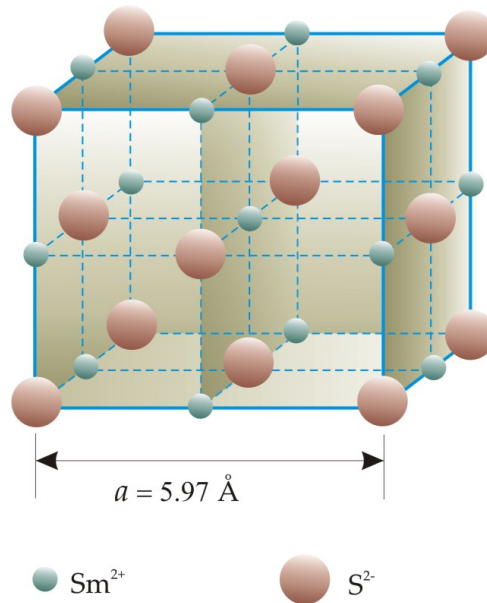


Figure 6.1: Crystal structure of SmS. At atmospheric pressure and ambient temperature, SmS is an ionic semiconductor of NaCl-type structure with lattice constant of 5.97 \AA , black color and is nominally $\text{Sm}^{2+}\text{S}^{2-}$.

resistivity and the lattice constant abruptly decrease (Jayaraman *et al.*, 1970). The reflectivity measurements (Kirk *et al.*, 1972) also revealed that between 0.6 and 0.65 GPa the reflectivity changes by at least one order of magnitude, reaching thus the metallic-reflectivity value and then remains constant (the absolute value of reflectivity in the metallic state at wavelengths greater than $0.8 \mu\text{m}$ is at least 85% of that of aluminum).

The abrupt decrease in resistivity (about 70 %), the sharp decrease in volume (about 10-13%) and the increase on the reflectivity (about one order of magnitude), reflect the occurrence of first order semiconductor-metal phase transition in SmS at about 0.65 GPa and 293°K . The phase transition is a *reversible* process but, due to the multiple cracking of the crystal during the reverse transition, it can happen that the measured quantities such as reflectivity or resistivity, are not necessarily returned to the initial values (Kirk *et al.*, 1972). The metallic phase has a characteristic *golden yellow* color. The high-pressure X-ray powder data reveal that this transition is *iso-structural* (i.e., the NaCl-type structure is retained) up to very high pressure $\sim 10 \text{ GPa}$ (Jayaraman *et al.*, 1970).

High pressure resistivity measurements and optical studies have established that the phase transition involves the delocalization of a $4f$ -electron in Sm ion from $4f$ to $5d$ (i.e., it involves a $4f^6 \rightarrow 4f^5 5d^1$ Sm-ion configurational change) which implies the conversion of Sm^{2+} toward Sm^{3+} (Jayaraman *et al.*, 1970; Kirk *et al.*, 1972). The crystal

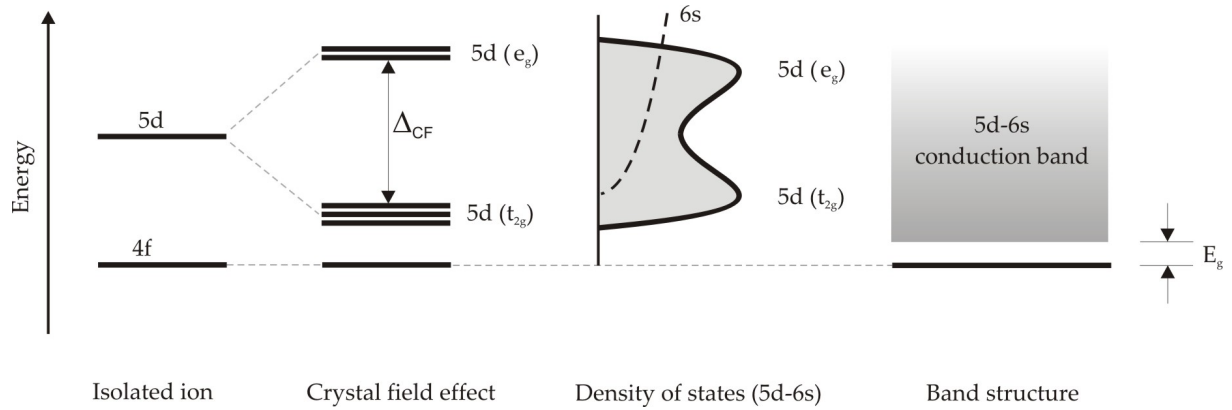


Figure 6.2: Schematic electronic structure of SmS in the semiconducting phase (see text).

field splits the $5d$ states into three lower-energy orbitals, called t_{2g} levels, and two higher-energy orbitals called e_g levels, see Figure 6.2. The energy difference between the two sets of levels (the crystal field splitting energy) Δ_{CF} is about 2.3 eV (Kaldis and Wachter, 1972). The $5d$ -band hybridizes with $6s$ -band whereas $4f$ levels are of atomic nature (Shapiro *et al.*, 1975) and little affected by the crystal environment. It should be emphasized that, the question whether $6s$ band is lower in energy than the bottom of $5d$ t_{2g} band is subjected to some controversy. According to Wachter (1994), the bottom of the $5d$ -band is lower in energy than $6s$ -band. His conclusions are based in optical absorption measurements, namely, the lowest energy optical absorption corresponds to $4f \rightarrow 5d$ transition and not to $4f \rightarrow 6s$ transition. On the other hand, based on the thermal conductivity measurements, Smirnov and Oskotskiĭ (1978) claim that the $6s$ -band is located lower in energy than the $5d$ t_{2g} -band. However, the shift of the thermally determined energy gap (-100 meV/GPa= -10 meV/kbar), which is equal to that determined from the absorption edge under pressure (Wachter, 1994), reveal that the $5d$ t_{2g} -band must be the lowest band.

The main effect of pressure is an increase of Δ_{CF} due to a reduction of lattice constant, thus decreasing the $4f - 5d(t_{2g})$ energy difference. The semiconductor-metal transition will occur when Δ_{CF} -splitting becomes so large that the bottom of the lowest $5d$ band coincides with the $4f$ state (Kaldis and Wachter, 1972).[§]

Because of the strong shielding of the outer $5s$ and $5p$ electrons from the nucleus by the $4f$ shell, the absence of one $4f$ electron decreases the ionic radius, i.e., the radius of

[§]Since energy gap, E_g , decreases at a rate of about -100 meV/GPa (Varma, 1976), at the transition pressure of 0.65 GPa, the energy gap should be reduced to the value of 0.065 eV, which is close to the activation energy of the defects (about 0.06 eV, see e.g. Batlogg *et al.*, 1976).

Table 6.1: Ionic radii of Sm^{2+} , Sm^{3+} and S^{2-} (after Varma, 1976).

Ion	Ionic radii [\AA]
Sm^{2+}	1.14
Sm^{3+}	0.96
S^{2-}	1.84

Sm^{2+} will be decreased due to the removal of an $4f$ electron. The ionic radii of Sm^{2+} , Sm^{3+} and S, are listed in Table 6.1. Therefore, the fluctuating valence in a rare-earth ion directly causes a fluctuation in the ionic diameter and thus affects lattice vibrations. Furthermore, because of the strong Coulomb attraction among the rare-earth ion and its surrounding chalcogen ions, the fluctuating valence induces local lattice distortion around the relevant rare-earth ion. Conversely the lattice vibrations seriously affect the valence fluctuations. The interplay between valence fluctuations and lattice vibrations is analyzed theoretically by Ghatak and Bennemann (1978), Kuroda and Bennemann (1981), and, Ichinose and Kuroda (1982). Ghatak and Bennemann (1978) outlined a theory which shows that primarily only short wavelength optical phonons are affected by valence fluctuations. For a system like SmS, valence fluctuations may cause softening of the longitudinal optical phonons. Ichinose and Kuroda (1982) found that both branches, acoustic and optical, are affected from valence fluctuations. Their hardening or softening depends on the electron-phonon interaction; the explicit formulas are presented in the referred article.

Another interesting property of SmS is its magnetic susceptibility. Divalent Sm ion (i.e., Sm^{2+}) has a non-magnetic ground state 7F_0 and thus will give rise to a *van Vleck paramagnetism* due to thermal population of the 7F_1 state which lies about 35 meV above (Wachter, 1994). Maple and Wohlleben (1971) found that at about 0.6 GPa the magnetic susceptibility drops by 65% (the values of the magnetic susceptibility and its derivative with pressure are listed in Appendix F). In the metallic phase, under pressure (0.75-1.2 GPa), down to the temperature of 0.4 K no magnetic ordering is found, nor is a Curie like contribution to the susceptibility present. This fact indicates that in the metallic phase SmS is *non-magnetic*.

Pressure-induced phase transitions are reported also for other rare earth chalcogenides such as SmTe, SmSe, TmTe, YbTe, etc. (Jayaraman *et al.*, 1970; Chatterjee *et al.*,

1972); also, there are a number of rare-earth ions (R) such as Gd, Er, Ho, Tm, Yb, Y, Er, Dy, Nd, Ce, etc. (Jayaraman *et al.*, 1975), which form compounds of the form $\text{Sm}_{1-x}\text{R}_x\text{S}$ and at appropriate concentration x exhibit *isostructural* semiconductor-metal phase transition.

6.2 Intermediate Valence

The lattice parameter is a powerful and direct indicator of what is happening at the microscopic level in SmS under pressure and temperature. The lattice parameter changes reflect changes in the size of the Sm ion, which in turn reflect changes in the valence state. The lattice constants that characterize the divalent Sm^{2+}S and fully trivalent Sm^{3+}S are, respectively, 5.97 and 5.62 Å (Jayaraman *et al.*, 1975). Any lattice parameter intermediate in value suggests an intermediate or mixed valence state for the Sm ion. Denoting by $v = 2 + n_d$ the intermediate valence of the Sm ion, where n_d stands for the trivalency character of the Sm ion (if $n_d = 1$, the Sm ion is tri-valent, alternatively, if $n_d = 0$, the Sm ion is di-valent), the intermediate valence can be deduced from the measured lattice constant, a , by using the Vegard's law (Varma and Heine, 1975; Denton and Ashcroft, 1991)

$$n_d = \frac{a_2 - a}{a_2 - a_3} \quad (6.1)$$

where a_2 and a_3 are lattice constants for the pure di- and tri-valent SmS. The intermediate valence of the Sm ion under pressure predicted by the Vegard's law (i.e., Eq.(6.1)) is displayed in Figure 6.3. Magnetic susceptibility measurement under pressure (Maple and Wohlleben, 1971) and lattice parameters (Jayaraman *et al.*, 1974) have firmly established that in the high-pressure metallic phase of SmS, the Sm ions do not assume the fully trivalent value of the lattice constant, i.e., the value of the lattice constant is not 5.62 Å but instead 5.70 Å indicating an *intermediate valence* close to 2.8, which is in agreement with that computed by Eq.(6.1). The interesting question is how one does picture an intermediate valence state. There are two ways in which such a state can be viewed. The first approach can be stated as follows: every Sm ion in the crystal fluctuates in time between $4f^6$ (Sm^{2+}) and $4f^55d^1$ (Sm^{3+}) states on a rapid time scale (believed to be of the order of 10^{-12} s, after Jayaraman *et al.*, 1975); the relative time the electron spends in one of the two configurations determining the extend of the intermediate valence. In this situation the fluctuation rate may be so rapid that the lattice is

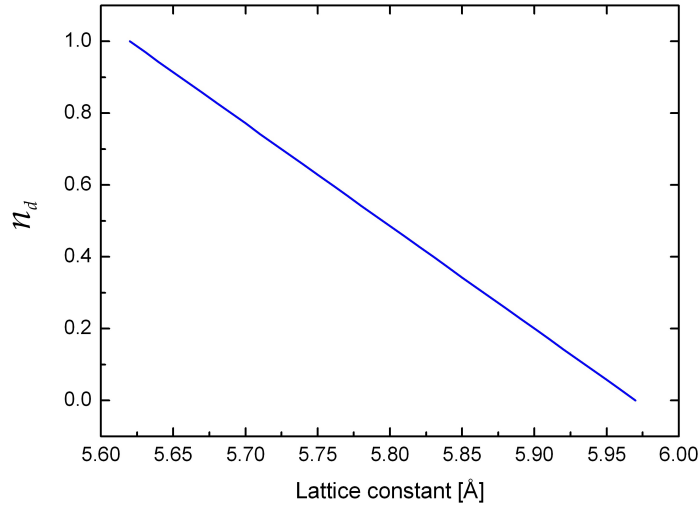


Figure 6.3: The trivalency character of the Sm ion under pressure, predicted by the Eq.(6.1)

not able to follow fully the electronic state and all the Sm ions stabilize at some intermediate size. This is the dynamic description that is called *inter-configurational fluctuation model* (Jayaraman *et al.*, 1975; Coey *et al.*, 1976). Thus, according to inter-configurational model, two configurations for the Sm ion are degenerate in energy ($4f^6$ and $4f^55d^1$) and the ion switches rapidly back and forth between the two. The average electronic configuration of the Sm ion is thus

$$n_d[4f^55d^1] + (1 - n_d)[4f^6] \quad (6.2)$$

where n_d characterizes the tri-valency character. The ^{149}Sm Mössbauer spectra measurements at room temperature and under applied pressures 0-1.1 GPa (Coey *et al.*, 1976) suggest that, in the mixed-valent state the fraction of trivalency is $n_d \approx 0.7$. On the basis of inter-configurational fluctuation model one can envision the collapsed phase of SmS as having in time average 0.7 electron in the conduction band and 5.3 electrons in the $4f$ shell of the Sm ion. Similar value ($n_d \approx 0.7$) is predicted also from the magnetic susceptibility measurements (Maple and Wohlleben, 1971). The Mössbauer spectra also reveal that the upper limit of the valence fluctuation time is $\tau \lesssim 10^{-9}$ s. However, the magnetic susceptibility measurements and Jayaraman *et al.* (1975) suggest that the inter-configurational fluctuation period is believed to be $\tau \approx 10^{-12}$ s.

The other approach to picture intermediate valence is to consider the Sm^{2+} and

Sm^{3+} ions as a distinct species (small ion and large ion) intimately mixed and completely disordered on an atomic scale. The valence does not fluctuate from one to the other state with time and stays static and spatially frozen. Hence we may use the average number n_d of $5d$ electrons per Sm ion to represent the average atomic concentration of Sm^{3+} ions in the system, and thus a tri-valency character

$$n_d \equiv \frac{N(\text{Sm}^{3+})}{N(\text{Sm}^{3+}) + N(\text{Sm}^{2+})} \quad (6.3)$$

where $N(\text{Sm}^{3+})$ and $N(\text{Sm}^{2+})$ are the numbers of Sm^{3+} and Sm^{2+} ions.

6.3 Pressure and Temperature Induced Phase Transitions in the Surface of SmS Crystal

A practical technique to drive semiconductor-metal phase transition in SmS is to polish the surface of the crystal. When SmS crystal is polished, its surface acquires the golden-yellow color due to the introduction of the residual compressive stress (greater than 0.65 GPa) in a thin layer of about 1000 Å. The surface of the SmS crystal before and after polishing is shown in Figure 6.4(a). The X-ray diagnosis of the phase transition was done by using Bragg-Brentano focusing technique[¶] (002 reflection, Ti K α : $\lambda=2.748$ Å). The metallic phase is observed at a Bragg angle $\theta_{B,m} \simeq 28.88^\circ$, which corresponds to the lattice constant $a_m \cong 5.69$ Å; for this value of the lattice constant, according to Jayaraman *et al.* (1970), the residual compressive stress in the metallic state is about 0.72 GPa. Additionally, by using Eq.(6.1), the measured lattice constant a_m yields an intermediate valence of about 2.8, which is comparable with those outlined in Section 6.2.

The metallic phase disappeared after the crystal was heated to about 150°C, see Figure 6.4(b), which is similar to that reported by Pohl *et al.* (1974). This happens because, as a response to heating, the crystal will expand and thus reduce a compressive residual stress to values lower than 0.65 GPa. This will drive the energy gap to values larger than 0.065 eV and thus transform the metallic layer to the semiconducting phase.

[¶]In this technique, X-rays are focused by rotating the crystal around Bragg angle; for details see e.g. Bertin (1975).

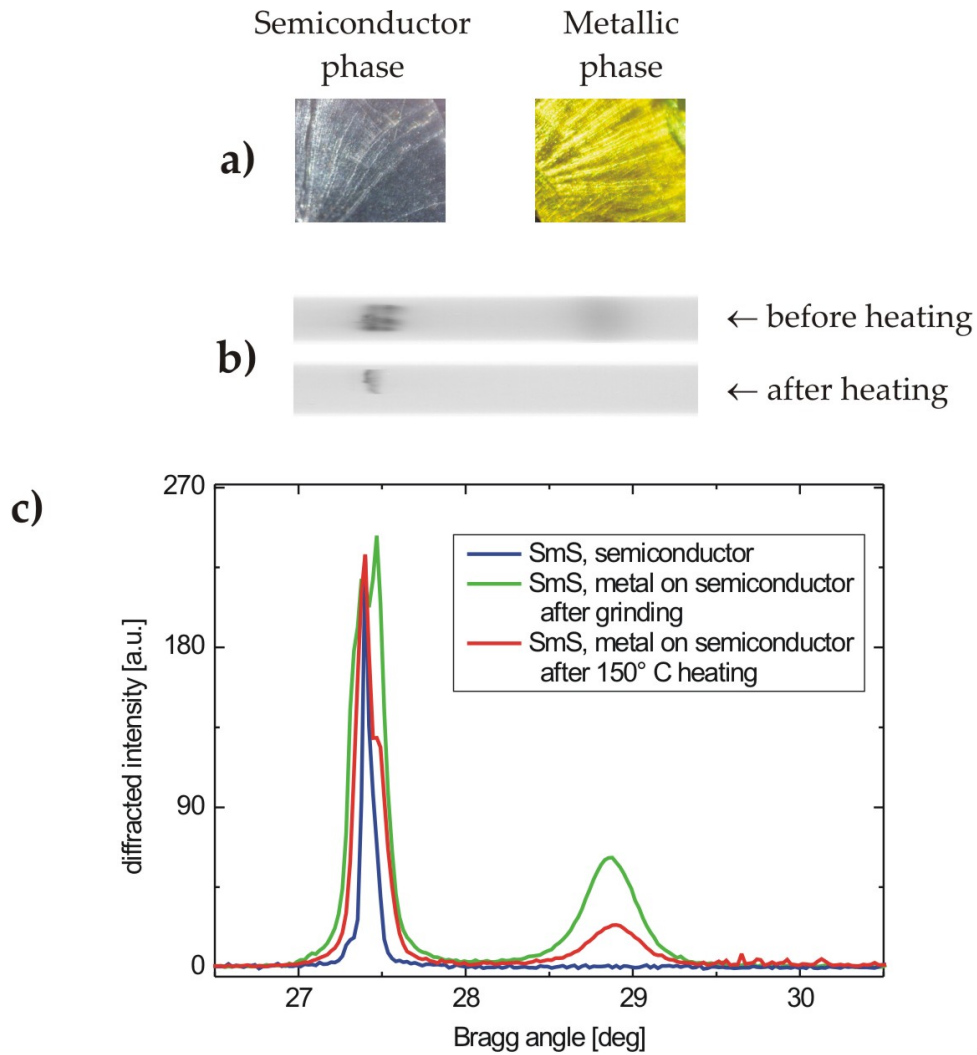


Figure 6.4: Phase transition in SmS: (a) surface of the SmS crystal before and after polishing, (b) comparison of X-ray films before and after heating of the SmS crystal, respectively and (c) the measured rocking curves before and after polishing and heating of the SmS crystal.

6.4 Summary and Conclusions

In this Chapter, besides a survey of the experimental results concerning phase transition in SmS, the semiconductor-metal ($s - m$) and metal-semiconductor ($m - s$) phase transitions in SmS are reported. The $s - m$ phase transition is induced by polishing the crystal, whereas, the $m - s$ phase transition is induced by heating the crystal to about 150°C . The measured lattice constant of the metallic phase revealed an intermediate valence of about 2.8. This value is comparable with those predicted by Mössbauer spectroscopy and magnetic susceptibility measurements.

Chapter 7

Ultrafast Structural Dynamics in SmS Probed by Time-Resolved X-Ray Diffraction

7.1 Introduction

Time-dependent phenomena are monitored by performing time resolved experiments. A time-resolved experiment inherently begins with initiation of the process under study, at some more or less accurately defined instant in time. The most frequent initiation can be done with a pulse of light which is termed the "pump" pulse. The subsequent development then is investigated by probing the sample using an ultra-short pulse of X-ray radiation, called "probe" pulse.

Time resolved X-ray diffraction experiments with nanosecond resolution have been used for about 20 years to study structural processes in solids such as annealing, crystallization or shock propagation (Larson *et al.*, 1982; Wark *et al.*, 1992; Helliwell and Rentzepis, 1997). Advances in the generation of ultrashort laser pulses (Shank, 1993; Hirlimann, 1998), have made it possible to investigate fundamental processes such as chemical reactions, phase transitions, and surface processes which occur on timescales comparable to the natural oscillation periods of atoms and molecules, i.e., in the range of femtoseconds ($1 \text{ fs} = 10^{-15} \text{ s}$) to picoseconds ($1 \text{ ps} = 10^{12} \text{ s}$). Indeed, these advances have taken us from the picosecond timescale (Wang *et al.*, 1989) a generation ago, to the femtosecond timescale (Callan, 2000) in the past decade, and recently into the attosecond ($1 \text{ as} = 10^{-18} \text{ s}$) regime (see e.g. Silberberg, 2001).

Some experiments of relevance to biology and chemistry are real-time studies of photoinitiated reactions in molecules such as myoglobin and photoactive yellow protein

(Srajer *et al.*, 1996; Perman *et al.*, 1998), investigation of short-pulse-laser irradiation of organic films (Rischel *et al.*, 1997) and the recombination of laser-dissociated iodine molecules dissolved in CCl_4 (Plech *et al.*, 2004). Experiments utilizing laser produced plasma X-ray sources, demonstrated the use of X ray diffraction to investigate nonthermal melting and diffraction from a coherent acoustic pulse induced by laser heating of semiconductor crystals (Rose-Petruck *et al.*, 1999; Rouse *et al.*, 2001a; Sokolowski-Tinten *et al.*, 2003).

In this Chapter, the observation of coherent acoustic phonon propagation in semiconducting SmS, using a laser driven plasma X-ray femtosecond pulses, is reported. Since valence fluctuation in Sm ion is associated with fluctuation in the ionic diameter (see Chapter 6), which consequently induces lattice distortion around Sm ion, time resolved investigation of structural changes in SmS can be a useful tool in providing insights into the phase transitions, as well as in electron-phonon coupling. The time resolved diffraction data demonstrate that, it is possible to obtain quantitative information on atomic motions in bulk media during picosecond-scale lattice dynamics. A brief theoretical conception of laser-plasma-driven femtosecond X-ray pulses is outlined in Section 7.2. The approach used to interpret the structural dynamics is presented in Section 7.3. The experimental results on the time resolved diffraction from expansion/compression regions of the SmS crystal are presented in Section 7.4.

7.2 Femtosecond Laser Plasma X-Ray Sources

For investigations of fast temporal processes like phase transitions, chemical reactions and lattice vibrations it is essential to develop efficient, bright ultrashort (ps or sub ps time scale) X-ray pulses since the nature of these processes is determined by atomic motions on these time scales. Several techniques have emerged for generating ultrafast X-ray pulses. Modern synchrotrons deliver intense polychromatic radiation in pulses with duration of around 30 ps (Rouse *et al.*, 2001a). Much weaker pulses of 300 fs duration have been generated by Thomson scattering of intense laser pulses on relativistic electrons (Schoenlein *et al.*, 1996). A third, completely differently approach is to use sub-picosecond laser pulses. In contrast to lasers with pulse durations of several hundred picoseconds or even nanoseconds, the focused laser intensities can easily reach values above 10^{17} W/cm^2 . Such intensities are many orders of magnitude above

the plasma formation threshold of a solid, and thus a plasma is created in front of the solid target. The thickness of the created plasma is of the order of the penetration depth of the laser radiation in the target material, which ranges from a few tens up to a few hundreds of nanometers. A significant amount of the absorbed laser energy is converted to accelerated electrons with energies of several hundred of keV (Kmetec *et al.*, 1992). These electrons lose their energy in a solid target producing bremsstrahlung (hard X-rays) and characteristic line radiation.

The number of X-ray photons which are emitted from the irradiated target of atomic number Z (the total $K\alpha$ yield) is highest for an optimal laser intensity* (Reich *et al.*, 2000) which is given by

$$I_{opt}[\text{W}/\text{cm}^2] = 7 \times 10^9 Z^{4.4} \quad (7.1)$$

$K\alpha$ emission starts after the laser pulse hits the plasma, when the first hot electrons are generated and enter the solid. After the laser pulse has gone, it continues until the energy of the last hot electron in the solid has dropped below the K-shell ionization energy. The total duration of the X-ray emission is the sum of the duration of the laser pulse τ_l and the "afterglow" emission τ_a (Reich *et al.*, 2000): $\tau_x = \tau_l + \tau_a$. Depending on the laser intensity, a small fraction of "super-hot" electrons can produce a long lasting $K\alpha$ afterglow with low intensity, which will have a negligible influence on observations. The temporal figure of merit of the $K\alpha$ pulse (τ_x) is defined as the time of the first 90% of emission. Afterglow emission can be restricted by using foil targets, which are quickly traversed by super-hot electrons, limiting the time they can produce X-rays.

The dependence of the time duration of $K\alpha$ pulse, τ_x , on a foil thickness is expressed as (Reich *et al.*, 2000)

$$\tau_x[\text{fs}] = \tau_l[\text{fs}] + \left(\frac{l[\mu\text{m}]}{0.0032Z^{0.5}} \right)^{\frac{1}{1.25}} \quad (7.2)$$

For instance, the time duration of $K\alpha$ pulses emitted from an irradiated ($\tau_l = 80$ fs) Ti-foil target ($Z = 22$), 25 μm thick, is about 460 fs.

*The number of generated X-ray photons depends on the ratio between the electron incidence energy and K-shell ionization energy; when this ratio is smaller than 20, most of the generated photons can escape from the target (for more details see Reich *et al.* (2000)).

7.3 Generation of Strain Pulses in SmS by Femtosecond Laser Pulses

Perturbation of the crystal with ultrashort laser pulses initiates structural changes in the crystal lattice. In semiconductors, the light will produce electrons and holes in a thin layer near the front of the sample (typically about absorption length of the laser light-for SmS at $\lambda_{laser} = 800$ nm, it is about 143 nm). These electrons and holes will emit phonons as they diffuse into the interior of the material, i.e., they lose their energy to the lattice, resulting in the increase of the lattice temperature. The increase in temperature of the lattice sets up a thermal stress which launches an elastic wave (Thomsen *et al.*, 1986). Detection of this elastic wave plays a very important role in understanding electron diffusion and thermalization, as well as in testing theories of the electron-electron and electron-phonon scattering (Tas and Maris, 1994; Lindenberg *et al.*, 2000). Experiments that demonstrated picosecond time resolved X-ray diffraction to study impulsive strain generation in semiconductors such as GaAs and InSb are shown by e.g. Rose-Petruck *et al.* (1999) and Morak (2003).

The theoretical approach presented in this section serves as a basis for interpretation of experimental results presented in the next section. The approach commonly used to interpret the strain-pulse shapes is the one-dimensional thermoelastic model proposed by Thomsen *et al.* (1986).

Under assumption that the absorption length ζ of the pump-laser pulse is much smaller than the sample thickness d , and the illuminated area A is larger than ζ and d , the energy deposited per unit volume at a distance z (see Figure 7.1) in the sample is

$$W(z) = (1 - R) \frac{F}{\zeta} \exp\left(-\frac{z}{\zeta}\right) \quad (7.3)$$

where R is the reflectivity of the sample, $F = Q/A$ is the laser fluence, and Q is the laser pulse energy. This heating gives a temperature rise

$$\Delta T(z) = \frac{W(z)}{C} \quad (7.4)$$

where C is the specific heat per unit volume. This temperature rise sets up an isotropic thermal stress given by

$$\sigma_{thermal} = -3B\beta\Delta T(z) \quad (7.5)$$

where B is the bulk modulus and β is the linear expansion coefficient. The thermal expansion launches a longitudinal strain pulse into the crystal, which is given by

$$\eta(z, t) = (1 - R) \frac{F\beta}{\zeta C} \left(\frac{1 + \nu}{1 - \nu} \right) \times \left\{ \exp \left(-\frac{z}{\zeta} \right) \left[1 - \frac{1}{2} \exp \left(-\frac{v_s t}{\zeta} \right) \right] - \frac{1}{2} \exp \left(-\frac{|z - v_s t|}{\zeta} \right) \text{sgn}(z - v_s t) \right\} \quad (7.6)$$

where v_s is the longitudinal sound velocity given by

$$v_s = \sqrt{3 \left(\frac{1 - \nu}{1 + \nu} \right) \frac{B}{\rho}} \quad (7.7)$$

ν is the Poisson's ratio[†], and ρ is the density of the material (sample).

Eq.(7.6) gives the strain profile in the direction of the sample normal (z -direction). Figure 7.1 shows two strain curves (for SmS), predicted by Eq.(7.6). From the figure it is obvious that the strain can be divided in two parts: the region near the target surface ($z = 0$) which has a time independent strain due to the thermal expansion, and the strain pulse which propagates away from the surface with the longitudinal sound velocity. The position in the crystal where the strain changes the sign (the jump position) is given by $v_s \Delta t$, where Δt is the pump-probe delay. The time for the acoustic wave to leave the region that is heated by the laser pulse is

$$\tau_{ac} = \frac{\zeta}{v_s} \quad (7.10)$$

In the calculation of the strain profile given by Eq.(7.6), diffusion of the heat deposited by the laser pulse is not included. The inclusion of this effect modifies the strain pulse shape (Thomsen *et al.*, 1986). However, the inclusion of the heat diffusion depends on the time for a significant fraction of the heat to diffuse out of the region that is heated by the laser pulse

$$\tau_{diff} = \frac{\zeta^2}{D} = \zeta^2 \frac{C}{\kappa} \quad (7.11)$$

[†]The Poisson's ratio and bulk modulus of a cubic crystal can be calculated in terms of the elastic constants using following expressions (Gersten and Smith, 2001):

$$\nu = \frac{C_{12}}{C_{11} + C_{12}} \quad (7.8)$$

$$B = \frac{C_{11} + 2C_{12}}{3} \quad (7.9)$$

where C_{11} and C_{12} are elastic constants; for SmS they are listed in Appendix F.

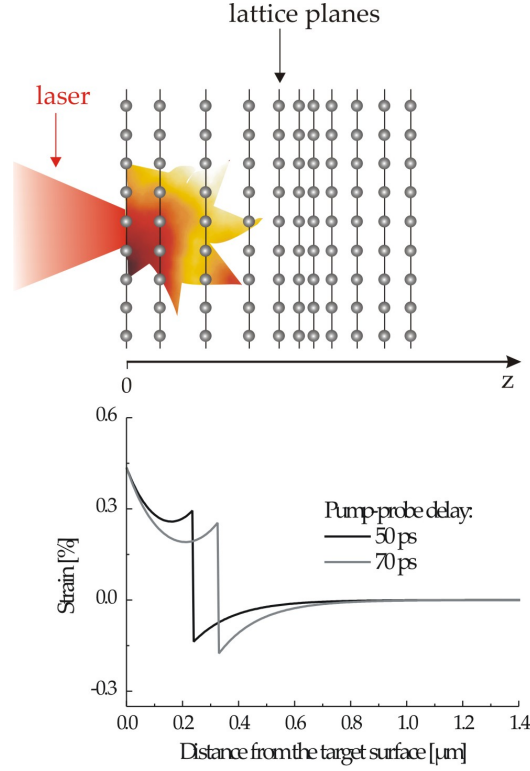


Figure 7.1: Impulsively excited strain pulses.

where D is the thermal diffusivity and κ is the thermal conductivity. If τ_{diff} is comparable or less than τ_{ac} , then the heat diffusion will change significantly the strain pulse (Thomsen *et al.*, 1986). For SmS ($v_s \approx 4700$ m/s, $C = 1.8 \times 10^6$ J/(m³K), $\kappa=6.4$ W/(mK), see Appendix F), $\tau_{ac} \approx 30$ ps while $\tau_{diff} \approx 6$ ns; it results that the heat diffusion does not modify significantly the acoustic wave.

At a more general level one has to consider that the laser pulse changes the electron and phonon distribution functions $n_{el}(\mathbf{k})$ and $n_{phon}(\mathbf{k})$ by $\delta n_{el}(\mathbf{k})$ and $\delta n_{phon}(\mathbf{k})$, respectively. In the semiconductor phase, the light will produce electrons and holes. These electrons and holes will emit phonons as they diffuse into the interior of the material. These changes produce a stress which is given by (Thomsen *et al.*, 1986)

$$\sigma_{ij} = \sigma_{ij}^{el} + \sigma_{ij}^{phon} \quad (7.12)$$

where σ_{ij}^{el} is the electron-hole contribution and σ_{ij}^{phon} is the phonon contribution to the stress. The electron hole-contribution to the stress is (Thomsen *et al.*, 1986)

$$\sigma_{ij}^{el} = -B \frac{\partial E_g}{\partial P} \delta_{ij} N_{el} \quad (7.13)$$

where N_{el} is the total number of electrons (equal to the number of holes), E_g is the band gap, P denotes pressure, and δ_{ij} is the Kronecker delta. Due to the diffusion

and recombination, the spatial distribution of electrons will be modified, and hence the stress will be modified. For each photon of energy E which is absorbed, thermal phonons of energy $(E - E_g)$ are produced. The phonon contribution to the stress is (Thomsen *et al.*, 1986)

$$\sigma_{ij}^{phon} = -\frac{3B\beta}{C}(E - E_g)\delta_{ij}N_{el} \quad (7.14)$$

The electron and phonon contributions to the stress are generally of the same order of the magnitude, but may have different signs.

7.4 Time Resolved Experiments with SmS

7.4.1 Experimental Setup

The time resolved experiments were designed to examine the time resolved response of the SmS crystal and its possible implication in phase transition. They were performed with a chirped pulse amplification (CPA) Ti:sapphire laser system at IOQ in Jena. The experimental setup is shown in Figure 7.2. X-ray pulses were generated by focusing

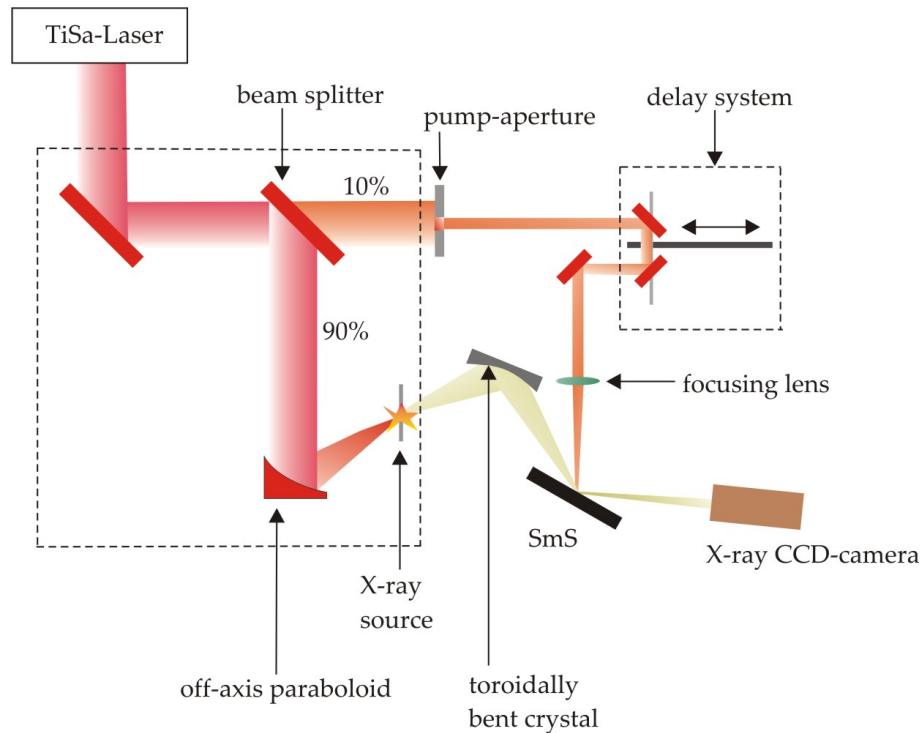


Figure 7.2: Scheme of the experimental setup: the Ti:sapphire system delivers pulses of about 80 fs with a pulse energy up to 200 mJ. 90% of the energy is focused onto a Ti band target by an off-axis paraboloid, producing Ti $K\alpha$ pulses. A fraction of the 10% transmitted laser energy is used to initiate structural changes in the SmS crystal. The changes are probed by the Ti $K\alpha$ pulses and detected by an X-ray CCD camera.

femtosecond pulses from a Ti:sapphire laser system, delivering 80-100 fs pulses with a

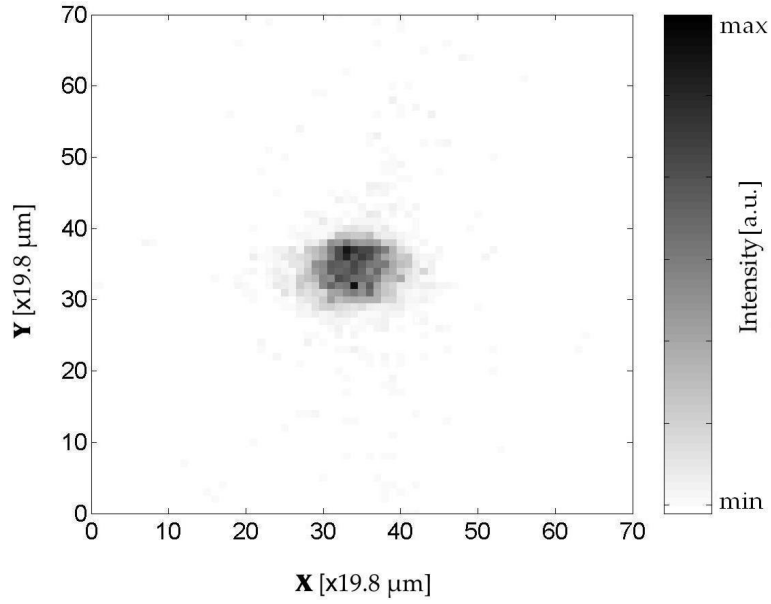


Figure 7.3: A typical Ti $K\alpha$ image of the X-ray emitting region obtained with Si bent crystal, 311 reflection, $\theta_B = 57.1^\circ$. The Ti $K\alpha$ pulse is composed of up to 7×10^4 photons. The CCD is placed in the Rowland circle; in this position the diameter of X-ray focus is about $200 \mu\text{m}$.

maximum energy up to 200 mJ and repetition rate of 10 Hz, onto a Ti band target (about $25 \mu\text{m}$ thick). The beam is directed from the vacuum compressor to the target chamber through a vacuum tube. In the target chamber (pressure 10^{-4} mbar) the incoming laser pulses were split by a 9:1 beam splitter. The main part of the pulse (90%) was focused on a Ti band target with a spot size of $10 \times 100 \mu\text{m}^2$ (horizontal \times vertical) corresponding to a maximum intensity of $2.5 \times 10^{17} \text{ Wcm}^{-2}$ (p-polarization).[‡] Fast electrons are produced during the laser-plasma interaction which then subsequently penetrate into the bulk material behind the plasma and produce characteristic Ti $K\alpha$ ($\lambda_{\alpha_1} = 2.748 \text{ \AA}$, $\lambda_{\alpha_2} = 2.752 \text{ \AA}$) line emission (see Section 7.2). The temporal duration of an Ti $K\alpha$ pulse is expected to be about 460 fs (see Section 7.2). The best focus of the plasma generating pulse was not used in order to reduce hard X-rays which can obscure information contained on the detector (X-ray CCD). The Ti $K\alpha$ radiation was focused onto SmS crystal (002 reflection, $\theta_B=27.4^\circ$) by using the 311 reflection of a toroidally bent Si crystal ($\theta_B^{\text{Si}}=57.1^\circ$, active area with diameter of 11 mm, $R_h = 149.79$ mm and $R_v = 106.39$ mm). Figure 7.3 shows the Ti $K\alpha$ image of the X-ray emitting region obtained with Si bent crystal. The Ti $K\alpha$ pulse is composed of up to 7×10^4 photons. The CCD is placed in the Rowland circle; in this position the diameter of X-ray focus is about $200 \mu\text{m}$.

[‡]The optimal laser intensity (see Eq.(7.1)) is $I_{opt} \approx 5.6 \times 10^{15} \text{ Wcm}^{-2}$.

The Bragg reflection from SmS crystal (002 reflection, $\theta_B = 27.4^\circ$) is recorded by using a CCD camera with a pixel size $19.8 \times 19.8 \mu\text{m}^2$. The width of the reflection curve is determined by the size of the $K\alpha$ source, and the intrinsic reflection curves of Si bent crystal and SmS crystal, respectively.

The remaining 10% of the laser pulse transmitted through a beamsplitter was used to initiate structural changes in the SmS crystal within a depth comparable to the penetration depth of infra-red laser pulse (143.7 nm). The delay between the optical pump and X-ray probe pulses is achieved by a delay system which consists of two 45° -mirrors mounted on motorized translational stage (see Figure 7.2). In order to realize the spatial and the temporal overlap, the laser pulse was attenuated so that no plasma formation occurred. Then, the spatial and the temporal overlap are adjusted by monitoring the splitted parts of the laser pulse on the visible-range CCD camera, and by using harmonic emission from BBO (BaBO_4) crystal, respectively.

The quality of the polycrystalline SmS is characterized by using the X-ray diffraction topography and by measuring the rocking curves at different positions on the crystal. It is found that the crystal is composed of grains with dimensions up to 2.7 mm and disoriented up to 1° relative to one another (see Appendix H). The pump-probe experiments were performed in single crystalline regions.

7.4.2 Experimental Results

The SmS crystal (002 reflection, $\theta_B=27.4^\circ$) was placed on the Rowland circle of the toroidally bent Si crystal. The structural changes, initiated by pump-pulses, are probed with Ti $K\alpha$ pulses. In order to obtain a good signal-to-noise ratio, the signal is accumulated over 200 shots. The pump fluence is controlled via the pump-aperture (see Figure 7.2).

Figure 7.4 shows the experimentally measured rocking curves for three delay times: 20, 40 and 60 ps, respectively, at the pump fluence of about $3 \text{ mJ}/\text{cm}^2$. The label 'unperturbed (1)' corresponds to the rocking curve measured at the beginning of the pump-probe measurement sequence, without disturbing the SmS crystal with pump pulses, while the label 'unperturbed (2)' corresponds to the rocking curve without pump pulses measured at the end of the measurement sequence (i.e., after the crystal was pumped many times). All rocking curves are measured at the same area in

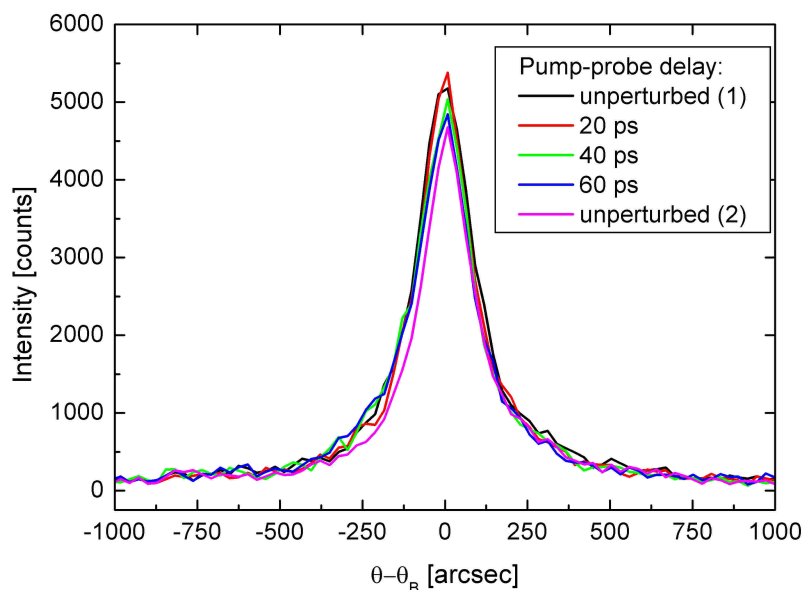


Figure 7.4: Time resolved rocking curves measured without pump pulses (labelled with 'unperturbed (1,2)'), and with pump pulses at the time delays of 20, 40 and 60 ps. Laser fluence: 3 mJ/cm².

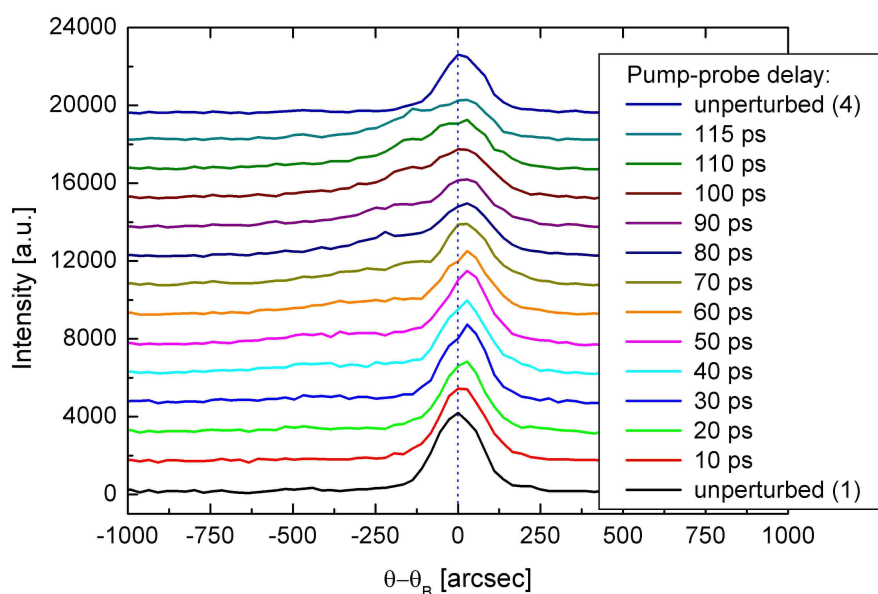


Figure 7.5: The experimentally measured rocking curves at the pump fluence of about 10 mJ/cm². The signal is accumulated over 200 shots. For presentation in a more comfortable comparative form, the rocking curves are shifted in intensity for 1500 counts. The label 'unperturbed (1,2)' corresponds to the reflection curve at the beginning (end) of the pump-probe measurement sequence, without disturbing the SmS crystal surface with pump pulses.

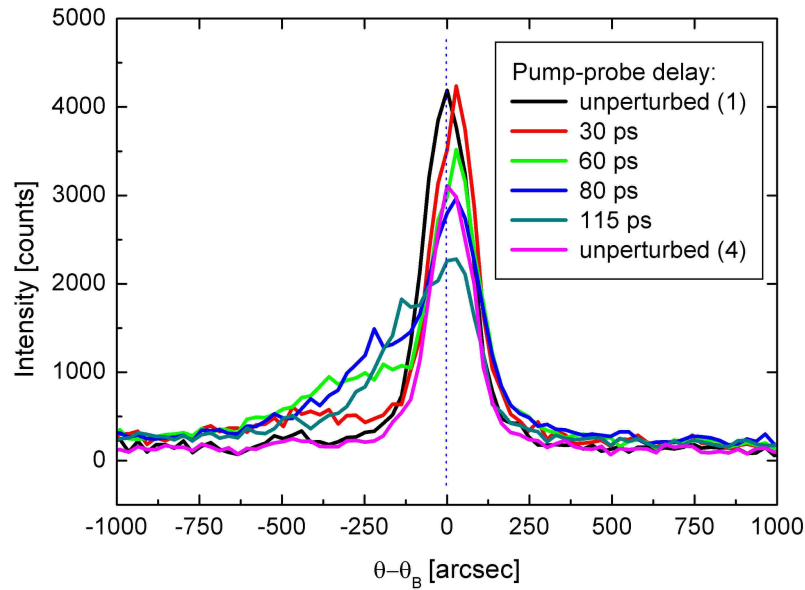


Figure 7.6: Time resolved rocking curves measured at the pump fluence of about 10 mJ/cm^2 without pump pulses (labelled with 'unperturbed (1,2)'), and with pump pulses at the time delays of 30, 60, 80 and 115 ps.

the SmS crystal. The only visible change on the rocking curves is the decrease of maximum intensity. This decrease is attributed to the debris created from a plasma and a possible damage of the crystal surface from pump-pulses. At this fluence (and also up to 10 mJ/cm^2) there is *no* obvious change in the rocking curves (the shape and the peak position) which would indicate any structural change which is initiated by the pump-pulses.

At the pump fluence of about 10 mJ/cm^2 , the rocking curves are broadened and shifted slightly toward smaller angles,[§] see Figure 7.5 and 7.6. The modification of the rocking curve profiles are more pronounced at smaller angles (negative $\Delta\theta$). At the end of the measurement sequence, the rocking curve has the same peak position and the same shape (Lorentzian-like) as one recorded at the beginning of the measurement sequence. The multi-peak analysis of the rocking curves measured at the time delays greater than 10 ps shows that, they are composed of two profiles: (i) the Bragg peak profile which corresponds to the diffraction from the unperturbed lattice planes, and (ii) a *satellite* peak profile which is located in the side of negative angles (negative $\Delta\theta$), which results from the disturbed lattice planes, see Figure 7.7. As the time delay be-

[§] The position of rocking curve peak is shifted up to about 27.5 arcsec, and, this value stays constant in all measurements where the pump-pulses are applied.

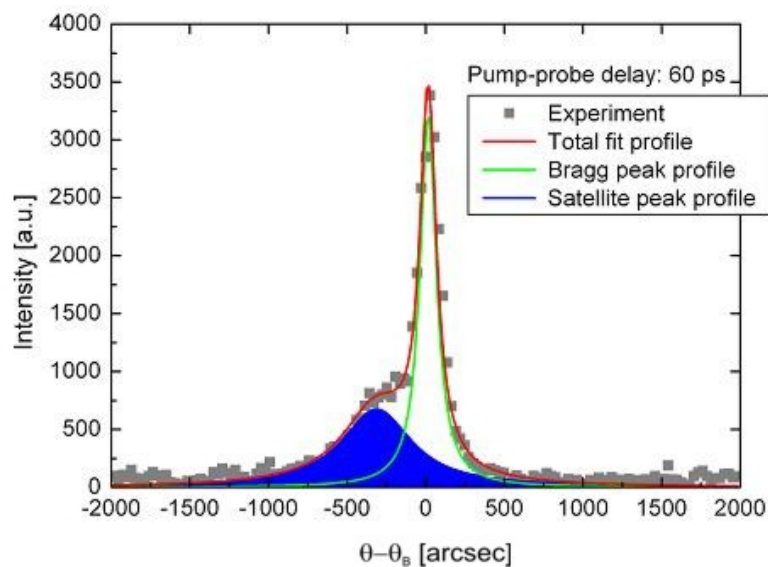


Figure 7.7: Multi-peak fitting with Lorentzian functions of a time resolved rocking curve measured at pump-probe delay of 60 ps and laser fluence of about 10 mJ/cm^2 . At the time delays greater than 10 ps, the rocking curves are composed of two profiles: (i) the *Bragg peak profile*, which corresponds to the diffraction from the unperturbed lattice planes, and (ii) a *satellite peak profile*, which is located in the side of negative $\Delta\theta$, which results from the disturbed lattice planes.

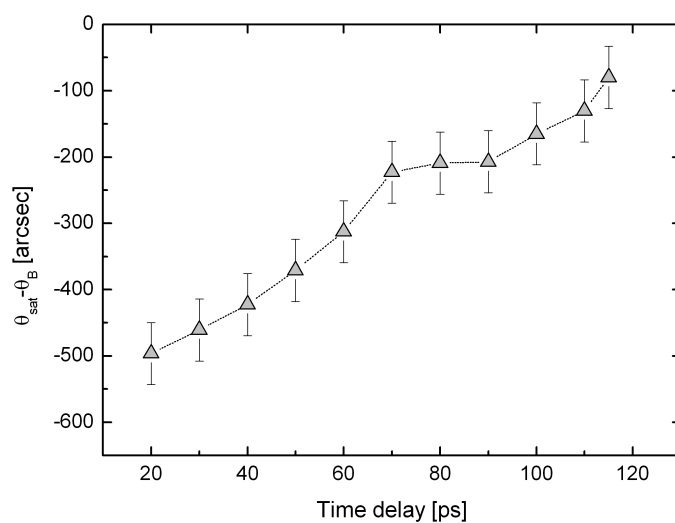


Figure 7.8: Position of the satellite peak relative to the Bragg angle. Laser fluence: 10 mJ/cm^2 .

tween pump and probe pulses is increased, the shift of the satellite peak position from the Bragg peak is decreased, see Figure 7.8.

At this fluence, as elaborated in Section 7.3, the impulsive heating of the crystal by *fs* pulses changes the population of the electrons and phonons in a crystal, i.e., the light will produce electrons and holes which transfer their excess energy to the lattice by generating coherent acoustic phonons (Thomsen *et al.*, 1986) across a range of wave vectors near the Brillouin zone center with a width $\sim 3 \times 10^7 \text{ m}^{-1}$. The changes in electron and phonon distribution drive a thermal stress which in turn drives an expansion/compression strain pulse into the bulk at the speed of sound $v_s \approx 4700 \text{ m/s}$. The decrease of the satellite peak position relative to the Bragg angle with the time delay is due to the propagation of the strain pulse. As the pump-probe delay increases, i.e., as the strain pulse leaves the heated region, the magnitude of the expansion of the lattice decreases and consequently, X-ray photons are diffracted toward the Bragg peak corresponding to the unperturbed lattice planes. However, the lattice expansion will remain until the heat is transported away by thermal diffusion, and this occurs on *ns*-timescale (about 6 *ns*).

The phonons excited by *fs* laser pulses induce extra-time dependent periodicity to the lattice (see Appendix I) which subsequently causes oscillation in the diffracted signal observed at negative $\Delta\theta$. In other words, this can be explained as follows: in the absence of the coherent phonons, the Bragg condition is fulfilled if the difference of wave vectors of the incident and diffracted X-ray beams corresponds to a reciprocal lattice vector; on the other hand, in the presence of a phonon, when the diffraction intensity is measurable, the Bragg condition is fulfilled when the difference of the wave vectors equals the sum of reciprocal lattice vector and the *phonon wave vector* (see Appendix I). Thus, as the strain wave propagates in the crystal-different phonon modes are enhanced (i.e., they are driven to large amplitudes). The wave vectors of these phonon modes can be computed using the following relation (see Appendix I)

$$q = \Delta\theta |\mathbf{G}| \cot \theta_B \quad (7.15)$$

where \mathbf{G} is the reciprocal lattice vector[¶] and $\Delta\theta = \theta - \theta_B$. Near the Brillouin zone

[¶]Note that, in solid state physics $|\mathbf{G}| = 2\pi/d$, where d is the unperturbed plane spacing, whereas in crystallography the factor 2π is omitted.

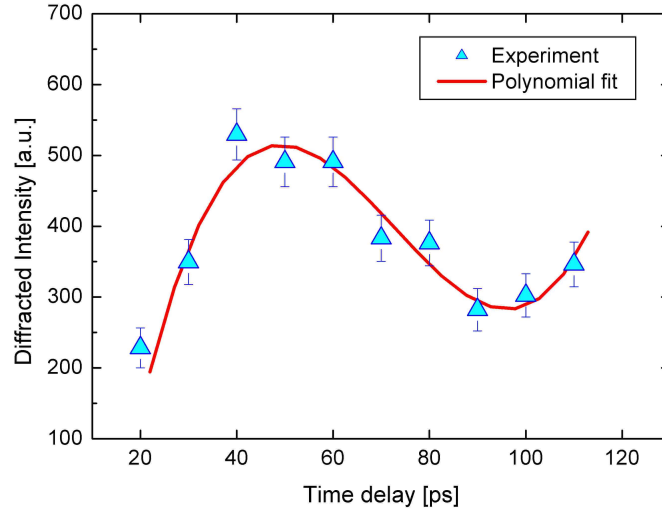


Figure 7.9: Time resolved diffracted intensity corresponding to a $|q| \approx 1.5 \times 10^7 \text{ m}^{-1}$.

center, the acoustic branch can be approximated by the linear dispersion relation

$$\omega \approx v_s q \quad (7.16)$$

Thus, according to Eq.(7.15), as the glancing angle θ is varied, different phonon-modes are selected out, and their frequency can be calculated using Eq.(7.16). Figure 7.9 shows the diffracted intensity at an angle $\Delta\theta \approx -470 \text{ arcsec}$, corresponding to the phonon wave vector $|q| \approx 1.5 \times 10^7 \text{ m}^{-1}$. The diffracted intensity shows oscillation with period of about $(82 \pm 4) \text{ ps}$, which is close to that predicted by Eq.(7.16), amounting about 90 ps.

The influence of a strain pulse on the rocking curve can be modelled by using the dynamical diffraction theory (Authier, 2001; Uschmann, 2004) in the presence of the strain (Thomsen *et al.*, 1986). The wave equation describing the x-ray propagation in a deformed lattice, formulated by Takagi-Taupin theory, is solved for the one dimensional case of a strain gradient (Taupin, 1964; Takagi, 1969). The depth dependent strain profile for a given time is taken into account by corresponding shift in the Bragg angle (due to the corresponding change in d -spacing), i.e., when the strain pulse is launched into a crystal, the interatomic distances change, and the corresponding shift in diffraction angle (for monochromatic radiation) is given by a differentiation of the Bragg's law

$$\eta = \frac{\Delta d}{d} = -\cot \theta_B \Delta\theta \quad (7.17)$$

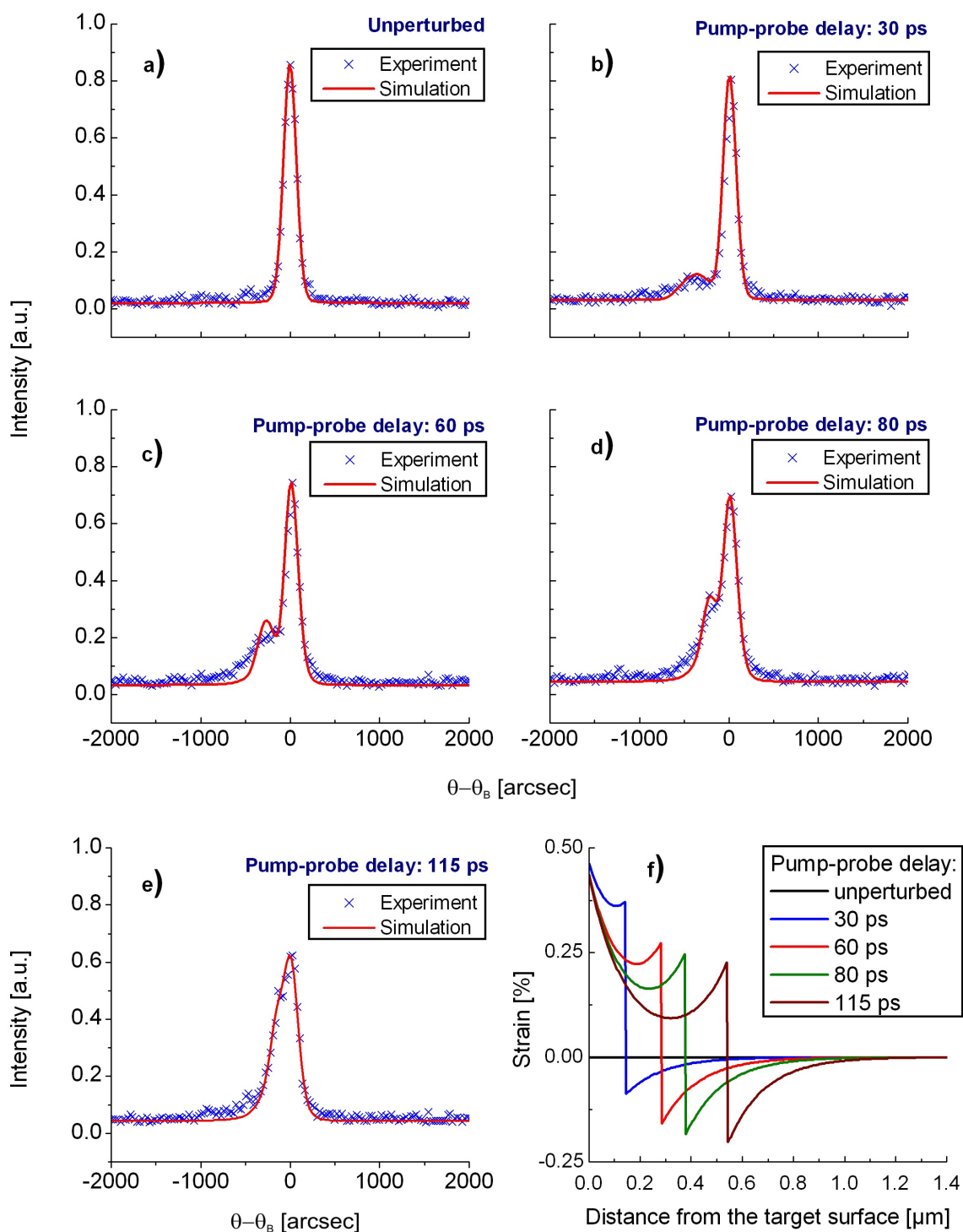


Figure 7.10: Time resolved rocking curves of impulsively strained SmS (sub-figures a to e) and their corresponding strains (sub-figure f). Laser fluence: 10 mJ/cm².

To account for instrumental broadening, the calculated rocking curves in the presence of the strain were convolved with Gaussian function of 133 arcsec FWHM. The comparison of measured rocking curves, shown in Figure 7.6, with those simulated by the above mentioned model are shown in Figure 7.10. It is evident that the simulations shown in Figure 7.10 reproduce well the features of the experimental data; the discrepancies at the wings of the rocking curves may be attributed to the underestimation of the carrier-lattice thermalization by the used model and errors introduced in evaluation of the rocking curves as well. The overall agreement of the measured and simulated rocking curves suggest that, the propagation of coherent acoustic phonons in semiconducting SmS is observed, and this demonstrates observation of the atomic motion in bulk media during picosecond time scale. Since the approach used to interpret the experimental results does not take into account any interplay between lattice vibrations and valence fluctuations, we can conclude that, at the laser fluences used, SmS behaves like a standard semiconductor (Krasniqi *et al.*, 2005b).

The maximum surface (elongation) strain is about 0.5%, or about 30 mÅ of lattice expansion, while the maximum compressive strain is about 0.2% or about 12 mÅ of lattice compression. For a crystalline semiconductor, the band gap E_g depends on the lattice constant a and changes by

$$\Delta E_g \approx \Phi \left(\frac{\Delta a}{a} \right) \quad (7.18)$$

when a phonon alters the lattice for Δa (Shockley and Bardeen, 1950). Φ is the deformation potential^{||} (for SmS, it is listed in Appendix F). Thus, the lattice contraction of 12 mÅ by the acoustic phonons causes an energy gap (band gap) decrease of about 0.009 eV, which indeed is not enough for the semiconductor-metal phase transition to occur. The occurrence of the phase transition requires driving of energy gap to zero (or at least to 0.065-0.067 eV) i.e., it requires an energy gap change (decrease) of about 0.2 eV. Moreover, the compression stress induced by the acoustic phonons^{**} is about

^{||}The deformation potential results from the change of the force exerted on carriers by the lattice, due to phonons. It can be determined by shifts in energy bands with dilatations.

^{**}The stress σ induced by the acoustic phonons (considering only deformations parallel to the shock front) can be calculated by using the following expression (Gersten and Smith, 2001):

$$\sigma = \frac{(C_{11} - C_{12})(C_{11} + 2C_{12})}{C_{11} + C_{12}} \eta \quad (7.19)$$

where η is the strain, C_{11} and C_{12} are elastic constants; for SmS, they are listed in Appendix F.

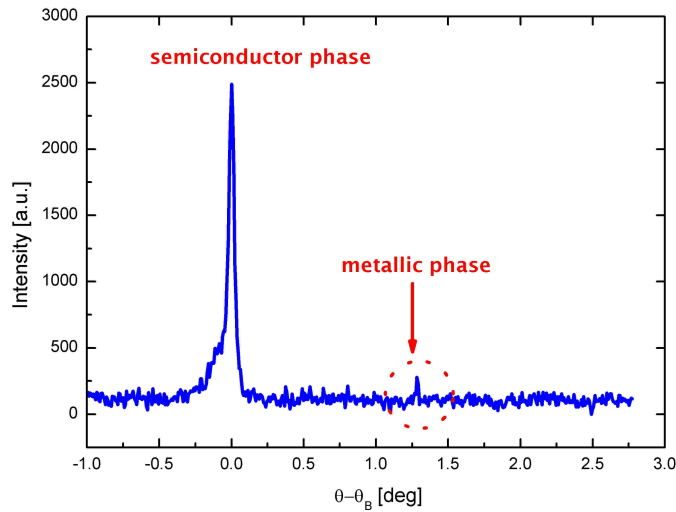


Figure 7.11: The rocking curve measured at a pump-probe delay of 50 ps and laser fluence of about $12\text{mJ}/\text{cm}^2$. A small peak (marked with dashed circle), located at about 1.3° relative to the Bragg peak is observed. This peak is attributed to the metallic phase of SmS.

0.25 GPa, and that needed for the phase transition is about 0.65-0.67 GPa. Thus at this laser fluence, no phase transition has occurred, and SmS behaves as a standard semiconductor.

At the laser fluence of about $12\text{mJ}/\text{cm}^2$, in the rocking curve measured at a pump-probe delay of 50 ps, at angular position of about 1.3° relative to the Bragg peak, a small peak is observed. The standard deviation of the intensity at the position of the peak is about 9% of the peak intensity, and the background intensity fluctuations are up to about 50% of the peak intensity. This peak is located in the position where the metallic phase signal should appear, that is, since the lattice constant of SmS at pressures higher than 0.65 GPa is smaller than 5.77 \AA , the angular position of the metallic phase relative to the semiconductor phase peak should be larger than 1° . According to [Jayaraman *et al.* \(1975\)](#) (see also Section 6.2), the mixed valence can be viewed as a state where the Sm ion in the SmS crystal fluctuates in time between $4f^6$ and $4f^55d^1$ configurations; when the fluctuation rate is very high, the lattice is not able to follow fully the electronic state and the Sm ion *stabilizes* at some *intermediate* size. Thus, observation of the metallic phase 50 ps after the perturbation of the crystal with the pump pulses suggest that, any fluctuation between the $4f^6$ and $4f^55d^1$ configurations is faster than 10^{-11} s , otherwise the peak would have been appeared at $\Delta\theta \approx 1.87^\circ$, or not at all. Therefore, the upper limit of the valence fluctuation time is shorter than that suggested by [Coey *et al.* \(1976\)](#),

which is $\lesssim 10^{-9}$ s. At the pump-fluence above 12 mJ/cm^2 , a permanent decrease of the measured signal is observed (about a factor of 3), which indicates permanent damage of the used crystalline region at this fluence.

7.5 Summary and Conclusions

In this Chapter, quantitative investigations of atomic motions in semiconducting SmS using optical pumping and X-ray probing, are reported. At the laser fluence of about 10 mJ/cm^2 , coherent acoustic phonon propagation in semiconducting SmS is observed. The observed acoustic phonons have frequencies up to about 0.08 THz. The time resolved diffraction data are in good agreement with theoretical predictions for coherent phonon excitation, demonstrating that, up to this laser fluence SmS behaves as a *standard semiconductor*, i.e., a semiconductor which (at the laser fluences used) shows no interplay between valence fluctuations and lattice vibrations. The measured structural changes indicate that, up to 12 mJ/cm^2 , the energy gap-closing necessary to drive semiconductor-metal phase transition in SmS, was not reached. At lower laser fluences (i.e., 3, 6 and 8 mJ/cm^2), we could not observe any feature in rocking curves which would suggest any lattice dynamics.

At the laser fluence of about 12 mJ/cm^2 , in the time scale of about 10^{-11} s, a signal corresponding to the metallic phase is observed; this may suggest that the interconfigurational fluctuation time is shorter than 10^{-11} s.

At the laser fluences above 12 mJ/cm^2 , a permanent decrease of the measured signal is observed (about a factor of 3), which indicates permanent damage of the used crystalline region at this fluence.

Chapter 8

Summary and Conclusions

The objective of the first part of the thesis was to investigate the influence of the intermediately coupled plasma environment on the radiating H-like Al ions by using high-resolution, high dispersion vertical geometry Johann spectrometer. Benefiting from the high spectral and spatial resolution of the spectrometer as well as from optimized sandwich-target geometry, the influence of the ionization potential lowering and the influence of electron-plasma waves in the emission spectra are observed. These results have both practical and theoretical importance. Practical, because some signatures observed in the emission spectrum lead to a new density diagnostic, and, theoretical, because they can be used to test different theoretical formulations of radiator-plasma interactions.

The experiments were carried out on the nanosecond Nd-glass laser facility at the LULI, Ecole Polytechnique, Palaiseau (France). A single laser beam delivering up to 20 J of the frequency-quadrupled radiation ($0.263 \mu\text{m}$) in a pulse length of 0.5 ns was focused to a spot with a diameter of 80-100 μm , yielding intensity of the order of 10^{14} Wcm^{-2} . The radiation was incident onto a structured targets consisting of Al foils (with thicknesses ranging from 5-50 μm) sandwiched between two CH or Mg foils (each with thickness ranging from 5-25 μm). Close to the irradiated target surface, electron density and temperature can reach extreme values to about 10^{23} cm^{-3} and 300 eV, respectively, whereas at about 100 μm from the target surface to about 10^{21} cm^{-3} and 900 eV, respectively.

The increased broadening and red shift of Al Lyman lines (γ and δ) with increasing electron density is observed. The measured Al Ly γ red shifts compare well with the quantum mechanical impact theory (QMIT) and uniform-electron-gas ion sphere

model (UEG-ISM). The Al Ly ζ - θ lines show gradual merging into continuum with increasing electron density. Comparison of the measured Al Ly δ line widths with simulated ones, predict that the electron densities where Al Ly ζ and η merge into continuum are about $1.5 \times 10^{22} \text{ cm}^{-3}$ and $8 \times 10^{21} \text{ cm}^{-3}$, respectively. The observed merging of Ly ζ and η into continuum is interplay of ionization potential lowering and spectral line broadening.

Detailed experimental studies of Ly γ line profiles emitted from dense Al plasma revealed fine structures on the red wing. These structures can plausibly be identified as the electron-plasma-wave caused dips (*L-dips*). Since their position from the line center depend on the electron density, they are used as a density diagnostic. This is the first application of the L-dips to diagnose hot and dense plasmas with electron densities $N_e > 1 \times 10^{21} \text{ cm}^{-3}$. The results obtained confirm that, it is possible to use L-dips as a density diagnostics in intermediately coupled plasmas, thus suggesting a possibility to develop a new efficient tool for plasma diagnostics.

Experimental profiles of Al Ly γ emitted from laser irradiated Al_4C_3 targets are more structured than those measured at Al targets. In this case, Al^{12+} radiators are perturbed mostly by the ions C^{6+} , therefore regardless of L-dips, the charge exchange results in a different kind of dips, called *X-dips*. In this work it is demonstrated that these dips are not observed at Al targets where the radiating and perturbing ions have the same nuclear charge.

At Al irradiated foils, where plasma is not laterally constrained, the Al Ly β line profiles show asymmetry in the red side, whereas Al Ly γ line profiles show asymmetry in the blue side. The asymmetry increases with increasing distance from the target surface, i.e., with decreasing of plasma density. At Al sandwich-targets, where the plasma is laterally constrained (and the plasma gradients are suppressed), the asymmetry in Al Ly β and γ line profiles is very weak. Thus, it is found that the asymmetry is related with the spatial constraint of the plasma. In laterally unconstrained plasmas, the radiating ions experience electric- and velocity- field inhomogeneities which lead to observed asymmetries.

The second part of the thesis reports about the time resolved experiments designed to examine the time resolved response of the semiconducting SmS crystal. At atmospheric pressure, SmS is a black-colored ionic semiconductor of NaCl-type structure

with a lattice constant of 5.97 Å, whereas at a pressure of about 0.65 GPa, it undergoes a first order phase transition to the metallic state which has a golden color. Under pressure there is a monotonic decrease of the lattice constant to 5.7 Å at 0.65 GPa. The phase transition is isostructural (i.e., NaCl-structure is retained) and involves delocalization of a 4*f* electron from the Sm ion ($4f^6 \rightarrow 4f^5 5d^1$) as the valence state changes from 2+ toward 3+. Fluctuating valence in Sm ion directly causes fluctuation in the ionic diameter, which consequently may induce lattice distortion around the Sm ion; thus, time resolved investigation of structural changes in SmS contribute to understanding the time resolved response of SmS crystal, provide insights into the phase transition as well as in electron-phonon coupling.

The experiments were performed with a CPA Ti:Sapphire laser facility at IOQ in Jena, delivering 80 fs pulses at a wavelength of about 800 nm with a maximum energy of 200 mJ and a repetition rate of 10 Hz. 90% of the laser pulse is focused onto a Ti band target to produce Ti $K\alpha$ pulses. The remaining 10% of the laser pulse was used to initiate structural changes in semiconducting SmS, which then are probed by Ti $K\alpha$ pulses.

At the laser fluence of about 10 mJ/cm², coherent acoustic phonon propagation is observed. The observed acoustic phonons have frequencies up to about 0.08 THz. The measured structural changes indicate that up to 12 mJ/cm², the energy-gap-closing necessary to drive semiconductor-metal phase transition was not reached. Comparison of the time resolved diffraction data with theoretical predictions for coherent phonon excitation demonstrate that, up to laser fluence of about 10 mJ/cm², SmS behaves as a standard semiconductor.

At the laser fluence of about 12 mJ/cm², in the pump-probe delay time scale of about 10⁻¹¹ s, a signal corresponding to the metallic phase is observed; this may suggest that the interconfigurational fluctuation time is shorter than 10⁻¹¹ s. At the laser fluences higher than 12 mJ/cm², a permanent decrease of the measured signal is observed, which indicates permanent damage of the used crystalline region.

Additionally, semiconductor-metal phase transition is induced by polishing the SmS crystal whereas metal-semiconductor phase transition is induced by heating the crystal to about 150°C. The measured lattice constant of the metallic phase revealed an intermediate valence of about 2.8.

Zusammenfassung

Thema des ersten Teils der Thesen war die Untersuchung des Einflusses der Plasmaumgebung (mit einer Kopplungskonstante von 0,1 bis 1) auf die strahlenden H-ähnlichen Al-Ionen durch Verwendung eines hochauflösenden, lichtstarken Johann-Spektrometers in vertikaler Dispersionsgeometrie. Es wurde der Einfluss beobachtet, den ein Absenken des Ionisationspotentials und die Elektronenplasmawellen im Emissionsspektrum, unterstützt sowohl durch die hohe spektrale und räumliche Auflösung als auch durch die optimierte Sandwich-Target Geometrie, haben. Die Ergebnisse haben sowohl praktische als auch theoretische Bedeutung. Praktische, weil einige Signaturen, die im Emissionsspektrums beobachtet wurden, zu einer neuen Dichtebestimmung führten. Theoretische, weil sie verwendet werden können, um verschiedene theoretische Formulierungen von Ionen-Plasma-Wechselwirkungen zu testen.

Die Experimente wurden am Nanosekunden Nd-Glas Lasersystem am LULI, Ecole Polytechnique, Palaiseau (Frankreich), durchgeführt. Ein einzelner Laserstrahl, der bis zu 20 J der Frequenz gekoppelter Strahlung ($\lambda = 0,263 \mu\text{m}$) bei einer Pulsdauer von 0,5 ns liefert, wurde auf einen Spot mit einem Durchmesser von 80-100 μm fokussiert. Dabei erhält man eine Intensität in der Größenordnung von 10^{14} W/cm^2 . Die Strahlung fiel auf ein strukturiertes Target aus Al Folie (mit einer Dicke von 5 bis 50 μm) ein, eingeschoben zwischen zwei CH oder Mg Folien (jede mit einer Dicke von 5 bis 25 μm). In der Nähe der bestrahlten Targetoberfläche können die Elektronendichte und die Temperatur extreme Ausmaße bis zu 10^{23} cm^{-3} bzw. 300 eV annehmen, währenddessen sie 100 μm entfernt von der Targetoberfläche nur noch 10^{21} cm^{-3} bzw. 900 eV betragen.

Es wurde eine Zunahme der Verbreiterung und eine Rot-Verschiebung einiger Al Lyman Linien (Ly γ und δ) beobachtet. Die gemessene Verschiebung von Al Ly γ stimmt gut mit vorhanden Theorien überein. Wenn die Elektronendichte zunimmt, gehen die Al Ly $\zeta - \theta$ graduell im Kontinuum auf. Der Vergleich von gemessener

Al Ly δ Linienbreite mit der simulierten sagt voraus, dass die Elektronendichte, bei der die Al Ly ζ und η ins Kontinuum übergegangen sind, eine Größenordnung von $1,5 \times 10^{22}$ bzw. $8 \times 10^{21} \text{ cm}^{-3}$ haben. Der beobachtete Effekt ist ein Zusammenspiel von Linienverbreiterung und Absenken des Ionisationspotentials.

Detaillierte experimentelle Untersuchungen der Profile von Ly Linien, die von einem heißen und dichten Al Plasma emittiert wurden, zeigen Feinstrukturen auf der langwelligen Seite der Linie. Diese Strukturen konnten eindeutig als Einsattelungen (*L-dips*) identifiziert werden, die durch Elektronen-Plasma-Wellen hervorgerufen wurden. Weil ihr Abstand vom Linienzentrum von der Elektronendichte abhängt, werden die L-dips zur Elektronendichtebestimmung angewandt. Diese Arbeit ist die erste Anwendung von L-dips zur Elektronendichtebestimmung von heißen und dichten Plasmen mit einer Elektronendichte $N_e > 10^{21} \text{ cm}^{-3}$. Die Ergebnisse bestätigen, dass es möglich ist, die L-dips als Mittel zur Elektronendichtebestimmung in heißen und dichten Plasmen zu nutzen, daraus ergibt sich die Möglichkeit für die Entwicklung einer neuen effizienten Methode zur Plasmadiagnostik.

Die gemessenen Profile von Al Ly γ , die von einem laserbestrahlten Al_4C_3 Target emittiert wurden, sind stärker strukturiert als die emittierten von Al Targets. In diesem Fall sind die Al^{12+} Strahler hauptsächlich durch C^{6+} Ionen gestört, deshalb ergibt der Ladungstausch ohne Berücksichtigung von L-dips, eine neue Art von dips, so genannten *X-dips*. In dieser Arbeit wurde gezeigt, dass diese dips (X-dips) in Al Targets, die strahlende und störende Ionen mit gleicher Kernladung enthalten, nicht beobachtet werden.

Bei Laser bestrahlten Al Folien, bei denen das Plasma nicht seitlich eingeschränkt ist, zeigt das Al Ly β Linienprofil eine Asymmetrie auf der langwelligen Seite der Linie, während das Al Ly γ Linienprofil eine Asymmetrie auf der kurzwelligen Seite zeigt. Die Asymmetrie nimmt zu, wenn der Abstand von der Targetoberfläche größer wird, d.h. mit Abnahme der Plasmadichte. Bei Al-Sandwich Targets, wo das Plasma ist seitlich eingeschränkt (und der Plasmagradiant unterdrückt wird), ist die Asymmetrie sehr schwach. Demnach steht die Asymmetrie in Zusammenhang mit der seitlichen Einschränkung des Plasmas. In seitlichen nicht eingeschränkten Plasmen, erfahren die strahlenden Ionen die elektrischen- und Geschwindigkeits-Feld Gradienten, die zu den beobachteten Asymmetrien führten.

Der zweite Teil der Arbeit befasst sich mit zeitaufgelösten Experimenten, die mit dem Ziel entwickelt wurden, ein zeitaufgelöstes Signal eines halbleitenden SmS-Kristalls zu untersuchen. Unter atmosphärischem Druck ist SmS ein schwarz aussehender Halbleiter mit NaCl-Struktur und einer Gitterkonstanten von $5,97 \text{ \AA}$. Bei einem Druck von $0,65 \text{ GPa}$ vollzieht sich im SmS ein Phasenübergang erster Ordnung zu der metallischen Phase, die eine goldene Farbe hat. Der Phasenübergang ist isostrukturell (d.h. die NaCl-Struktur bleibt erhalten) und wird durch die Ablösung eines $4f$ -Elektrons von dem Sm-Ion (Sm^{2+}) verursacht, so dass sich die Ionisationsstufe von $2+$ zu $3+$ ändert. Der veränderte Valenzzustand verursacht direkt eine Veränderung des Ionenradius, woraus Gitterstörungen um das SmS-Ion entstehen. Zeitaufgelöste Untersuchungen der Strukturänderungen in SmS sind folglich ein wertvolles Hilfsmittel, um Einblicke sowohl in den Phasenübergang als auch in die Elektronen-Photonen-Wechselwirkung zu erlangen.

Die Experimente wurden mit einem CPA Ti:Saphir-Laser, der 80 fs -Laserpulse bei einer Wellenlänge von etwa 800 nm , einer Maximalenergie von 200 mJ und einer Wiederholrate von 10 Hz liefert, am IOQ in Jena durchgeführt. 90% der Laserpulse werden zur Erzeugung von Ti $K\alpha$ -Pulsen auf ein Ti-Bandtarget fokussiert. Die restlichen 10% der Laserpulse wurden zur Initialisierung der Strukturänderungen im halbleitenden SmS genutzt, die dann durch die Ti $K\alpha$ -Pulse untersucht werden.

Bei einer Laserfluenz von etwa 10 mJ/cm^2 wird die Ausbreitung von kohärenten akustischen Phononen beobachtet. Die beobachteten akustischen Phononen haben Frequenzen bis zu etwa $0,08 \text{ THz}$. Die gemessenen Strukturänderungen zeigen, dass bis zu 12 mJ/cm^2 das Schließen der Energielücke als notwendige Voraussetzung für den Halbleiter-Metall-Phasenübergang nicht erreicht wurde. Ein Vergleich der zeitaufgelösten Beugungsdaten mit theoretischen Vorhersagen für kohärente Phononenanregung zeigt, dass sich SmS bis zu einer Laserfluenz von etwa 10 mJ/cm^2 wie ein Standard-Halbleiter verhält.

Bei der Laserfluenz von etwa 12 mJ/cm^2 wurde in der pump-probe Verzögerungszeitskala von etwa 10^{-11} s ein Signal, das mit der metallischen Phase übereinstimmt, beobachtet. Daraus lässt sich vermuten, dass die zwischenstrukturelle-Fluktuations-Zeit kleiner als 10^{-11} s ist. Bei einer größeren Laserfluenz als 12 mJ/cm^2 wird ein stetiger Abfall des gemessenen Signals beobachtet, was auf eine Zerstörung des genutzten kristallinen

Gebiets hinweist.

Zusätzlich wird durch einen polierten SmS Kristall ein Phasenübergang vom Halbleiter zum Metall hervorgerufen wird, während der Metall-Halbleiter Phasenübergang induziert wird, indem der Kristall auf 150°C erhitzt wird. Die gemessene Gitterkonstante der Metallphase zeigt eine Zwischen-Valenz von 2,8.

Bibliography

- Atwood D., *Soft X-Rays and Extreme Ultraviolet Radiation*, Cambridge University Press, Cambridge (1999).
- Audebert P., Shepherd R., Fournier K. B., Peyrusse O., Price D., Lee R. W., Springer P., Gauthier J.-C. and Klein L., *Time-Resolved Plasma Spectroscopy of Thin Foils Heated by a Relativistic-Intensity Short-Pulse Laser*, Phys. Rev. E **66**, 066412 (2002).
- Authier A., *Dynamical Theory of X-Ray Diffraction*, Oxford University Press, Oxford (2001).
- Bastiani S., Rouse A., Geindre J. P., Audebert P., Quoi C., Hamoniaux G., Antonetti A., and Gauthier J. -C., *Experimental study of the interaction of subpicosecond laser pulses with solid targets of varying initial scale lengths*, Phys. Rev. E **56**, 7179 (1997).
- Batlogg B., Kaldis E., Schlegel A. and Wachter P., *Electronic Structure of Sm Monochalcogenides*, Phys. Rev. B **14**, 5503 (1976).
- Bell A. R., *Laser Produced Plasmas*, in: Plasma Physics: An Introductory Course, R. Dendy (ed), Cambridge University Press, Cambridge, pp. 319 (1993).
- Bertin E. P., *Principles and Practice of X-Ray Spectrometric Analysis*, Plenum Press, New York, pp.193 (1975).
- Bethe, H. A., Salpeter, E. E., *Quantum Mechanics of One-and Two-Electron Atoms*, Plenum/Roseta (1977).
- Birgeneau R. J., Bucher E., Rupp L. W., and Walsh W. M., *Exchange Interactions in the Samarium Monochalcogenides*, Phys. Rev. B **5**, 3412 (1972).
- Böddeker St., Günter S., Könies A., Hitzschke L. and Kunze H. -J., *Shift and Width of the H_{α} Line of Hydrogen in Dense Plasmas*, Phys. Rev. E **47**, 2785 (1993).

- Böddeker St., Kunze H. -J. and Oks E., *Novel Structure in the H_{α} -Line Profile of Hydrogen in a Dense Helium Plasma*, Phys. Rev. Lett. **75**, 4740 (1995).
- Bransden B. H. and McDowell M. R. C., *Charge Exchange and the Theory of Ion-Atom Collisions*, Clarendon Press, Oxford (1992).
- Brueckner K. A. and Jorna S., *Laser-Driven Fusion*, Rev. Mod. Phys. **46**, 325 (1974).
- Bryant D. A. and Bingham R., *Space Plasma Physics*, in: Plasma Physics: An Introductory Course, R. Dendy (ed), Cambridge University Press, Cambridge, pp. 209 (1993).
- Calisti A., Khelifaoui F., Stamm R. and Talin B., *Model for the Line Shapes of Complex Ions in Hot and Dense Plasmas*, Phys. Rev. A **42**, 5433 (1990).
- Callan J. P., *Ultrafast Dynamics and Phase Changes in Solids Excited by Femtosecond Laser Pulses*, PhD Thesis, Harvard Univ., Cambridge (2000).
- Callister W. D., *Fundamentals of Materials Science and Engineering*, John Wiley & Sons, New York (2001).
- Chatterjee A., Singh A. K. and Jayaraman A., *Pressure-Induced Electronic Collapse and Structural Changes in Rare-Earth Monochalcogenides*, Phys. Rev. B **6**, 2285 (1972).
- Chin A. H., Schoenlein R. W., Glover T. E., Balling P., Leemans W. P. and Shank C. V., *Ultrafast Structural Dynamics in InSb Probed by Time-Resolved X-Ray Diffraction*, Phys. Rev. Lett. **83**, 336 (1999).
- Coey J. M. D., Ghatak S. K., Avignon M. and Holtzberg F., *Electronic Configuration of Samarium Sulphide and Related Compounds: Mössbauer-Effect Measurements and a Model*, Phys. Rev. B **14**, 3744 (1976).
- Cook A. H., *Interiors of the Planets*, Cambridge University Press, Cambridge (1981).
- Cooper J., *Plasma Spectroscopy*, Rep. Prog. Phys. **29**, 35 (1966).
- Christiansen J. P., Ashby D. E. and Roberts K. V., *MEDUSA-A One Dimensional Laser Fusion Code*, Comput. Phys. Commun. **7**, 271 (1974).
- Darwin C. G., *The Theory of X-Ray Reflection*, Phil. Mag. **27**, 315 (1914).

- Dendy R. (ed.), *Plasma Physics: An Introductory Course*, Cambridge University Press, Cambridge (1993).
- Denton A. R. and Ashcroft N. W., *Vegard's Law*, Phys. Rev. A **43**, 3161 (1991).
- Djaoui A. and Rose S. J., *Calculation of the Time-Dependent Excitation and Ionization in a Laser-Produced Plasmas*, J. Phys. B **25**, 2745 (1992).
- Duston D., Rogerson J. E., Davis J. and Blaha M., *Dense Plasma Effects on K-Shell Dielectronic Satellites Lines*, Phys. Rev. A **28**, 2968 (1983).
- Finken K. H., Buchwald R., Bertschinger G. and Kunze H. -J., *Investigation of the H Alpha Line in Dense Plasmas*, Phys. Rev. A **21**, 200 (1980).
- Fowler T. Kenneth, *Nuclear Power Fusion*, Rev. Mod. Phys. **71**, S456 (1999).
- Foreman L., *The Technology of the Target Fabrication for ICF*, in: Hooper M. B. (ed.), *Laser Plasma Interactions 5: Internal Confinement Fusion*, Scottish Universities Summer School in Physics & Institute of Physics Publishing, Bristol and Philadelphia, pp. 219 (1995).
- Förster E., Gäbel K. and Uschmann I., *New Crystal Spectrograph Designs and their Application to Plasma Diagnostics*, Rev. Sci. Instrum. **63**, 5012 (1992).
- Fraenkel B. S., *Highly Resolved, Monochromatic, X-Ray Images of Laser-Produced Plasmas through the Single-Crystal Double-Reflection Spectrometer*, Appl. Phys. Lett. **41**, 234 (1982).
- Gauthier P., Rose S. J., Sauvan P., Angelo P., Leboucher-Dalimier E., Calisti A. and Talin B., *Modeling the Radiative Properties of Dense Plasmas*, Phys. Rev. E **58**, 942 (1998).
- Gavrilenko V. P. and E. Oks, Sov. Phys. JETP **53**, 1122 (1981).
- Gavrilenko V. P. and Oks E., Sov. Phys. Plasma Phys. **13**, 22 (1987).
- Gershtein S. S. and Krivchenkov V. D., Sov. Phys.-JETP **13**, 1044 (1961).
- Gersten J. I. and Smith F. W., *The Physics and Chemistry of Materials*, Wiley, New York (2001).

- Ghatak S. K. and Bennemann K. H., *Effect of Valence Fluctuations on Lattice Vibrations*, J. Phys. F **8**, 571 (1978).
- Golubkov A. V., Kazanin M. M., Kaminskiĭ V. V., Sokolov V. V., Solov'ev S. M. and Trushnikova L. N., *Thermoelectric Properties of SmS_x (x=0.8-1.5)*, Inorganic Materials **39**, 1251 (2003).
- Griem H. R., *Plasma Spectroscopy*, McGraw-Hill, New York (1964).
- Griem H. R., *Spectral Line Broadening by Plasmas*, Academic Press, New York (1974).
- Griem H. R., Blaha M. and Kepple P. C., *Stark Profile Calculations for Lyman Series Lines of One-Electron Ions in Dense Plasmas*, Phys. Rev. A **19**, 2421 (1979).
- Griem H., *Shifts of Hydrogen and Ionized-Helium Lines from $\Delta n = 0$ interactions with Electrons in Dense Plasmas*, Phys. Rev. A **38**, 2943 (1988).
- Griem H. R., J. de Physique **49**, C1-293 (1988).
- Griem H. R., Blaha M. and Kepple P., *Stark-Profile Calculation for Resonance Lines of Heliumlike Argon in Dense Plasmas*, Phys. Rev. A **41**, 5600 (1990).
- Grützmacher K. and Wende B., *Stark Broadening of the Hydrogen Resonance Line L β in a Dense Equilibrium Plasma*, Phys. Rev. A **18**, 2140 (1978).
- Güntherodt G., Keller R., Grünberg P., Frea A., Kress W., Merlin R., Holzapfel W. B. and Holtzberg F., *Phase Diagram, Optical and Phononic Properties of the Valence Instability of SmS*, in R. Parks (ed.), *Valence Instabilities and Related Narrow Band Phenomena*, New York, Plenum Press, pp. 321 (1977).
- Güntherodt G., Merlin R., Frey A. and Cardona M., *Optic Phonon Anomalies and f-d Hybridization in SmS and SmB₆*, Solid State Commun. **27**, 551 (1978).
- Güntherodt G., Jayaraman A., Bilz H. and Kress W., *Electron-Phonon Coupling in Intermediate-Valence Compounds*, in L. M. Falicov, W. Hanke, M. B. Maple (eds.), *Valence Fluctuations in Solids*, North-Holland Publishing Company, New York, pp. 121 (1981).

- Hauer A., Mitchell K. B., van Hulsteyn D. B., Tan T. H., Linnebur E. J., Mueller M. M., Kepple P. C. and Griem H. R., *Spectroscopic Measurement of High-Density CO₂-Laser-Driven Implosion*, Phys. Rev. Lett. **45**, 1495 (1980).
- Hauer A. A., Kilkenny J. D. and Landen O. L., *Toroidally Curved Crystal for Time-Resolved X-Ray Spectroscopy*, Rev. Sci. Instrum. **56**, 803 (1984).
- Hauer A. A. and Baldis H. A., *Introduction to Laser Plasma Diagnostics*, in: Laser-Induced Plasmas and Applications, L. J. Radziemski and D. A. Cremers (eds.), Marcel Dekker, Inc., New York and Basel, pp. 105 (1989).
- Hauer A. A., Delamater N. D. and Koenig, Z. M., *High Resolution X-Ray Spectroscopic Diagnostics of Laser Heated and ICF Plasmas*, Laser and Particle Beams, **9**, 3 (1991).
- Haynes D. A., Jr., Garber D. T., Hooper C. F., Mancini R. C., Lee Y. T., Bradley D. K., Delettrez J., Epstein R. and Jaanimagi P. A., *Effects of Ion Dynamics and Opacity on Stark-Broadened Argon Line Profiles*, Phys. Rev. E **53**, 1042 (1996).
- Hawryluk R. J., *Results from Deuterium-Tritium Tokamak Confinement Experiments*, Rev. Mod. Phys. **70**, 537 (1998).
- He H., Wark J. S., Foerster E., Uschmann I., Renner O., Kopecky M. and Blyth W., *Double-Crystal High-Resolution X-Ray Spectroscopy of Laser-Produced Plasmas*, Rev. Sci. Instrum. **64**, 26 (1993).
- Helliwell J. R. and Rentzepis P. M., (eds.), *Time-Resolved Diffraction*, Clarendon Press, Oxford (1997).
- Henke B. L., Yamada H. T. and Tanaka T. J., *Pulsed Plasma Source Spectrometry in the 808000-eV X-Ray Region*, Rev. Sci. Instrum. **54**, pp. 1311 (1983).
- Hirlimann C., in: *Femtosecond Laser Pulses Principles and Experiments* (ed. Rullière, C.), Springer, Berlin, pp. 47 (1998).
- Hood A. W., *Solar Plasmas*, in: Plasma Physics: An Introductory Course, R. Dendy (ed), Cambridge University Press, Cambridge, pp. 267 (1993).

- Hooper C. F., Kilcrease D. P., Mancini R. C., Woltz L. A., Bradley D. K., Jaanimagi P. A. and Richardson M. C., *Time-Resolved Spectroscopic Measurements of High Density in Ar-Filled Microballoon Implosions*, Phys. Rev. Lett. **63**, 267 (1989).
- Hooper M. B. (ed.), *Laser Plasma Interactions 5: Internal Confinement Fusion*, Scottish Universities Summer School in Physics & Institute of Physics Publishing, Bristol and Philadelphia (1995).
- Ichimaru S., *Strongly Coupled Plasmas: High Density Classical Plasmas and Degenerate Electron Liquids*, Rev. Mod. Phys. **54**, 1017 (1982).
- Ichimaru S., *Nuclear Fusion in Dense Plasmas*, Rev. Mod. Phys. **65**, 255 (1993).
- Ichinose S. and Kuroda Y., *Lattice Vibration in Homogeneously-Mixed-Valent Systems of Rare-Earth Materials*, Phys. Rev. B **25**, 2550 (1982).
- Iglesias C. A., DeWitt H. E., Lebowitz J. L., MacGowan D. and Hubbard W. B., *Low-Frequency Electric Microfield Distributions in Plasmas*, Phys. Rev. A **31**, 1698 (1985).
- Jamelot G., Jaeglé P., Lemaire P. and Carillon A., *J. Quant. Spectrosc. Radiat. Transfer* **44**, 71 (1990).
- Jayaraman A., Narayanamurti V., Bucher E. and Maines R. G., *Continuous and Discontinuous Semiconductor-Metal Transition in Samarium Monochalcogenides Under Pressure*, Phys. Rev. Lett. **25**, 1430 (1970).
- Jayaraman A., Bucher E., Dernier P. D. and Longinotti L. D., *Temperature-Induced Explosive First-Order Electronic Phase Transition in Gd-Doped SmS*, Phys. Rev. Lett. **31**, 700 (1973).
- Jayaraman A., Singh A. K., Chatterjee A. and Usha Devi S., *Pressure-Volume Relationship and Pressure-Induced Electronic and Structural Transformations in Eu and Yb Monochalcogenides*, Phys. Rev. B **9**, 2513 (1974).
- Jayaraman A., Dernier P. and Longinotti L. D., *Study of the Valence Transition in SmS Induced by Alloying, Temperature, and Pressure*, Phys. Rev. B **11**, 2783 (1975).
- Joyce R., Woltz L. A. and Hooper C. F., *Asymmetry of Stark-Broadened Lyman Lines from Laser-Produced Plasmas*, Phys. Rev. A **35**, 2228 (1987).

- Junkel G. C., Gunderson M. A. and Hooper Jr. C. F., *Full Coulomb Calculation of Stark Broadened Spectra from Multi-Electron Ions: A Focus on the Dense Plasma Line Shift*, Phys. Rev. E **62**, 5584 (2000).
- Kahn S. M., Behar E., Kinkhabwala A. and Savin D., *X-Ray Spectroscopy of Astrophysical Plasmas*, Phil. Trans. R. Soc. Lond. A **360**, 1923 (2002).
- Kaldis E. and Wachter P., *The Semiconductor-Metal Transition of the Samarium Monochalcogenides*, Solid State Commun. **11**, 907 (1972).
- Kaminskii V.V., *Energy of the Metal-Semiconductor Phase Transition in SmS and the Threshold Recording Energy Density*, Sov. Phys. Solid State **20**, 1008 (1978).
- Kaminskii V. V. and Solov'ev S. M., *EMF Induced by a Change in the Samarium Ion Valence as a Result of a Phase Transition in SmS Single Crystals*, Physics of the Solid State **43**, 439 (2001).
- Kauffman R., *X-Ray Radiation from Laser Plasma*, in: Physics of Laser Plasma, A. Rubenchik and S. Witkowski (eds.), North-Holland, Amsterdam, pp. 111 (1991).
- Kelly L., *Kelly Atomic Line Database*, cfa-www.harvard.edu/amdata/ampdata/kelly/kelly.html (2003).
- Kilkenny J. D., Lee R. W., Key M. H. and Lunney J. G., *X-Ray Spectroscopic Diagnosis of Laser-Produced Plasmas with Emphasis on Line Broadening*, Phys. Rev. A **22**, 2746 (1980).
- Kirk J. L., Vedam K., Narayanamurti V., Jayaraman A. and Bucher E., *Direct Optical Observation of the Semiconductor-to-Metal Transition in SmS under Pressure*, Phys. Rev. B **6**, 3023 (1972).
- Kmetec J. D., Gordon C. L., Macklin J. J., Lemoff B. E., Brown G. S., and Harris S. E., *MeV X-Ray Generation with a Femtosecond Laser*, Phys. Rev. Lett. **68**, 1527 (1992).
- Koenig M., Malnault Ph. and Nguyen H., *Atomic Structure and Line Broadening of He-like Ions in Hot and Dense Plasmas*, Phys. Rev A **38**, 2089 (1988).
- Koshelev N., *Asymmetric Line Profiles of Highly Charged Ions in Dense Plasmas and Dielectric Satellites*, J. Phys. B: At. Mol. Opt. Phys. **21**, L593 (1988).

- Krasniqi F. S., Renner O., Dalimier E., Dufour E., Schott R. and Förster E., *Density Diagnostics of Intermediately Coupled Plasmas Based on Langmuir-Wave-Caused Dips*, Eur. Phys. J. D, submitted (2005).
- Krasniqi F. S., Uschmann I., Morak A., Kämpfer T., Förster E. and Sauerbrey R., *Ultrafast Structural Dynamics in Samarium mono-Sulphide (SmS) Probed by Time Resolved X-Ray Diffraction*, Europhys. Lett., submitted (2005).
- Kruer W. L., *Laser Plasma Interactions in Hohlräumen*, in: Hooper M. B. (ed.), *Laser Plasma Interactions 5: Internal Confinement Fusion*, Scottish Universities Summer School in Physics & Institute of Physics Publishing, Bristol and Philadelphia, pp. 27 (1995).
- Kuroda Y. and Bennemann K. H., *Coupling between Valence Fluctuations and Lattice Vibrations in Rare-Earth Chalcogenides*, Phys. Rev. B **23**, 4114 (1981).
- Kühne M. and Petzold H.-Ch., *Soft X-Ray Radiation from Laser-Produced Plasmas: Characterization of Radiation Emission and its Use in X-Ray Lithography*, Applied Optics **27**, 3926 (1988).
- Landolt-Börnstein, New Series-Group III, Vol. 41: Subvol. D, Springer Verlag (2001).
- Larson B. C., White C. W., Noggle T. S., Barhorst J. F. and Mills D. M., *Synchrotron X-Ray Diffraction Study of Silicon During Pulsed Laser Annealing*, Phys. Rev. Lett. **48**, 337 (1982).
- Leboucher-Dalimier E., Poquérousse A. and Angelo P., *Space-Resolved X-Ray Emission from the Densest Part of Laser Plasmas: Molecular Satellite Features and Asymmetrical Wings*, Phys. Rev. E **47**, R1467 (1993).
- Leboucher-Dalimier E., Oks E., Defour E., Sauvan P., Angelo P., Schott R. and Poquérousse A., *Experimental Discovery of Charge Exchange Caused Dips in Spectral Lines from Laser-Produced Plasmas*, Phys. Rev. E **64**, 065401 (2001).
- Leboucher-Dalimier E., Oks E., Defour E., Angelo P., Sauvan P., Schott R. and Poquérousse A., *Advanced Simulations of Spectroscopic Signatures of Charge Exchange in Laser-Produced Plasmas*, The European Physical Journal D **20**, 269 (2002).

- Lee R. W., *Study of the Plasma Broadening of Spectral Lines of Hydrogenic Ions*, J. Phys. B: At. Mol. Opt. Phys. **12**, 1129 (1979).
- Lee R. W., *Study of Ion Dynamic Effects on Lyman and Balmer Hydrogen Lines*, J. Phys. B: At. Mol. Opt. Phys. **12**, 1145 (1979).
- Lee R. W., *Fits for Hydrogenic Stark-Broadened Line Profiles for the Elements Carbon to Argon*, J. Appl. Phys. **58**, 612 (1985).
- Lee R. W., *Plasma Line Shapes for Selected Transitions in Hydrogen-, Helium- and Lithium-Like Ions*, J. Quant. Spectrosc. Radiat. Transfer **40**, 561 (1988).
- Lee R. W., *The How To: FLY, FLY User Manual* (1995).
- Lee R. W., Petrasso R. and Falcone R. W., *Science on High Energy Lasers: From Today to the NIF*, LLNL Report: UCRL-ID-119170 (1995).
- Lee R. W. and Larsen J. T., *A Time Dependent Model for Plasma Spectroscopy of K-shell Emitters*, J. Quant. Spectrosc. Radiat. Transfer **56**, 535 (1996).
- Lindenberg A. M., Kang I., Johnson S. L., Missalla T., Heimann P. A., Chang Z., Larsson J., Bucksbaum P. H., Kapteyn H. C., Padmore H. A., Lee R.W., Wark J. S. and Falcone R.W., *Time-Resolved X-Ray Diffraction from Coherent Phonons during a Laser-Induced Phase Transition*, Phys. Rev. Lett. **84**, 111 (2000).
- Lindl J., McCrory R. L. and Campbel E. M., *Progress Toward Ignition and Burn Propagation in Inertial Confinement Fusion*, Physics Today **45**, 32 (1992).
- Mandl F., *Quantum Mechanics*, John Wiley and Sons, Chichester (1992).
- Maple M. B. and Wohleben D., *Nonmagnetic 4f Shell in the High-Pressure Phase of SmS*, Phys. Rev. Lett. **27**, 511 (1971).
- Matthews D. L., Hagelstein P. L., Rosen M. D., Eckart M. J., Ceglio N. M., Hazi A. U., Medecky H., MacGowan B. J., Trebes J. E., Whitten B. L., Campbell E. M., Hatcher C. W., Hawryluk A. M., Kauffman R. L., Pleasance L. D., Rambach G., Scofield J. H., Stone G. and Weaver T. A., *Demonstration of a Soft X-Ray Amplifier*, Phys. Rev. Lett. **54**, 110 (1985).

- McCrory R. L. and Soures J. M., *Inertially Confined Fusion*, in: *Laser-Induced Plasmas and Applications*, L. J. Radziemski and D. A. Cremers (eds.), Marcel Dekker, Inc., New York and Basel, pp. 207 (1989).
- Misalla T., Uschmann I., Förster E., Jenke G. and von der Linde D., *Monochromatic Focusing of Subpicosecond X-Ray in the keV Range*, *Rev. Sci. Instrum.* **68**, 1288 (1999).
- Morak A., *Röntgenbeugung auf Subpikosekunden-Zeitskalen*, Dissertation, Friedrich-Schiller Universität, Jena (2003).
- More R. M., *Atomic Physics of Laser-Produced Plasmas*, in: *Physics of Laser Plasma*, A. Rubenchik and S. Witkowski (eds.), North-Holland, Amsterdam, pp. 63 (1991).
- Murillo M. S., Kilcrease D. P. and Collins L. A., *Dense Plasma Microfield Nonuniformity*, *Phys. Rev. E* **55**, 6289 (1997).
- Nishikawa K. and M. Wakatani, *Plasma Physics: basic Theory with Fusion Applications*, 2nd edition, Berlin Heidelberg, Springer-Verlag (1994).
- Nguyen H., Koenig M., Bendrejem D., Caby M. and Coulaud G., *Atomic Structure and Polarisation Line Shift in Dense and Hot Plasmas*, *Phys. Rev. A* **33**, 1279 (1986).
- Ogata S., *Monte Carlo Simulation Study of Crystallization in Rapidly Supercooled One-Component Plasmas*, *Phys. Rev. A* **45**, 1122 (1992).
- Oks E. and Rantsev-Kartinov V. A., *Sov. Phys. JETP* **52**, 50 (1980).
- Oks E., St. Bddeker and Kunze H.-J., *Spectroscopy of Atomic Hydrogen in Dense Plasmas in the Presence of Dynamic Fields: Intra-Stark Spectroscopy*, *Phys. Rev. A* **44**, 8338 (1991).
- Oks E., *Plasma Spectroscopy: The Influence of Microwave and Laser Fields*, New York, Springer Verlag (1995).
- Oks E., *Are Crossings of Energy Levels and Charge Exchange Really Quantum Phenomena?*, *Phys. Rev. Lett.* **85**, 2084 (2000).
- Oks E. and Leboucher-Dalimier E., *Spectroscopic Signatures of Avoided Crossings Caused by Charge Exchange in Plasmas*, *J. Phys. B* **33**, 3795 (2000).

- Oks E. and Leboucher-Dalimier E., *Extrema in Transition Energies Resulting not in Satellites but in Dips within Spectral Lines*, Phys. Rev. E **62**, R3067 (2000).
- Pagel B. E. J., *Importance of Spectral Line Shapes in Astrophysics*, J. Phys. B **4**, 279 (1971).
- Patel P. K., Wolfrum E., Renner O., Loveridge A., Allott R., Neely D., Rose S. J. and Wark J. S., *X-Ray Line Reabsorption in Rapidly Expanding Plasma*, J. Quant. Spectr. Radiat. Transfer **65**, 429 (2000).
- Paul P. M., Toma E. S., Breger P., Mullot G., Augé F., Balcou Ph., Muller H. G. and Agostini P., *Observation of a Train of Attosecond Pulses from High Harmonic Generation*, Science **292**, 1689 (2001).
- Perman B., Srajer V., Ren Zh., Teng T., Pradervand C., Ursby T., Bourgeois D., Schotte F., Wulff M., Kort R., Hellingwerf K. and Moffat K., *Energy Transduction on the Nanosecond Time Scale: Early Structural Events in a Xanthopsin Photocycle*, Science **279**, 1946 (1998).
- Pittman T. L. and Fleurier C., *Plasma Shifts of the He II H_{α} and P_{α} lines*, Phys. Rev. A **33**, 1291 (1986).
- Plech A., Wulff M., Bratos S., Mirloup F., Vuilleumier R., Schotte F. and Anfinrud P. A., *Visualizing Chemical Reactions in Solution by Picosecond X-Ray Diffraction*, Phys. Rev. Lett. **92**, 125505-1 (2004).
- Pohl D. W., Badertscher R., Müller K. A. and Wachter P., *Laser Induced Phase Transitions in the Surface of SmS Crystals*, Appl. Opt. **13**, 95 (1974).
- Potter E. D., Herek J. L., Pederson S., Liu Q. and Zewail A. H., *Femtosecond Laser Control of a Chemical Reaction*, Nature **355**, 66 (1992).
- Pronko P. P., S. K. Dutta, J. Squier, J. V. Rudd, D. Du and Mourou G., *Machining of Sub-Micron Holes Using a Femtosecond Laser at 800 nm*, Opt. Commun. **114**, 106 (1995).
- Reich Ch., Gibbon P., Uschmann I. and Förster E., *Yield Optimization and Time Structure of Femtosecond Laser Plasma $K \alpha$ Sources*, Phys. Rev. Lett. **84**, 4846 (2000).

- Renner O., Kopecky M., Krousky E., Förster E., Missalla T. and Wark J. S., *New Methods of X-ray Spectroscopy of Laser Produced Plasmas with One-Dimensional Spatial Resolution*, *Laser and Particle Beams* **12**, 539 (1994).
- Renner O., Kopecky M., Wark J. S., He H. and Förster E., *Vertical Dispersion Mode Double-Crystal Spectrometer for Advanced Spectroscopy of Laser-Produced Plasma*, *Rev. Sci. Instrum.* **66**, 3234 (1995).
- Renner O., Missalla T., Sondhauss P., Krousky E. and Förster E., *High-Luminosity, High-Resolution, X-Ray Spectroscopy of Laser-Produced Plasma by Vertical-Geometry Johann Spectrometer*, *Rev. Sci. Instrum.* **68**, 2393 (1997).
- Renner O., Sondhauss P., Salzmann D., Djaoui A., Koenig M. and Förster E., *Measurement of the Polarization Shifts in Hot and Dense Aluminum Plasma*, *J. Quant. Spectrosc. Radiat. Transfer* **58**, 851 (1997).
- Renner O., Sondhauss P., Salzmann D., Djaoui A., Koenig M. and Förster E., *Measurement of the Polarization Shifts in Hot and Dense Aluminum Plasma*, *J. Quant. Spectrosc. Radiat. Transfer* **58**, 851 (1997).
- Renner O., Salzmann D., Sondhauss P., Djaoui A., Krousky E. and Förster E., *Experimental Evidence for Plasma Shifts in Lyman Series of Aluminum*, *J. Phys. B* **31**, 1379 (1998).
- Renner O., Sondhauss P., Peyrusse O., Krousky E., Ramis R., Eidmann K. and Förster E., *High-Resolution Measurements of X-Ray Emission from Dense Quasi-1D Plasma: Line Merging and Profile Modification*, *Laser and Particle Beams* **17**, 365 (1999).
- Renner O., Limpouch J., Krousky E., Uschmann I. and Förster E., *Spectroscopic Characterization of Plasma Densities of Laser-Irradiated Al Foils*, *J. Quant. Spectrosc. Radiat. Transfer* **81**, 385 (2003).
- Renner O., Uschmann I. and Förster E., *Diagnostic Potential of Advanced X-Ray Spectroscopy for Investigation of Hot Dense Plasmas*, *Laser and Particle Beam* **22**, 25 (2004).
- Renner O., *Private Communications*, November (2004).
- Renner O., Dalimier E., Oks E., Krasniqi F., Dufour E., Schott R. and Förster E., *Experimental Evidence of Langmuir-Wave-Caused Dips in Spectral Lines of Laser-Produced Plasmas*, *J. Quant. Spectrosc. Radiat. Transfer*, accepted.

- Renner O., *Private Communications*, Januar (2005).
- Ribe F. L., *Fusion Reactor Systems*, Rev. Mod. Phys. **47**, 7 (1975).
- Rischel C., Rouse A., Uschmann I., Albouy P. -A., Geindre J. -P., Audebert P., Gauthier J. -C., Förster E., Martin J. -L. and Antonetti A., *Femtosecond Time-Resolved X-ray Diffraction from Laser-Heated Organic Films*, Nature **390**, 490 (1997).
- Root R. G., *Modeling of Post-Breakdown Phenomena*, in: Laser-Induced Plasmas and Applications, L. J. Radziemski and D. A. Cremers (eds.), Marcel Dekker, Inc., New York and Basel, pp. 69 (1989).
- Rose-Petruck C., Jimenez R., Guo T., Cavalleri A., Siders C. W., Ráksi F., Squier J. A., Walker B. C., Wilson K. R. and Barty C. P. J., *Picosecond-milliångström Lattice Dynamics Measured by Ultrafast X-Ray Diffraction*, Nature **398**, 310 (1999).
- Rouse A., Rischel Ch. and Gauthier Jean-Claude, *Femtosecond X-Ray Crystallography*, Rev. Mod. Phys. **73**, 17 (2001).
- Rouse A., Rischel C., Fourmaux S., Uschmann I., Sebban S., Grillon G., Balcou Ph., Förster E., Geindre J. P., Audebert P., Gauthier J. C. and Hulin D., *Non-Thermal Melting in Semiconductors Measured at Femtosecond Resolution*, Nature **410**, 65 (2001).
- Rubenchik A. M. and Zakharov V. E., *Strong Langmuir Turbulence in Laser Plasma*, in: Physics of Laser Plasma, A. Rubenchik and S. Witkowski (eds.), North-Holland, Amsterdam, pp. 335 (1991).
- Salzmann D. and Wedin G., *Calculation of the Photoabsorption Coefficient in a Hot and Dense Aluminum Plasma*, Phys. Rev. A **18**, 2695 (1978).
- Salzmann D., Yin R. Y. and Pratt R. H., *Comparison Between Average-Atom and Detailed-Configuration-Type Calculations of the Photoionization Cross Section of hot and Dense Aluminum Plasmas*, Phys. Rev. A **32**, 3627 (1985).
- Salzmann D., *Atomic Physics in Hot Plasmas*, Oxford University Press, New York (1998).
- Saunders G. A, Lambson W. A., Tu Hailing, Bullett D. W., Bach H. and Methfessel S., *Pressure-Induced Elastic Softening of SmS*, J. Phys. C: Solid State Phys. **15**, L551 (1982).

- Schnopper H. W. and Kalata K., *New High-Dispersion High-Resolution X-Ray Spectrometer*, Appl. Phys. Lett. **15**, 134 (1969).
- Schoenlein R. W., Leemans W. P., Chin A. H., Volfbeyn P., Glover T. E., Balling P., Zolotarev M., Kim K. J., Chattopadhyay S., and Shank C. V., *Femtosecond X-Ray Pulses at 0.4 Å generated by 90° Thomson Scattering: A Tool for Probing the Structural Dynamics of Materials*, Science **274**, 236 (1996).
- Schwoerer H., Gibbon P., Düsterer S., Behrens R., Ziener C., Reich C. and Sauerbrey R., *MeV X Rays and Photoneutrons from Femtosecond Laser-Produced Plasmas*, Phys. Rev. Lett. **86**, 2317 (2001).
- Seamann A., Eidmann K., Golovkin I. E., Mancini R. C., Andersson E., Förster E. and Witte K., *Isochoric Heating of Solid Aluminum by Ultrashort Laser Pulses Focused on a Tamped Target*, Phys. Rev. Lett. **82**, 4843 (1999).
- Shank C. V., in: *Ultrashort Laser Pulses Generation and Applications*, Kaiser W. (ed.), Springer, Berlin and New York, pp. 534 (1993).
- Shapiro S. M., Birgeneau R. J. and Bucher E., *Magnetic Excitations in Semiconducting SmS*, Phys. Rev. Lett. **34**, 470 (1975).
- Shockley W. and Bardeen J., *Energy Bands and Mobilities in Monoatomic Semiconductors*, Phys. Rev. **77**, 407 (1950).
- Silberberg Y., *Physics at the Attosecond Frontier*. Nature **414**, 494 (2001).
- Skupsky S., *X-Ray Line Shift as a High-Density Diagnostic for Laser Imploded Plasmas*, Phys. Rev. A **21**, 1316 (1980).
- Smirnov I. A. and Oskotskiĭ V. S., *Semiconductor-Metal Phase Transition in Rare-Earth Semiconductors (Samarium Monochalcogenides)*, Sov. Phys. Usp. **21**, 117 (1978).
- Sobelman I. I., *Atomic Spectra and Radiative Transitions*, 2nd ed., Springer Verlag, Berlin Heidelberg (1992).
- Sobel'man I. I., Vainshtein L. A. and Yukov E. A., *Excitation of Atoms and Broadening of Spectral Lines*, Springer Verlag, Berlin-Heidelberg (1995).

- Sokolowski-Tinten K., Blome C., Blums J., Cavalleri A., Dietrich C., Tarasevitch A., Uschmann I., Förster E., Kammler M., Horn-von-Hoegen M. and von der Linde D., *Femtosecond X-Ray Measurement of Lattice Vibrations near the Lindemann Stability Limit*, Nature **422**, 287 (2003).
- Srajer V., Teng T., Ursby T., Pradervand C., Ren Zh., Adachi Sh., Schildkamp W., Bourgeois D., Wulff M. and Moffat K., *Photolysis of the Carbon Monoxide Complex of Myoglobin: Nanosecond Time-Resolved Crystallography*, Science **274**, 1726 (1996).
- Stamm R., Smith E. W. and Talin B., *Study of Hydrogen Stark Profiles by Means of Computer Simulation*, Phys. Rev. A **30**, 2039 (1984).
- Sundaram S. K. and Mazur E., *Inducing and Probing Non-Thermal Transitions in Semiconductors Using Femtosecond Laser Pulses*, Nature Materials **1**, 217 (2002).
- Takagi S., *A Dynamical Theory of Diffraction for a Distorted Crystal*, J. Phys. Soc. Jpn. **26**, 1239 (1969).
- Taupin D., Bull. Soc. Fr. Minér. Crist. **87**, 469 (1964).
- Tas G. and Maris H. J., *Electron Diffusion in Metals Studied by Picosecond Ultrasonics*, Phys. Rev. B **49**, 15046 (1994).
- Thomsen C., Grahn H. T., Maris H. J. and Tauc J., *Surface Generation and Detection of Phonons by Picosecond Light Pulses*, Phys. Rev. B **34**, 4129 (1986).
- Tighe R. J. and Hooper C. F., *Stark Broadening in Hot, Dense Laser-Produced Plasmas*, Phys. Rev. A **14**, 1514 (1976).
- Tu Hailing, Saunders G. A. and Bach H., *Elastic Behavior Under Pressure of Semiconducting SmS*, Phys. Rev. B **29**, 1848 (1984).
- Uschmann I., *Private Communications* (2004).
- Varma C. M., *Mixed-Valence Compounds*, Rev. Mod. Phys. **48**, 219 (1976).
- Varma C. M. and Heine V., *Valence Transitions in Rare Earth Chalcogenides*, Phys. Rev. B **11**, 4763 (1975).
- Volonté S., *Polarisation Shift Effect in High-Density Plasmas*, J. Phys. D **11**, 1615 (1978).

- Wachter P., *Intermediate Valence and Heavy Fermions*, in: Handbook on the Physics and Chemistry of Rare Earths, Vol. 19-Lanthanides/Actinides: Physics-II, K. A. Gschneidner Jr., L. Eyring, G. H. Lander and G. R. Choppin (eds.), Elsevier Science B. V., pp. 177 (1994).
- Wang J.-K., Saeta P., Buijs M., Malvezzi M. and Mazur, E. in: *Ultrafast Phenomena VI* (eds Yajma T.,Yoshihara K.,Harris C. B. and Shionoya S.), Springer, Berlin, pp. 236 (1989).
- Wark J. S., Woolsey N. C. and Whitlock R. R., *Novel Measurements of High-Dynamic Crystal Strength by Picosecond X-Ray Diffraction*, Appl. Phys. Lett. **61**, 651 (1992).
- Wark J. S., Djaoui A., Rose S. J., He H., Renner O., Missalla T. and Foerster E., *Effect of Velocity Gradients on X-ray Line Transfer in Laser-Produced Plasmas*, Phys. Rev. Lett. **72**, 1826 (1994).
- Wark J., *Table-Top Picosecond Sources*, NATURE **398**, 284 (1999).
- Weyl G. M., *Physics of Laser Induced Breakdown: An Update*, in: Laser-Induced Plasmas and Applications, L. J. Radziemski and D. A. Cremers (eds.), Marcel Dekker, Inc., New York and Basel, pp. 1 (1989).
- Willmott P. R. and Huber J. R., *Pulsed Laser Vaporization and Deposition*, Rev. Mod. Phys. **72**, 315 (2000).
- Woolsey N. C., Back C. A., Lee R. W., Calisti A., Mossé C., Stamm R., Talin B., Asfaw A. and Klein L. S., *Experimental Results on Line Shifts from Dense Plasmas*, J. Quant. Spectrosc. Radiat. Transf. **65**, 573 (2000).
- Yaakobi B., Steel D., Thorsos E., Hauer A. and Perry B., *Direct Measurement of Compression of Laser-Imploded Targets Using X-Ray Spectroscopy*, Phys. Rev. Lett. **39**, 1526 (1977).
- Yaakobi B., Kim H., Soures J. M., Deckman H. W. and Dunsmuir J., *Submicron X-Ray Lithography Using Laser-Produced Plasma as a Source*, Appl. Phys. Lett. **43**, 686 (1983).
- Young H. D and Freeman R. A., *University Physics*, 10th ed., Addison-Wesley (2000).
- Zachariasen W. H., *Theory of X-ray Diffraction in Crystals*, Wiley, New York (1945).

Zewail A. H., *Femtochemistry: Atomic-Scale Dynamics of the Chemical Bond*, J. Phys. Chem. A **104**, 5660 (2000).

Ziener Ch., Uschmann I., Stobrawa G., Reich Ch., Gibbon P., Feurer T., Morak A., Düsterer S., Schwoerer H., Förster E. and Sauerbrey R., *Optimization of $K\alpha$ Brusts for Photon Energies Between 1.7 and 7 keV Produced by Femtosecond-Laser-Produced Plasmas of Different Scale Length*, Phys. Rev. E **65**, 066411 (2002).

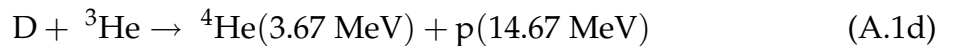
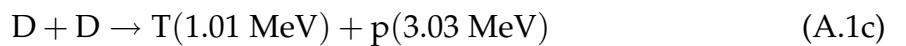
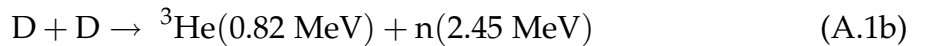
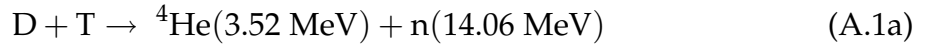
Zhuzhunashvili A. I. and Oks E., Sov. Phys. JETP **46**, 2142 (1977).

Appendix A

Nuclear Fusion

Control of the thermonuclear fusion process for the purpose of producing clean, economically competitive, electrical energy has been the ultimate objective of a worldwide scientific research effort for the last four decades (see e.g. [McCroly and Soures, 1989](#)). The fusion process occurs when a nuclei of low-atomic-weight elements such as hydrogen (deuterium, D, and tritium, T) fuse together to form heavier elements such as helium (He) with the subsequent release of energy in the form of energetic neutrons and charged particles.

The thermonuclear reactions which occurs at the lowest plasma temperatures are ([Ribe, 1975](#))



To overcome the Coulomb repulsive force that keeps atomic nuclei apart, fusion fuel must be heated to temperatures in excess of 50 000 000 K ($\equiv 4.3 \text{ keV}$) ([Ribe, 1975](#))*. In addition, efficient fusion burning requires that the resulting plasma be kept at a high

*Since the nuclei are positively charged, they must have enough energy to overcome the Coulomb repulsion between them. The required Coulomb energy to be overcome is ([Nishikawa and Wakatani, 1994](#))

$$E_{Coul} = \frac{Z_1 Z_2 e^2}{4\pi R_0} \quad (\text{A.2})$$

where Z_1 and Z_2 are the nuclear charges of the fuel species and R_0 is the collision radius which can be estimated by the radius of the nucleus. For deuterium $Z_1 = Z_2 = 1$, $R_0 \approx 5 \times 10^{-15} \text{ m}$, then $E_{Coul} \approx 286 \text{ keV}$. However, in practice, because of quantum mechanical tunneling, the reaction can take place at lower energy.

density for a long enough time to allow burnup of a significant fraction of the fusion fuel.

The current nuclear research is focused on the D-T thermonuclear fusion reaction (A.1a) (see e.g. Nishikawa and Wakatani, 1994). The major fraction of the reaction energy is carried out of the plasma by the 14 MeV neutrons. Since the neutron is not confined by a magnetic field, it hits the vessel walls of the reactor immediately after reaction. The neutron kinetic energy is converted to heat and subsequently to other energy means (e.g., it can be used to run an electric generator).

Two general schemes have been investigated in the past 50 years as means to confine fusion plasmas: (1) *magnetic confinement fusion*, which is based on the use of high-intensity magnetic fields (in excess of several teslas) to confine a relatively low density (10^{14} cm^{-3}) plasma for times on the order of tens of seconds (Ribe, 1975; Hawryluk, 1998), and (2) *inertial confinement fusion* (ICF), which is based on the rapid heating and compression of fusion fuel in a spherical target (of several millimeter diameter) to ultrahigh densities (see below).

Inertial Confinement Fusion

Inertial confinement fusion (ICF) is an alternative approach to controlled fusion that depends on rapid heating and compression of the fusion fuel (deuterium and tritium), contained in a spherical target (such as polymer or glass shell) of several millimeters diameter, to ultrahigh densities (typically $100 \times \text{solid density} \sim 300 \text{ g/cm}^3$). At these densities and temperatures in excess of 5 keV, the fusion reaction rate is high enough to allow efficient burning before the plasma disassembles. Condition for confinement and heating of the plasma is given by *Lawson criterion* (Brueckner and Jorna, 1974)

$$N\tau = 10^{14} \left[\frac{\text{s}}{\text{cm}^3} \right] \quad (\text{A.3})$$

where N is the total ion density (deuterium+tritium). This condition states that one needs, at the same time, sufficiently high ion density N for a sufficient long time τ , in order to produce more energy than that what is lost.

The simplest configuration to realize ICF, is to illuminate uniformly a spherical target from all directions with laser beams (see Figure A.1). The pellet is compressed by the light pressure ($P_{\text{light}} = I_{\text{laser}}/c$), where I_{laser} is the laser intensity and c is the speed

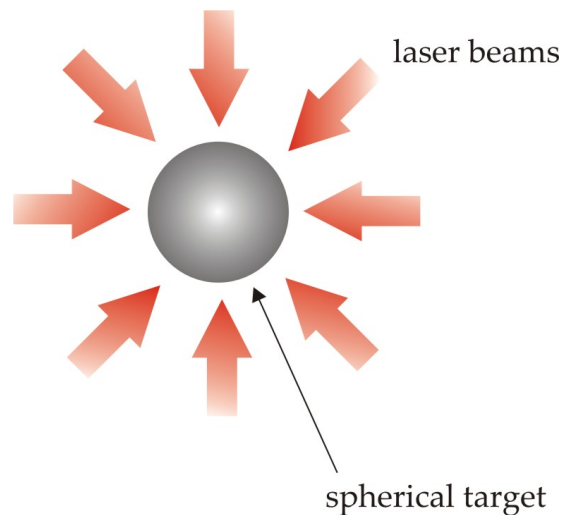


Figure A.1: Direct drive concept for ICF: the target is illuminated uniformly from all directions with laser beams.

of light. The light pressure alone is insufficient to compress the target at ultrahigh density. The pressure needed to compress the fuel to ultrahigh densities ($>50 \text{ Mbar} = 10^{12} \text{ Pa}$, McCrory and Soures, 1989) is provided by ablation of the surface layer (called *ablator*) of the fuel pellet. This causes the rest of the shell to be accelerated toward the center. A small part of the fuel volume (may be as low as 2%) (Lindl *et al.*, 1992) ignites from the heating by the converging shock waves, and begins a wave of fusion reaction, or burn, that moves outward through the succeeding layers of cold compressed fuel, each layer being heated by the alpha particle energy from the fusion occurring inside. This process continues as the target expands and disassembles. Finally the density drops too low and the alpha particle deposition length grows too long to sustain fusion (Foreman, 1995).

Plasma waves excited by different processes during laser-plasma interaction such as resonance absorption and Raman instability, have undesirable effects for ICF. They decay by producing a population of very high energetic electrons, which can penetrate deeply into the fuel (because of their long mean free path) and preheat the core of the imploding sphere prior to the arrival of the compression shock front. If the fuel is heated, then a high pressure is generated in the center of the target, which then halts the compression and high densities are not attained (Bell, 1993). Another important undesirable effect is the nonuniformity of the target illumination. If the compression becomes non-uniform, then Rayleigh-Taylor instability develops and the compression efficiency is strongly reduced (Nishikawa and Wakatani, 1994).

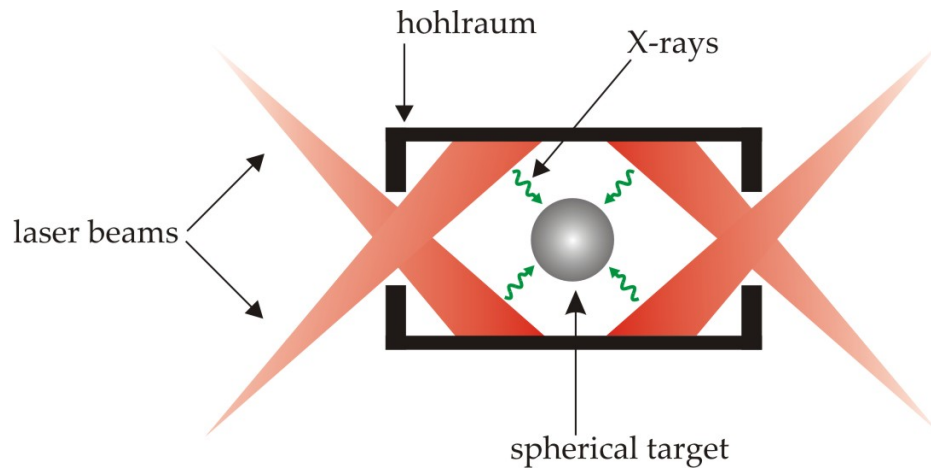


Figure A.2: Indirect drive concept for ICF: laser beams illuminate walls of the hohlraum and the X-rays from the walls of the hohlraum implode the fuel.

To avoid the problems of core preheating and non-uniform compression, the indirect drive concept is developed (Foreman, 1995; Kruer, 1995). In this approach, laser beams heat the walls of a small cylindrical can, called *hohlraum*, which then efficiently radiate in the X-ray region (see Figure A.2). This radiation acts then as the energy driver to implode the fuel (Kruer, 1995). Another challenging aspect for ICF is the target fabrication. The technology of the target fabrication is reviewed by Foreman (1995).

Appendix B

Plasma Potential

The effort concentrated on the research into hot and dense plasmas, particularly astrophysical and laser-produced plasmas, has stimulated extensive theoretical investigation on the behavior of ions in these plasmas and the influence of the plasma environment on atomic processes. In these plasmas, the neighboring electrons and ions have a strong perturbing effect on the atomic energy levels of radiating ions and wave functions of bound electrons, thereby significantly altering the atomic transition probabilities as well as the atomic cross sections. To calculate energy levels and cross sections of various atomic processes in a hot and dense plasmas, in principle, one should account for the interaction of every plasma particle with every other one, but as it is impractical to carry out such a detailed computation, one needs the help of various models which approximate the plasma influence in the ionic potential.

All the models of the ionic potential in hot and dense plasma share some common concepts. The most important is the *screening* of the nuclear electrostatic potential by the free and bound electrons. The quantity that measures the deviation of the screened potential from the Coulombic one is the *screening factor*, $S(r)$, defined by (Salzmann, 1998)

$$V(r) = \frac{1}{4\pi\epsilon_0} \frac{Ze}{r} S(r) \quad (\text{B.1})$$

where Z is the charge of the nucleus, e is the electron charge magnitude and ϵ_0 is the permittivity of free space. The main contribution to the total potential near the nucleus comes from the nuclear Coulomb potential; therefore one expects that for small r : $S(r \rightarrow 0) = 1$. On the other hand, at the large distances the cloud of free and bound electrons completely screens the nuclear potential, so that far from the nucleus $S(r \rightarrow \infty) = 0$, and the total potential diminishes more rapidly than the Coulomb one.

The Coulomb interaction between charged particles plays the essential role in determining the properties of ions immersed in hot and dense plasmas. This interaction is characterized by a parameter called *plasma coupling constant* (Ichimaru, 1982; Salzmann, 1998), Γ , also referred to as *ion-ion coupling constant*, which is defined as the ratio of the potential energy between two ions at average distance R_i , \bar{E}_p , and average kinetic energy, $\bar{E}_k = k_B T$,

$$\Gamma = \frac{\bar{E}_p}{\bar{E}_k} = \frac{1}{4\pi\epsilon_0} \frac{\bar{Z}^2 e^2}{R_i k_B T} \quad (\text{B.2})$$

where $\bar{Z} = N_e/N_i$, N_e is the electron density, N_i is the ion density, k_B is the Boltzmann constant, T is the plasma temperature, R_i is the *ion sphere radius**

$$R_i = \left(\frac{3\zeta}{4\pi N_e} \right)^{1/3} \quad (\text{B.4})$$

and ζ is the number of electrons missing from the atom. A similar definition holds for the *electron-ion coupling constant*, $\Gamma_{e-i} = \bar{Z}e^2 / (4\pi\epsilon_0 R_i k_B T)$, however it is only seldom used in literature (Salzmann, 1998).

When: (i) $\Gamma \leq 0.1$, plasmas are *weakly coupled*, (ii) $\Gamma \geq 10$ plasmas are *strongly coupled*, and (iii) $0.1 < \Gamma < 10$ plasmas are *intermediately coupled*. In weakly-coupled plasmas, the Coulomb interaction can be treated by means of perturbation theory in distinction to strongly coupled plasmas where a perturbation theory is no longer valid. In strongly coupled plasmas, the shift of one ion from its position immediately influences, through their electrostatic interactions, the motion of nearby particles, in much the same way as in a liquid the motions of atoms are correlated. (Ichimaru, 1993).[†]

In the weakly coupled plasmas, the plasma potential can be modelled using *Debye-Hückel theory*. This theory predicts an exponentially decreasing screening factor of the form (Salzmann, 1998)

$$S(r) = \exp\left(-\frac{r}{r_D}\right) \quad (\text{B.5})$$

*In a plasma of a ion density $N_i (= N_e/\zeta)$, the average volume available for every ion is $V_i = 1/N_i$. Frequently one uses the concept of the *ion sphere*, which is a sphere of radius R_i , and which has the same average volume V_i ,

$$V_i = \frac{4\pi}{3} R_i^3 = \frac{1}{N_i} \quad (\text{B.3})$$

[†]At still higher densities and lower temperatures ($\Gamma > 180$), a one component plasma (i.e., plasma consisting of single species of ions) undergoes a freezing transition into a BCC (body centered cubic) crystalline state (Ogata, 1992; Ichimaru, 1993).

where r_D is the Debye screening length, and it is given by (Nishikawa and Wakatani, 1994)

$$r_D = \sqrt{\frac{\epsilon_0 k_B T_e}{e^2 N_e}} \quad (\text{B.6})$$

Substitution of Eq.(B.5) into Eq.(B.1) yields the Debye-Hückel potential

$$V(r) = \frac{1}{4\pi\epsilon_0} \frac{Ze}{r} \exp\left(-\frac{r}{r_D}\right) \quad (\text{B.7})$$

The Debye-Hückel potential is obtained using (i) the Poisson equation which reflect the electrostatic nature of the plasma particles, (ii) the Boltzman statistical distribution for ions and electrons, and (iii) under condition that $eV(r)/k_B T_e \ll 1$. Thus, the Debye-Hückel potential is valid for *high temperature plasmas (weakly coupled plasmas)* and its reliability is limited by the validity of the Boltzman statistics.

To model atomic properties in intermediately coupled plasmas such as merging of the ionic levels into continuum and line shift, a plausible approximation is to use a plasma potential which assumes charge neutrality inside the ion sphere. These models are called *ion sphere models*. To this category belongs the *Thomas-Fermi model* and *uniform-electron gas ion sphere model* (UEG-ISM) (Salzmann, 1998). These models assume a nucleus of charge Z , and the same number, Z , of electrons inside the ion sphere nucleus.

The Thomas-Fermi model is widely used to simulate the ionic potential in hot plasmas, in particular those of high- Z material. It uses the Poisson equation and Fermi-Dirac statistics for distribution of electrons. Since there is no analytic expression for Thomas-Fermi potential, it can be inferred from an implicit expression of the form (Salzmann, 1998)

$$N_e(r) = \frac{1}{2\pi^2} \left(\frac{2m_e k_B T_e}{\hbar^2}\right)^{3/2} F_{1/2}\left(\frac{\mu + eV(r)}{k_B T_e}\right) \quad (\text{B.8})$$

where m is the electron mass, μ is the chemical potential and $F_{1/2}$ is the Fermi-Dirac integral given by

$$F_j(x) = \int_0^\infty \frac{y^j dy}{1 + \exp(y - x)} \quad (\text{B.9})$$

A widely used approximation to model the ionic potential in intermediately coupled plasmas, based on the ion sphere, assumes that the free electron polarization around the nucleus has only negligible effect on the potential, and the free electrons are distributed in space more or less uniformly (this situation is achieved when the

temperature is high enough so that the kinetic energy overcomes the potential energy). This model is called *uniform-electron gas ion sphere model* (UEG-ISM). In this case the electrostatic potential generated by the free electrons is given by (Salzmann, 1998)

$$V_{pl}(r) = -\frac{1}{4\pi\epsilon_0} \frac{3}{2} \frac{\zeta e}{R_i} \left[1 - \frac{1}{3} \left(\frac{r}{R_i} \right)^2 \right] \quad (\text{B.10})$$

and the electrostatic potential energy seen by the bound electron is

$$U(r) = -\frac{1}{4\pi\epsilon_0} \frac{Ze^2}{r} + \frac{1}{4\pi\epsilon_0} \frac{3}{2} \frac{\zeta e^2}{R_i} \left[1 - \frac{1}{3} \left(\frac{r}{R_i} \right)^2 \right], \quad r \leq R_i \quad (\text{B.11})$$

Eqs.(B.10) and (B.11) are very successful in modelling many atomic phenomena in hot and dense plasmas such as e.g. line shift (see Chapter 4), and lead to analytical expressions which can easily be used from experimentalists.

Appendix C

Line Broadening Mechanisms

The width of a spectral line is a parameter that is very sensitive to the plasma conditions around the emitting ions. The broadening mechanisms which are important in a plasma are natural broadening, Doppler broadening, opacity broadening, electron impact broadening and Stark broadening (Cooper, 1966; Hauer and Baldis, 1989). These broadening effects add up, and the total line width is a combination of all of them. However, in general, only one of these effects dominates, depending on the local plasma temperature and density, while the others are regarded as small corrections (Salzmann, 1998).

Below, these broadening mechanisms are briefly reviewed. In particular, to illustrate the principles of electron impact broadening and quasistatic Stark broadening, discussions are based on simplified pictures reviewed by Cooper (1966), Griem (1974) and Salzmann (1998), which are useful in providing qualitative insights into the dependence of the FWHM of a spectral line on electron density and/or electron temperature.

Natural line broadening: This broadening mechanism of spectral lines is due to the finite lifetime of the excited states (Mandl, 1992). The width due to the natural broadening is the *minimum width* possible for a spectral line. For a spectral line emitted in a transition $u \rightarrow l$, where u and l stand for the quantum numbers which characterize the upper and the lower states, respectively, the natural line width (in the energy scale) is given as

$$\Gamma_{u \rightarrow l} = \frac{\hbar}{\tau_u} + \frac{\hbar}{\tau_l} \quad (\text{C.1})$$

where τ_u is the lifetime of the state u (the excited state), τ_l is the lifetime of the ground (lower) state l , and \hbar is the reduced Planck constant. If the state l represent the ground

state, which cannot decay, than $\tau_l = \infty$, and the natural line width takes the form

$$\Gamma_u = \frac{\hbar}{\tau_u} \quad (\text{C.2})$$

Typically, the lifetime of the excited state τ_u is of the order 10^{-8} s, giving $\Gamma_u \approx 10^{-7}$ eV (or 10^{-7} mÅ). In laboratory plasmas this natural line width is much smaller than the broadening caused by other mechanisms (which is of the order of a few mÅ) and is only seldom measurable.

Doppler Broadening: The Doppler broadening is caused by thermal motion of the radiating ions and is, generally, the dominant broadening mechanism in a low density plasmas with emitters heaving a moderate core charge Z_r . When no other broadening mechanisms are taken into account, the effect of the ions motion in the plasma is the broadening of the emission line into a Gaussian shape, whose FWHM is (Salzmann, 1998)

$$\begin{aligned} \Delta\lambda_{\text{FWHM}} &= 2\lambda_0 \sqrt{\frac{2k_B T \log 2}{Mc^2}} \\ &= 5.085 \times 10^{-2} \lambda_0 [\text{\AA}] \sqrt{\frac{T_i [\text{eV}]}{A_r}} \quad [\text{m\AA}] \end{aligned} \quad (\text{C.3})$$

where M is the mass of the radiating ion, T_i is the ion temperature, A_r is the relative atomic mass (or atomic weight) of the radiating ion ($M = A_r \times 1.660538 \times 10^{-27}$ kg), k_B is the Boltzman constant and c is the speed of light.

Electron Impact Broadening: The electron impact broadening is caused by collisions of electrons with the radiating ions and is relevant in the case when these collisions are very rapid, with a duration much shorter than the natural lifetime of the decaying level. The rapid scattering processes are mainly due to the rapidly moving free electrons in the plasma. Assuming that: (i) the motion of the perturbing particles can be described by classical trajectories and the wave nature of the perturber is neglected, (ii) the trajectory of the perturbing particle is rectilinear, (iii) the greatest influence on the radiator is due to its interaction with its nearest neighbor, and, (iv) the perturbation is elastic and does not induce transitions among the energy levels of the radiator, then, the width of the spectral line which is broadened due to the impact of

the electrons with a radiator is (Salzmann, 1998)

$$\Delta\lambda_{\text{FWHM}}[\text{mÅ}] \simeq 3.039 \times 10^{-23} (\lambda_0[\text{mÅ}])^2 \frac{Z_r^2 N_e [\text{cm}^{-3}]}{\sqrt{T_e} [\text{eV}]} \times \left[0.923 - \ln \left(6.737 \times 10^{-11} \frac{Z_r \sqrt{N_e [\text{cm}^{-3}]}}{T_e [\text{eV}]} \right) \right] \quad (\text{C.4})$$

where λ_0 is the unperturbed wavelength of the spectral line, Z_r represents the charge of the radiator, T_e is the electron temperature and N_e is the electron density. Eq. (C.4) shows a very important scaling property of the electron broadening, namely that this width is approximately proportional to the electron density and inversely proportional to the square root of the electron temperature

$$\Delta\lambda_{\text{FWHM}} \propto \frac{N_e}{\sqrt{T_e}} \quad (\text{C.5})$$

Quasi-Static Stark Broadening: The origin of quasi-static Stark broadening are the relatively slowly changing microfields, generated by surrounding ions, which split and shift energy levels of the radiating ions. This broadening mechanism is valid when the interaction time between a perturber and a radiator is longer than the time between collisions (Salzmann, 1998). The width of the spectral line in the quasistatic approximation is (Griem, 1974)

$$\Delta\lambda_{\text{FWHM}}[\text{mÅ}] \approx 1.475 \times 10^{-15} \frac{Z_p^{1/3}}{Z_r} (\lambda_0[\text{Å}])^2 (n_u^2 - n_l^2) N_e^{2/3} \quad (\text{C.6})$$

where Z_p is the charge of a perturber, and, u and l stand for the quantum numbers which characterize the upper and the lower states involved in radiative transition.

Opacity Broadening: The origin of opacity broadening is the transport of emission from the region of radiation to the observing instrument (Hauer and Baldis, 1989). Contribution of opacity broadening to FWHM of a spectral line can not be brought into a simple analytic expression because it involves solution of the radiative transfer equation

$$\nabla I(\lambda, \mathbf{r}) = J(\lambda, \mathbf{r}) - \kappa I(\lambda, \mathbf{r}) \quad (\text{C.7})$$

where $I(\lambda, \mathbf{r})$ is the intensity of radiation at a given wavelength and at a particular point \mathbf{r} in the plasma, J is the emissivity (which depends on the spontaneous radiative rate) and κ is the absorption coefficient of the plasma (which depends on the absorption oscillator strength) (Salzmann, 1998). A relatively simple formulas are available only for plasmas in full thermodynamic equilibrium (see e.g. Salzmann, 1998).

Appendix D

Doppler Shift

The Doppler effect* is a phenomenon observed with *all waves*. It states that, whenever a source (which emits waves) moves relative to an observer or an observer moves relative to a source, the frequency of the wave at the location of the observer is shifted relative to the frequency of the source. In plasmas, owing to the thermal motion of the emitting ions, the frequency of the detected photon in the rest frame (placed on the detector), ω_{obs} , differs from the frequency emitted in the frame of the moving ion, ω_s .

- When the ions move away from the detector, the frequency observed on the detector is (Young and Freedman, 2000)

$$\omega_{obs} = \omega_s \sqrt{\frac{c - v_{obs}}{c + v_{obs}}} \quad (\text{D.1})$$

where v_{obs} is the component of the ion velocity in the direction of observation, and c is the speed of light. Eq.(D.1) states that, the observed frequency in this case is red-shifted i.e., the measured frequency is lower than that of the source (radiation ion).

- When the ions approaches the detector, the frequency observed on the detector is (Young and Freedman, 2000)

$$\omega_{obs} = \omega_s \sqrt{\frac{c + v_{obs}}{c - v_{obs}}} \quad (\text{D.2})$$

i.e., the observed frequency in this case is blue-shifted i.e., the measured frequency is higher than that of the source (radiation ion).

To calculate motional Doppler shifts in a constrained flow plasma, we will consider the situation shown in Figure D.1(a). Let us suppose that the ions move along y -axis,

*Named after the Austrian scientist Christian Doppler (1803-1853).

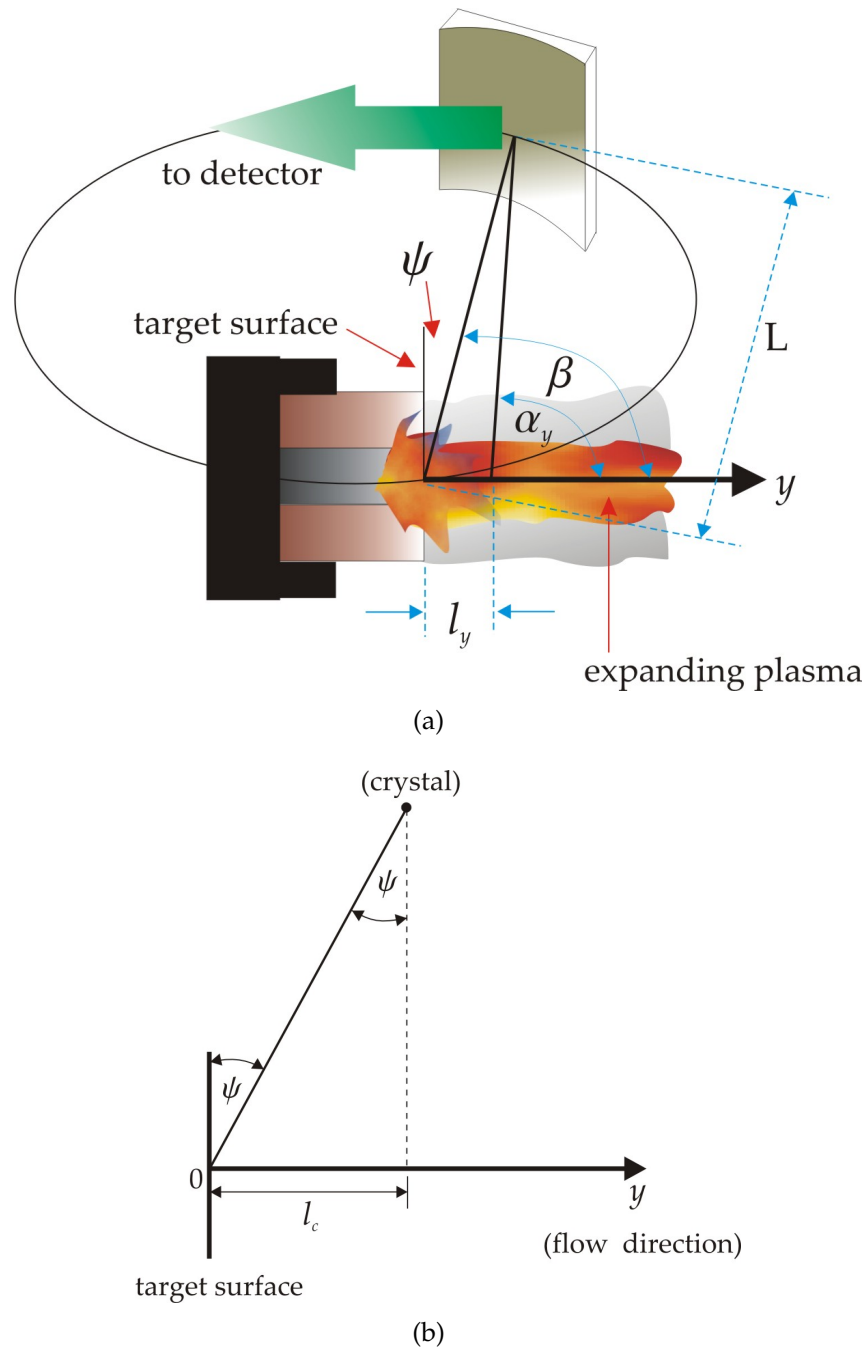


Figure D.1: Scheme of the experimental setup which is used to calculate the motional Doppler shift in a constrained flow plasma. (a) The plasma flows in the y direction, and the crystal which collect the radiation from the plasma, is aligned to observe the radiation at an angle ψ to the target surface, (b) The radiating ions, up to $y = l_c = L \sin \psi$, approaches the crystal.

with velocity v . The crystal is aligned to observe the radiation at an angle ψ to the target surface. At the distance l_y from the target surface, the angle between the flow and observation directions is

$$\alpha_y[\text{deg}] = \beta[\text{deg}] + \frac{l_y}{L} \frac{180}{\pi} \quad (\text{D.3})$$

where $\beta = \pi/2 - \psi$ and L is the distance between the crystal and target surface. The component of the ion velocity in the observation direction is

$$v_{obs} = v \cos \alpha_y = v \cos \left(\beta + \frac{l_y}{L} \frac{180}{\pi} \right) \quad (\text{D.4})$$

During expansion of the plasma, radiating ions will approach the crystal up to $y = l_c = L \sin \psi$ (see Figure D.1(b)), because, as they move in y direction, at each subsequent distance from the target surface (starting at $y = 0$) they will be closer to the crystal. In this case, the frequency of photons which arrive on the crystal is calculated using Eq.(D.2). In other word, they experience blue Doppler shift (the observed frequency is higher than that of the source), which in the wavelength scale can be written as

$$\Delta\lambda_{Doppler} = \lambda_{obs} - \lambda_s = \lambda_{obs} \left[1 - \left(\frac{c + v \cos \alpha_y}{c - v \cos \alpha_y} \right)^{1/2} \right] \quad (\text{D.5})$$

where α_y is given by Eq.(D.3). In this case, $\Delta\lambda_{Doppler}$ is negative quantity because the observed wavelength is shorter than that of the source (radiating ion). On the other hand, at $y > l_c$, the emitting ions move away from the target, and the observed photons experience red-Doppler shift

$$\Delta\lambda_{Doppler} = \lambda_{obs} - \lambda_s = \lambda_{obs} \left[1 - \left(\frac{c - v \cos \alpha_y}{c + v \cos \alpha_y} \right)^{1/2} \right] \quad (\text{D.6})$$

Now, $\Delta\lambda_{Doppler}$ is positive quantity because the observed wavelength is longer than that of the source (radiating ion).

Appendix E

The Stark Effect for H-like Ions and Parabolic Quantum Numbers

The Stark effect is the splitting of atomic (ionic) levels under the action of an external electric field (Sobelman, 1992). Interaction between the atom and the electric field, $\vec{\epsilon}$, adds to the ionic Hamiltonian a term

$$V = -\vec{D} \cdot \vec{\epsilon} \quad (\text{E.1})$$

where \vec{D} is the electric dipole moment of the atom (see e.g. Mandl, 1992). Due to this interaction, the ionic levels are split according to the absolute value of the magnetic quantum number, m , which means that the magnetic sublevels with $+m$ and $-m$ remain degenerate.

In spherical coordinates, the Stark effect is evaluated by using the bound state perturbation theory for the degenerate case. Energies of Stark sublevels (caused by perturbation (E.1)) are found by solving the system of equations

$$\sum_{\alpha=1}^s \left(V_{\beta\alpha} - E_n^{(1)} \right) C_{\alpha} = 0 \quad (\text{E.2})$$

where $V_{\beta\alpha} = \int \psi_{\beta}^* V \psi_{\alpha} d^3r$, ψ_{α} and ψ_{β} denote two different quantum states (characterized with principal quantum number n , angular momentum quantum number l and magnetic quantum number m), C_{α} are constant coefficients (for details, see e.g. Mandl, 1992), s is the degeneracy of the state with n without inclusion of the spin i.e. $s = \sum_{l=0}^{n-1} = n^2$, and $\beta=1, 2, \dots, s$. Thus, this problem involves solution of a set of s homogeneous equations with s -unknowns, which sometime (especially for higher principal quantum numbers, $n \geq 3$) is not practical.

Fortunately, the Stark effect can also be treated in a simpler fashion by using parabolic

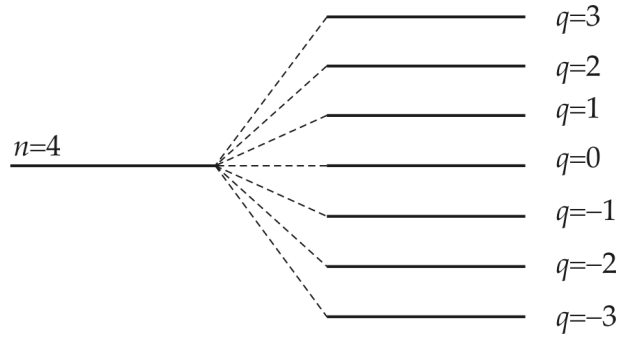


Figure E.1: Splitting of the energy level with principal quantum number $n = 4$. For a given principal quantum number n , the electric quantum number q can take $2n - 1$ values, $q = 0, \pm 1, \pm 2, \pm 3, \dots, \pm(n - 1)$.

coordinates (Sobelman, 1992),

$$\zeta = \sqrt{x^2 + y^2 + z^2} + z = r(1 + \cos \theta) \quad (\text{E.3})$$

$$\eta = \sqrt{x^2 + y^2 + z^2} - z = r(1 - \cos \theta) \quad (\text{E.4})$$

$$\varphi = \arctan\left(\frac{y}{x}\right) \quad (\text{E.5})$$

In parabolic coordinates the stationary state of a discrete spectrum is defined by the *parabolic quantum numbers* n_1 and n_2 , and magnetic quantum number m . The principal quantum number n is connected with n_1 and n_2 by the relation

$$n = n_1 + n_2 + |m| + 1 \quad (\text{E.6})$$

The selection rules with respect to the magnetic quantum number m are (Bethe and Salpeter, 1977; Sobelman, 1992),

$$\Delta m = 0, \quad \pi - \text{components} \quad (\text{E.7})$$

$$\Delta m = \pm 1, \quad \sigma - \text{components} \quad (\text{E.8})$$

while for the parabolic quantum numbers n_1 and n_2 , there is no selection rule (Bethe and Salpeter, 1977).

In parabolic coordinates, the first order correction to the energy level with the principal quantum number n (or the linear Stark effect term) is (Bethe and Salpeter, 1977; Sobelman, 1992),

$$\Delta E^{(1)} = \frac{3}{2} \frac{n(n_1 - n_2)}{Z} ea_0 \epsilon \quad (\text{E.9})$$

where a_0 is the Bohr radius, e is the electron charge magnitude and Z is the nuclear charge of the ion. From this equation, it is obvious that the energy of the linear Stark

effect term, aside from the dependence on the principal quantum number n , depends on the difference $(n_1 - n_2)$ which is called the *electric quantum number*, q . For a given principal quantum number n the electric quantum number, q , can take the values (Sobelman, 1992),

$$q = n_1 - n_2 = 0, \pm 1, \pm 2, \pm 3, \dots, \pm(n - 1) \quad (\text{E.10})$$

Thus, according to Eq.(E.9) and (E.10), the level with principal quantum number n , is splited into $(2n - 1)$ Stark sublevels. Although there is no explicit dependence in Eq.(E.9) on the magnetic quantum number m , there is implicit dependence because of the relation (E.6). Now, for an isolated hydrogen-like ion, the energy of a level with principal quantum number n and electric quantum number q , is

$$E_{nq}^{(1)} = -\frac{1}{4\pi\epsilon_0} \frac{Z^2 e^2}{2a_0} \frac{1}{n^2} + \Delta E^{(1)} = -\frac{1}{4\pi\epsilon_0} \frac{Z^2 e^2}{2a_0} \frac{1}{n^2} + \frac{3}{2} \frac{nq}{Z} e a_0 \epsilon \quad (\text{E.11})$$

With increasing field strength ϵ , a term which is quadratic in the electric field appears in Eq.(E.11). This term is called *the quadratic Stark effect term*. According to the perturbation theory in parabolic coordinates, the second-order correction to the energy or the quadratic Stark effect term is (Bethe and Salpeter, 1977; Sobelman, 1992),

$$\Delta E^{(2)} = -(4\pi\epsilon_0) \frac{1}{16} \left(\frac{n}{Z}\right)^4 [17n^2 - 3q^2 - 9m^2 + 19] a_0^3 \epsilon^2 \quad (\text{E.12})$$

thus, for an isolated hydrogen-like ion, the energy of a level with principal quantum number n , electric quantum number q and magnetic quantum number m , takes the form

$$\begin{aligned} E_{nqm}^{(2)} &= E_{nq}^{(1)} + \Delta E^{(2)} \\ &= -\frac{1}{4\pi\epsilon_0} \frac{Z^2 e^2}{2a_0} \frac{1}{n^2} + \frac{3}{2} \frac{nq}{Z} e a_0 \epsilon \\ &\quad - (4\pi\epsilon_0) \frac{1}{16} \left(\frac{n}{Z}\right)^4 [17n^2 - 3q^2 - 9m^2 + 19] a_0^3 \epsilon^2 \end{aligned} \quad (\text{E.13})$$

From the last equation it is obvious that, in contrast to Eq.(E.11), inclusion of the quadratic Stark effect term removes explicitly the degeneracy with respect to $|m|$.

Appendix F

Important Physical Constants of SmS

Lattice constant

Pressure [GPa]	Lattice constant [Å]	Reference
atm. pressure	5.970	(Jayaraman <i>et al.</i> , 1970)
0.30	5.958	(TuHailing <i>et al.</i> , 1984)
0.60	5.945	(TuHailing <i>et al.</i> , 1984)
0.67	5.800	(Saunders <i>et al.</i> , 1982)

Energy parameters

Quantity	Symbol	Value	Units	References
Energy gap	E_g	0.10	eV	Varma (1976)
		0.15	eV	Wachter (1994)
		0.20	eV	Landolt-Börnstein (2001)
		0.40	eV	Chatterjee <i>et al.</i> (1972)
dE_g/dP	dE_g/dP	-100	meV/GPa	Landolt-Börnstein (2001)
Deformation potential	Φ	4.7	eV	Jayaraman <i>et al.</i> (1974)

Bulk modulus

Pressure [GPa]	Bulk modulus [GPa]	References
atm. pressure	50.0	Saunders <i>et al.</i> (1982)
0.60	45.8	TuHailing <i>et al.</i> (1984)
0.67	40.0	Saunders <i>et al.</i> (1982)

Elastic constants and their pressure derivatives at atmospheric pressure

Quantity	Value	Units	References
C_{11}	127	GPa	Saunders <i>et al.</i> (1982), TuHailing <i>et al.</i> (1984)
C_{12}	12	GPa	Saunders <i>et al.</i> (1982), TuHailing <i>et al.</i> (1984)
C_{44}	26.9	GPa	Saunders <i>et al.</i> (1982), TuHailing <i>et al.</i> (1984)
dC_{11}/dP	10.4	-	Saunders <i>et al.</i> (1982), TuHailing <i>et al.</i> (1984)
dC_{12}/dP	-1.6	-	Saunders <i>et al.</i> (1982), TuHailing <i>et al.</i> (1984)
dC_{44}/dP	-0.08	-	Saunders <i>et al.</i> (1982), TuHailing <i>et al.</i> (1984)

Elastic constants and their pressure derivatives at 0.6 GPa

Quantity	Value	Units	References
C_{11}	128.20	GPa	TuHailing <i>et al.</i> (1984)
C_{12}	4.70	GPa	TuHailing <i>et al.</i> (1984)
C_{44}	26.85	GPa	TuHailing <i>et al.</i> (1984)
dC_{11}/dP	-6.3	-	TuHailing <i>et al.</i> (1984)
dC_{12}/dP	-22.8	-	TuHailing <i>et al.</i> (1984)
dC_{44}/dP	-0.08	-	TuHailing <i>et al.</i> (1984)

Thermic quantities (semiconductor phase)

Quantity	Symbol	Value	Units	References
Melting temperature	T_m	2210	K	Landolt-Börnstein (2001)
Debye temperature	Θ_D	247	K	Landolt-Börnstein (2001)
		155	K	Landolt-Börnstein (2001)
Heat capacity	C	1.8×10^6	J/(m ³ ·K)	Kaminskiĭ and Solov'ev (2001)
Thermal conductivity	κ	6.42	W/(m·K)	Golubkov <i>et al.</i> (2003)

Magnetic quantities (semiconductor phase)

Quantity	Symbol	Value	Units	References
Magnetic susceptibility	χ	2.185×10^{-3}	-	see Remark 1
$d\chi_{mol}/dP$	$d\chi/dP$	3.071×10^{-4}	GPa ⁻¹	Maple and Wohleben (1971)
Van Vleck susceptibility	χ_{vv}	3.589×10^{-3}	-	Birgeneau <i>et al.</i> (1972)

Optical properties at the wavelength of 800 nm (semiconductor phase)

Quantity	Symbol	Value	References
Reflectivity	R	15%	Landolt-Börnstein (2001)
Penetration depth	ζ	143.7 nm	See Remark 2.

Electric and thermoelectric quantities

Quantity	Symbol	Value	Units	References
Electron mobility (semicond. phase)	μ	20 to 25	cm ² /(V·s)	Landolt-Börnstein (2001)
Thermoelectric power at 435-455 K	α_{the}	800	μ V/K	Golubkov <i>et al.</i> (2003)

Remark 1: The magnetic susceptibility for semiconducting SmS was measured as a function of temperature by Maple and Wohleben (1971). At about 300 K, the value of molar magnetic susceptibility in *cgs-emu* units is $\chi_{mol}^{cgs-emu} \simeq 5.57 \times 10^{-3}$ emu/mol; magnetic susceptibility is $\chi^{cgs-emu} = (\rho/W_a)\chi_{mol}^{cgs-emu} \simeq 1.739 \times 10^{-4}$, where ρ (=5.69469 g/cm³) is the mass density of SmS and W_a (=182.426 g/mol) is the molar mass of SmS. This value is converted to SI units by using the conversion

formula (Callister, 2001)

$$\chi^{SI} = 4\pi\chi^{cgs-emu} = 4\pi \cdot 1.739 \times 10^{-4} = 2.185 \times 10^{-3}$$

Remark 2: The absorption length, ζ_{las} , for the laser light of a wavelength, λ_{las} , in an absorbing material is defined as the inverse of the linear absorption coefficient, α_{las} , i.e.,

$$\zeta_{las} = \frac{1}{\alpha_{las}} = \frac{\lambda_{las}}{4\pi n_2} \quad (\text{F.1})$$

where n_2 is the imaginary part of the refractive index $n(=n_1+in_2)$. n_2 is related to the real and imaginary part of the dielectric function $\epsilon(=\epsilon_1+i\epsilon_2)$ by

$$\begin{aligned} \epsilon_1 &= n_1^2 - n_2^2 \\ \epsilon_2 &= 2n_1n_2 \end{aligned} \quad (\text{F.2})$$

The real and imaginary parts of the dielectric function for semiconducting SmS in the range of photon energies up to 12 eV, were published by Batlogg *et al.* (1976). For $E_{ph} = 1.55$ eV (Ti:sapphire laser), $\epsilon_1 \approx 4.9$ and $\epsilon_2 \approx 2$, thus, using Eqs.(F.1) and (F.2), the value $\zeta_{las} \simeq 143.7$ nm is obtained.

Appendix G

Applications of SmS

Due to the moderate pressures where the semiconductor-metal phase transition appears, SmS is an ideal candidate for some interesting applications such as *data storage* and *thermal-to-electric* energy conversion. Pohl *et al.* (1974) for the first time demonstrated that polished SmS crystals glued to quartz show reflectivity-vs-temperature hysteresis (phase transitions taking place were monitored by using reflectivity measurement with a He-Ne laser). This behavior is attributed to a temperature dependent stress generated by the different thermal expansion of the sample and substrate which then drives the semiconductor-metal phase transition. Thus, this suggests that when samples are used for data storage, the information can be recorded and erased by temperature cycling, which leaves the surface in the metallic or semiconductor state.

Another interesting application is conversion of thermal energy to electric energy. Kaminskiĭ and Solov'ev (2001) demonstrated that heating of SmS single crystals gives rise to electro-motor-force (EMF) generation. This effect is associated with a change in the Sm ion valence as a result of a Mott-type phase transition occurring in the system of impurity (interstitial) Sm^{2+} ions. The reasons for generation of the EMF were: (i) the onset of the temperature gradients in the sample as a result of absorption and release of the energy during a valence change $\text{Sm}^{2+} \rightleftharpoons \text{Sm}^{3+} + e^-$, and (ii) the formation of the conduction-electron concentration gradients because of a valence change $\text{Sm}^{2+} \rightleftharpoons \text{Sm}^{3+} + e^-$.

Appendix H

Characterization of the SmS Crystal

H.1 Introduction

In this Appendix, the X-ray investigations of the quality of the SmS crystal used in time resolved experiments presented in Chapter 7, are reported. These investigations ensure that, the observed phenomena belong to a single crystalline regions, i.e., they helped to isolate single crystallin regions. The quality of the crystal is investigated using two methods: (i) Measurement of the rocking curves at different regions on the target surface, and (ii) X-ray diffraction topography. The theoretical background, necessary for interpretation of the experimental results, is outlined in Section H.2. Experimental results and discussion are presented in Section H.3.

H.2 Theoretical Background

X-ray diffraction is a versatile, non-destructive technique for investigating the quality of a crystal. The method uses a beam of X-rays to irradiate a specimen at various incidence angles θ , see Figure H.1. The X-rays are diffracted from the crystal according to the Bragg's law

$$2d_{hkl} \sin \theta = \lambda \quad (\text{H.1})$$

where d_{hkl} is the spacing of the diffracting planes (hkl), and for cubic crystals it is given by

$$d_{hkl} = \frac{a}{\sqrt{h^2 + k^2 + l^2}} \quad (\text{H.2})$$

According to their quality, crystals can be divided in two classes: *perfect* crystals and *imperfect (mosaic)* crystals. A perfect crystal is a three dimensional repetition of a unit

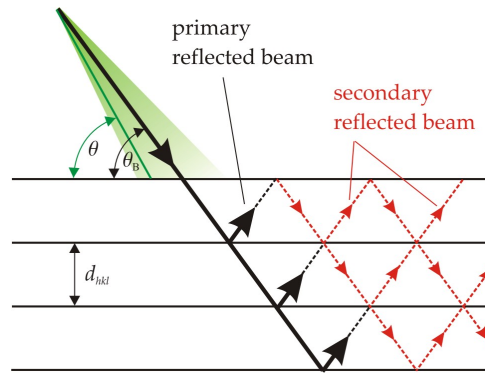


Figure H.1: Diffraction from a crystal: illustration of the reflection of the reflected beam.

cell.* When the primary beam falls on a crystal at the correct Bragg's law angle, there will be the usual primary diffracted beam. However, as illustrated in Figure H.1 the primary diffracted beam will make the correct Bragg angle with the crystal planes in its way to leave the crystal and as a consequence there will be a second reflected beam which propagates in the direction of the primary beam. The theory of X-ray diffraction which completely *neglect* the second reflected beam is called the *kinematic theory of X-ray diffraction*. The more rigorous treatment, which makes the proper *allowance* for the reflection of the second reflected beam is called the *dynamical theory of X-ray diffraction*. Following the dynamical theory of X-ray diffraction, the reflectivity from an ideal crystal in the reflection geometry depends on the incident angle with the diffracting planes (θ), wavelength of the used radiation (λ), Bragg's angle (θ_B), polarization of the radiation (C) and structure factor (F_{hkl}) (the explicit expressions for the reflectivity and structure factor are given by e.g. Zachariasen, 1945, Chapter 3 and Authier, 2001, Chapter 7) i.e.,

$$R_{hkl} = f(\theta, \lambda, \theta_B, C, |F_{hkl}|^2) \quad (\text{H.3})$$

where f stands for 'function of (\dots)'. If one measures the integrated intensity from an ideally perfect crystal and interpret the measurements by using equations for an ideally perfect crystal, there is a satisfactory agreement, but for the great majority of real crystals the X-ray reflections are stronger than the dynamical theory allows. The experimental values of integrated reflecting power often exceeds the theoretical value by a factor of ten or more while at the same time the directly measured FWHM amounts to minutes of arc instead of the few seconds of arc which is predicted by the ideal-crystal

*The unit cell is the basic structural unit or building block of the crystal structure and defines the crystal structure by virtue of its geometry and the atom positions within.

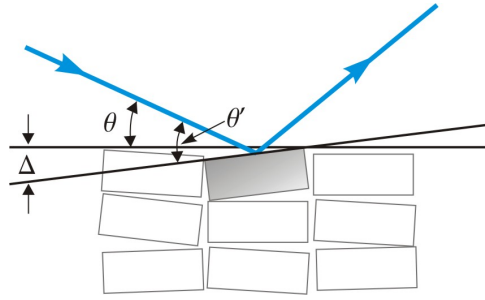


Figure H.2: Scheme of the mosaic structure model of a real crystal. The atoms are arranged in blocks (grains), each block being itself an ideal crystal, but adjacent blocks having appreciable variations in orientation. θ is the angle which the incident beam makes with the mean lattice planes, θ' is the glancing angle for a single block and Δ is the magnitude of the angular deviation from the mean.

theory (dynamical theory). Because of these discrepancies between theory and experiment, one is forced to conclude that ideal crystals are not entirely satisfactory models of real crystals. In order to account for the observations, Darwin (1914) proposed the *mosaic crystal model* of a real crystal. He suggested that the atoms are arranged in *blocks*, each block being itself an ideal crystal, but adjacent blocks have appreciable variations in orientation (see Figure H.2). These ideal-crystal-blocks are called *grains*. The orientation of the grains can be described by the distribution function (*mosaic spread*) $W(\Delta)$, where Δ is the magnitude of the angular deviation from the mean lattice-plane orientation. For instance, $W(\Delta)$ can be of the form (Zachariasen, 1945)

$$W(\Delta) = \frac{1}{\eta\sqrt{2\pi}} \exp\left(-\frac{\Delta^2}{2\eta^2}\right) \quad (\text{H.4})$$

where η is the standard deviation.

Assuming that the mosaic crystal has a shape of a plane parallel plate and is composed of layers, each layer having many ideal crystal blocks (grains), the reflecting power of a single layer, Ω , is (Zachariasen, 1945)

$$\Omega(\theta - \theta_B) = \int W(\Delta) R_{hkl}(\theta - \theta_B + \Delta) d\Delta \quad (\text{H.5})$$

Note that the mosaic spread, $W(\Delta)$, can be also a Lorentzian-like, as well (Authier, 2001).

H.3 Experimental Results and Discussion

The quality of the SmS crystal is investigated using two methods: (i) Measurement of the rocking curves at different regions on the target surface, and (ii) X-ray diffraction

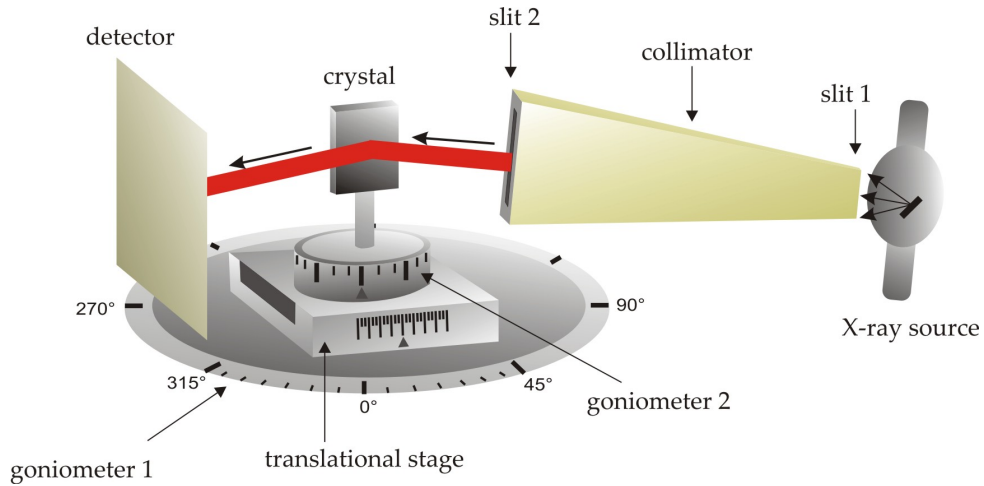


Figure H.3: Scheme of the experimental setup for measuring the rocking curves at different regions from the target surface. The Bragg angle is adjusted using goniometer 1, whereas the angular range used to obtain rocking curves is provided by goniometer 2. The translational stage is used to select different measuring regions on the crystal. The diffracted intensity is recorded by a scintillator detector.

topography. By measuring the rocking curves at different regions from the target surface one can determine *quantitatively* angles between grains composing the crystal and their spatial extend, whereas the *visualization* of the grains is done using X-ray diffraction topography. The details of the measurements and experimental results for each method are presented in subsections [H.3.1](#) and [H.3.2](#).

H.3.1 Measurement of the SmS Crystal Rocking Curves

The rocking curves, measured at different regions on the crystal surface, give hints to the local defects in the crystal lattice and the general disorientation from measuring region to measuring region. These information can be inferred by analyzing the shape of the rocking curves and changes on the peak position from one measuring region to another. The SmS-crystal rocking curves are recorded by using the setup schematically shown in [Figure H.3](#). An incident beam ($\text{Cu K } \alpha$, $\lambda = 1.54 \text{ \AA}$) coming from a source, collimated by a slit (slit 2) $0.2 \times 1 \text{ mm}^2$ (horizontal \times vertical), impinges on the SmS crystal set for a Bragg diffraction (004 reflection, $\theta_B = 31.07^\circ$). The diffracted intensity is recorded by a scintillation detector. The Bragg angle is adjusted using goniometer 1, whereas the angular range ($\Delta\theta \pm \theta_B$) used to obtain rocking curves is provided using goniometer 2. The motorized translational stage is used to select different measuring regions on the crystal. [Figure H.4](#) shows SmS crystal with its corresponding coordinate system used to identify measuring regions. [Figure H.5](#) displays the rocking curves

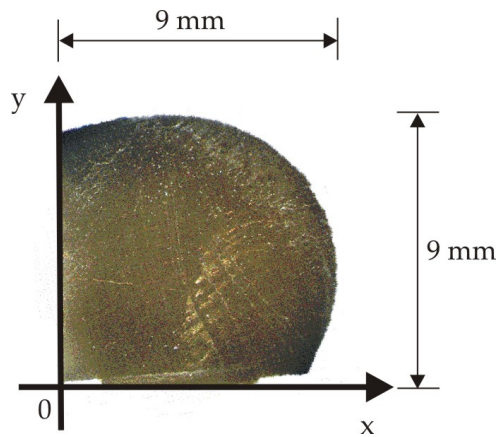


Figure H.4: The currently available SmS crystal with its corresponding coordinate system used to identify measuring regions.

measured at the regions located at $y = 5$ mm and $x = 0.9, 1.9, 2.4, 2.65, 2.9, 3.15, 3.4, 3.65,$ and 3.9 mm. Reflection curves up to $x = 2.65$ mm (grain I) show peaks, corresponding to $\text{Cu K } \alpha_1$ and α_2 , which do not change their position at different measuring regions; this results suggests that the rocking curves belongs to a single grain which is extended up to 2.65 mm (at $x = 2.9 - 3.15$ mm extra peaks begin to appear due to the exposure of the neighboring grains which surround the grain I). At $x = 3.4 - 3.7$ mm the $\text{K } \alpha_1$ peak

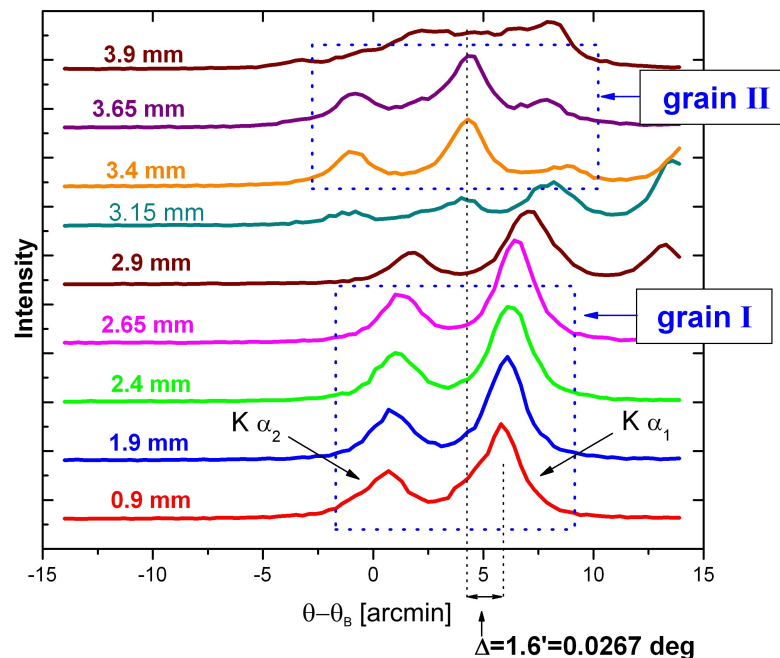


Figure H.5: Rocking curves measured at the regions located at $y = 5$ mm and $x = 0.9, 1.9, 2.4, 2.65, 2.9, 3.15, 3.4, 3.65,$ and 3.9 mm, $\text{Cu K } \alpha, 004$ reflection. The measuring curves reveal two grains: grain I and II, which are extended tilted about 1.6 arcmin relative to each other (see text).

is shifted about 1.6 arcmin; this indicates the presence of the second grain (grain II) which is tilted about 1.6 arcmin relative to the grain I (the extra peaks in the right side of $K \alpha_1$ correspond to a neighboring grain). By measuring the rocking curves every 0.25 mm throughout the crystal surface (up to $y=6$ mm), it is found that the currently available SmS crystal is composed of grains with dimensions up to 2.65 mm and tilted up to 1° relative to one another.

H.3.2 X-ray Diffraction Topography

X-ray diffraction topography is an imaging technique visualizing the variations of intensity diffracted by various points of the surface or the bulk of a crystal. These variations may be due to the fact that one region satisfies Bragg's condition for diffraction while another does not-this is called *orientation contrast*; they may also be due to the fact that the local crystal perfection and therefore the local reflectivity varies from point to point-this is called *extinction contrast*. The scheme of the experimental setup is shown in Figure H.6. X-ray topographs are obtained by using the same setup as for the measurement of rocking curves except that a photographic film (AGFA Structurix D7 FW) is used as a detector. The scheme of the experimental setup (top view of the setup shown in Figure H.3) is shown in Figure H.6. Translating the specimen and the film

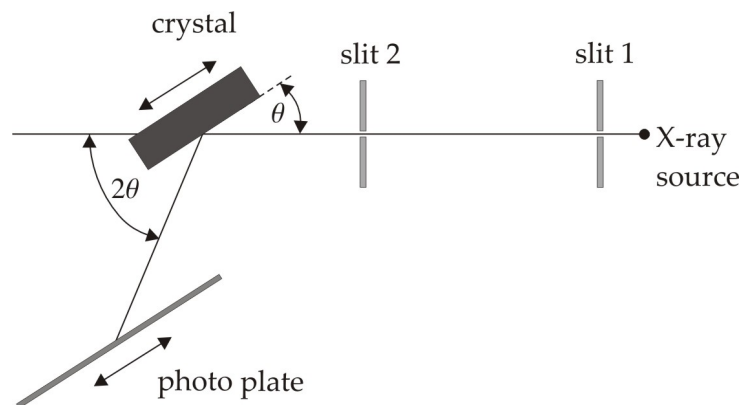


Figure H.6: The scheme of the experimental setup (top view of the setup shown in Figure H.3) used for X-ray diffraction topography. The incident beam ($\text{Cu K } \alpha_1$ and α_2) is collimated by a slit 2 with a size $0.2 \times 20 \text{ mm}^2$ (horizontal \times vertical). Translating the specimen and the film during the exposure simultaneously, a projection topograph which provides a two dimensional map of crystal irradiated area is obtained. The position of the film is chosen to be parallel to the specimen surface in order to obtain a geometrically undistorted image.

during the exposure simultaneously, a projection topograph which provides a two dimensional map of crystal irradiated area is obtained. The position of the film is chosen to be parallel to the specimen surface in order to obtain a geometrically undistorted

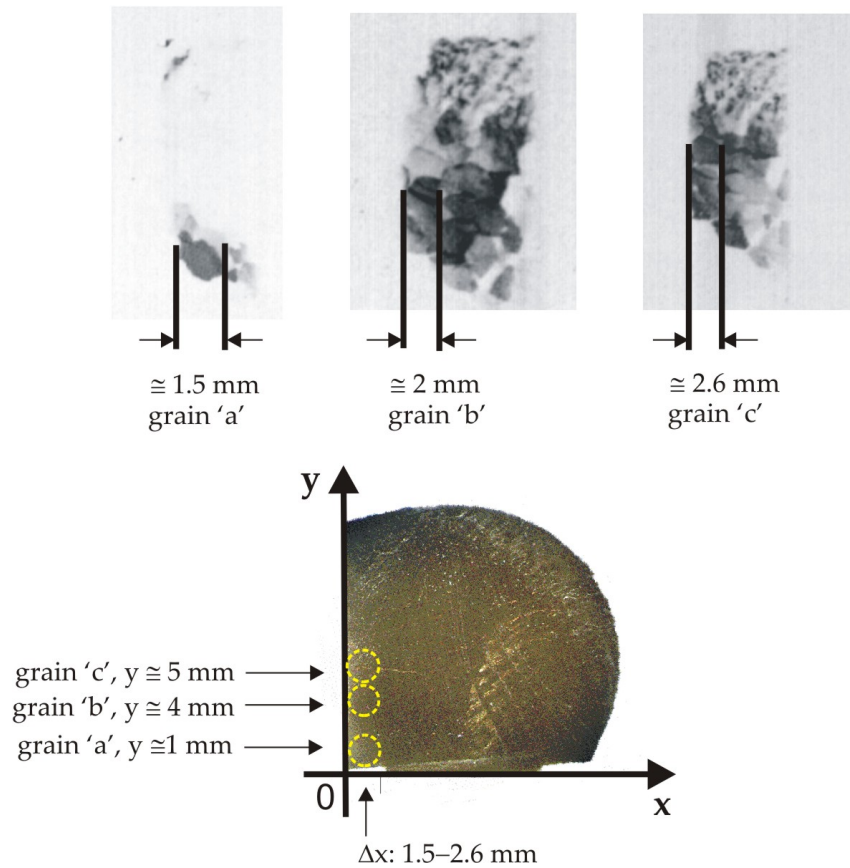


Figure H.7: Projection topographs which visualize three 'big' grains with their corresponding position on the crystal.

image. Combining the above mentioned methods, three 'big' grains with dimensions 1-2.7 mm, are visualized. They are shown, with their corresponding positions on the crystal surface, in Figure H.7.

H.4 Summary and Conclusions

The quality of the SmS crystal used in the ultrafast investigations presented in Chapter 7, is investigated using X-ray diffraction topography and by measuring the rocking curves at different positions on the crystal. It is found that the SmS crystal has mosaic structure i.e. it is composed from grains of dimensions up to 2.7 mm. The grains are disoriented up to 1° relative to one another.

Appendix I

Phonon Wave-Vectors in X-Ray Diffraction

X-ray diffraction experiments provide a means to study the longitudinal acoustic phonons. In the absence of the acoustic phonons, the Bragg condition is fulfilled when the difference of the wave vectors of the incident and diffracted X-rays, \mathbf{k} and \mathbf{k}' , respectively, is the sum of the reciprocal lattice vector \mathbf{G} . In the presence of the acoustic phonons, the plane spacing will change and this is accompanied by a corresponding change $\Delta\theta$ in the diffraction angle. In this case, when the diffraction signal is measurable, the Bragg condition is fulfilled when the difference of the \mathbf{k} -vectors equals the sum of the reciprocal lattice vector and the phonon wave vector \mathbf{q} . The phonon wave vector \mathbf{q} can be determined by wave vector matching considerations shown in Figure I.1. The geometry of the problem yields that

$$|\mathbf{q}| = 2x \cos \theta_B \quad (\text{I.1})$$

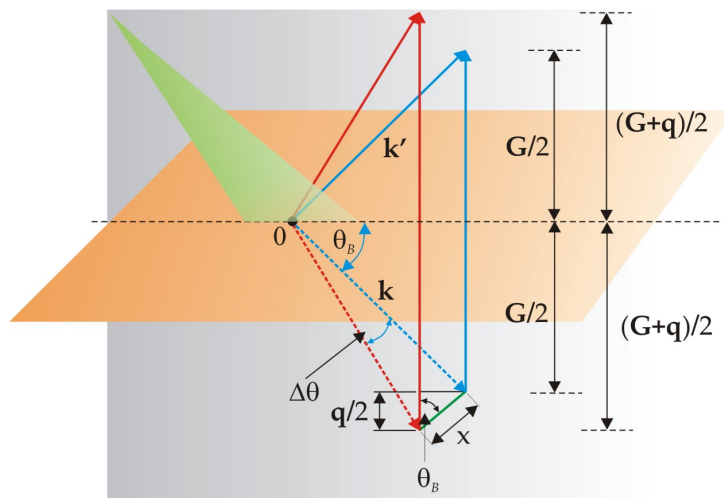


Figure I.1: Wave vector matching in the presence of longitudinal acoustic phonons.

and

$$x \approx |\mathbf{k}| \Delta\theta = \left(\frac{|\mathbf{G}|}{2 \sin \theta_B} \right) \Delta\theta \quad (\text{I.2})$$

Substitution of Eq.(I.1) into (I.1), yields the final form of phonon wave vector

$$|\mathbf{q}| = |\mathbf{G}| \Delta\theta \cot \theta_B \quad (\text{I.3})$$

Eq. (I.3) suggest that, as the glancing angle $\theta (= \theta_B + \Delta\theta)$ is varied, different phonon modes are selected out from the broad spectrum of the excited modes.

Danksagung

An dieser Stelle möchte ich mich bei allen bedanken, die zum Gelingen dieser Arbeit beigetragen haben. Besonderer Dank gilt

- Herrn Prof. Dr. Eckhart Förster für die herzliche Aufnahme in seiner Arbeitsgruppe, für die Möglichkeit, diese Arbeit durchzuführen, sowie für die hervorragende wissenschaftliche Betreuung;
- Herrn Dr. Oldrich Renner für die Betreuung und die vielen hilfreichen Hinweise beim ersten Teil der Arbeit;
- Herrn Dr. Ingo Uschmann und Herrn Dr. Andreas Morak für die Betreuung des zweiten Teils der Arbeit und die vielen hilfreichen Diskussionen und Hinweise;
- Frau Dr. Ortrud Wehrhan für die Hilfe bei Messungen in Röntgenlabors, für die 'Geburtstagskuchen' und für die Unterstützung in jeder Hinsicht;
- Herrn Prof. Dr. Roland Sauerbrey und Frau Prof. Dr. Elisabeth Leboucher-Dalimier für die Unterstützung und hilfreichen Ratschläge;
- Frau Jana Brusberg, Herrn Bernhard Retschke, Herrn Paul Puhlmann, Herrn Dr. Christian Reich, Herrn Dr. Sergei Podorov, Herrn Stephan König, Frau Adelheid Saupe und Frau Heike Marschner für die freundliche und kollegiale Atmosphäre;
- Herrn Dr. Laszlo Veisz für die vielen fruchtbaren Diskussionen, seine Hilfe mit dem MEDUSA Simulationscode und \LaTeX ;
- Frau Emmanuelle Defour und Herrn Romain Schott für die erfolgreiche Zusammenarbeit;
- Frau Andrea Lübcke, Herrn Flavio Zamponi und Herrn Tino Kämpfer für die Hilfe im Laserlabor;

- Meinen Eltern, meinem Bruder und meiner Schwester für ihre liebevolle Unterstützung in jeder Hinsicht.

Lebenslauf

Name: Faton Sadik Krasniqi
Geburtsdatum: 28. April 1978
Geburtsort: Skopje, Mazedonien
Staatsangehörigkeit: kosovoalbaner
Familienstand: ledig
Privatanschrift: Am Herrenberge 11, 07745 Jena

Sept. 1984 - Sept. 1992: Grundschule Gjon Sereqi in Ferizaj

Sept. 1992 - Sept. 1996: Mathematisch-naturwissenschaftliches
Gymnasium Kuvendi i Arbërit, Ferizaj

Okt. 1996 - Juli 2000: Studium der Physik an der Prishtina Universität
Okt. 2000: Abschluß mit Diplom. Thema: PWBA and DWBA Methods
in Stripping and Pickup Direct Nuclear Reactions

Seit Nov. 2001: Doktorand am Institut für Optik und Quantenelektronik
der Friedrich-Schiller Universität Jena, Deutschland

Jena, 03.07.2005

Ehrenwörtliche Erklärung

Ich erkläre hiermit ehrenwörtlich, daß ich die vorliegende Arbeit selbständig, ohne unzulässige Hilfe Dritter und ohne Benutzung anderer als der angegebenen Hilfsmittel und Literatur angefertigt habe. Die aus anderen Quellen direkt oder indirekt übernommenen Daten und Konzepte sind unter Angabe der Quelle gekennzeichnet.

Weitere Personen waren an der inhaltlich-materiellen Erstellung der vorliegenden Arbeit nicht beteiligt. Insbesondere habe ich hierfür nicht die entgeltliche Hilfe von Vermittlungs bzw. Beratungsdiensten (Promotionsberater oder andere Personen) in Anspruch genommen. Niemand hat von mir unmittelbar oder mittelbar geldwerte Leistungen für Arbeiten erhalten, die im Zusammenhang mit dem Inhalt der vorgelegten Dissertation stehen.

Die Arbeit wurde bisher weder im In- noch im Ausland in gleicher oder ähnlicher Form einer anderen Prüfungsbehörde vorgelegt.

Die geltende Promotionsordnung der Physikalisch-Astronomischen Fakultät ist mir bekannt.

Ich versichere ehrenwörtlich, daß ich nach bestem Wissen die reine Wahrheit gesagt und nichts verschwiegen habe.

Jena, 04.07.2005